Magnetoresistivity tensor of antimony and its alloy single crystals.

Rashid, A. A M.

Award date:
1978

Awarding institution:
University of Bath

MAGNETORESISTIVITY TENSOR

OF

ANTIMONY

AND ITS

ALLOY SINGLE CRYSTALS

by

A.A.M. RASHID

A thesis submitted to the
University of Bath
for the degree of
Doctor of Philosophy
1978

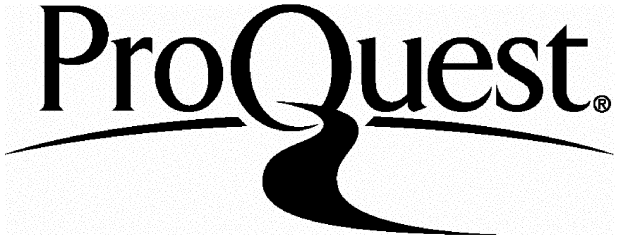

ABSTRACT

Magnetoresistivity tensor components have been measured as a function of orientation and magnetic field dependence in antimony and its p-type alloys with tin and germanium at 77°K, 196°K and 300°K. A special minimization program has been used to obtain the model parameters (the components of electron and hole mobility tensors, the carrier densities and the tilt angles of the Fermi surface ellipsoids) for a two band, multivalley ellipsoidal Fermi surface. The validity of the field dependent tensor method has first been checked on antimony itself; the model parameters of antimony found from components of field dependent tensors have been compared with those obtained using the low field method of Öktü and Saunders (1967). The results show that the field dependent tensor theory (Akgöz and Saunders 1975) can be extended to the treatment of galvanomagnetic effects of antimony and its alloys. The existence of Umkehr effect in the magnetoresistivity of antimony and its alloys has been established; this phenomenon can be understood on the basis of field dependent tensor description of transport properties. Then using the field dependent tensor method, extensive details of the temperature and concentration dependence of the carrier mobilities in antimony and its alloys have been obtained. It has been found that each tin or germanium atom removes one electron. The carrier mobilities in antimony alloys are dominated by ionized impurity scattering; the Born approximation is a better fit for these alloys than for bismuth-lead alloys (Bhargava 1967). The tilt angles of Fermi surface pockets are invariant with temperature and concentration.

ACKNOWLEDGEMENTS

Professor G. A. Saunders, my Supervisor, originally suggested the scheme of work, and has guided me throughout. I am most grateful to him, not only for his advice and encouragement, but also for keeping my mind alert by acting as a constant source of new ideas and fresh approaches.

I am indebted to all the technical staff, especially to Mr. B. Chapman for his assistance in the production of the manuscript, Mr. R. Draper for his help in crystal growth and to Mr. and Mrs. Lambson for their various technical assistance. I have benefited from many useful discussions with past and present members of Professor Saunders' Research Group.

Finally, I am grateful to the Iraqi Government for their financial support.

CONTENTS

CHAPTER ONE

GENERAL INTRODUCTION

Measurement of galvanomagnetic effects has long been a valuable method for obtaining information about the motion of charge carriers in crystals under the influence of electric and magnetic fields. The elemental group V semimetals antimony, arsenic and especially bismuth, have always been among the first materials in which new experimental studies of transport effects have been carried out.

At one time practice in galvanomagnetic studies of the semimetals, bismuth (Abeles and Meiboom 1956, Zitter 1962, Michenaud and Issi 1972), antimony (Öktü and Saunders 1967) and arsenic (Jeavons and Saunders 1969) was to measure the twelve coefficients that described the magnetoresistivity tensor components in the low field limit. Results were then interpreted in terms of the two carrier, multivalley band model to obtain a set of model parameters, the carrier densities, the component of electron and hole mobility tensors, the tilt angles of the Fermi surface allipsoids. Now that a general formalism for the magnetoconducitivity tensor is available (Akgöz and Saunders 1975), the model parameters can be obtained from the measurements of the magnetoresistivity tensor components $\rho_{ij}(B)$ at magnetic fields beyond the low field limit.

Saunders and Sümengen (1972) have pointed out important advantages of this field dependent tensor approach: the complete set of model parameters can be calculated from the measurements made on a single specimen, the considerable experimental difficulties encountered in measurement of low field magnetoresistivity tensor coefficients which are of necessity small are avoided. Akgöz and Saunders(1974) applied the new method in a study of the transport properties of arsenic-antimony alloy single crystals and showed that the band model parameters and mobilities calculated from the field dependent tensor components

and low field coefficient data were in excellent agreement. So by following their basic definition of the Hall-effect and magnetoresistance, the present work attempts to show that the field dependent tensor theory may be extended to the treatment of the transport properties of antimony and its alloy single crystals for the first time.

Since the overlap between the valence and conduction bands in antimony is small (~ 0.2 ev at low temperature), alloying with small quantities (~ 1 at %) of elements from neighbouring columns of the periodic table can give rise to a relatively large change in the carrier concentration. In the present work we have chosen to study crystals alloyed with tin and germanium where the Fermi level is lowered below the conduction band edge. Tin and germanium should behave as acceptors in antimony (increasing the number of holes and decreasing the number of electrons): this enables us to study the behaviour of the magnetoresistivity tensors in materials containing only holes and to compare the results with those in pure antimony itself. Measurements have been taken ($4.2^{o}K$ and $300^{o}K$) of electrical resistances (zero field) and magnetoresistivity tensor components of antimony and its alloy single crystals. These have been analysed using the field dependent tensor method, an approach which has never been used previously on these materials. The properties of antimony-germanium single crystal alloys have never been measured before by using any techniques. To test the applicability of the method, the model parameters of antimony and its alloys found from the component of the field dependent tensors have been compared with those obtained (Öktü and Saunders (1967) and Saunders and Öktü (1968)) using the low field method. In doped materials as opposed to pure elements changes in mobilities will result, not only from increased

impurity scattering, but also from a quantitative change in pure electron-phonon acoustic scattering. One aim of the present work has been to develop an understanding of the scattering processes in antimony and its alloys.

CHAPTER TWO

CRYSTAL STRUCTURE

2.1 Introduction

The group V elements bismuth, antimony and arsenic are semimetals. All have a rhombohedral crystal structure (space group $R\bar{3}m$) with two atoms per unit cell. The first five Brillouin zones contain just enough states to be filled completely by the ten valance electrons in the unit cell. However, the fifth zone just overlaps the sixth; a small number of electrons (in Sb about 10^{-3} per atom) spill over into the conduction band, leaving an equal number of holes in the valance band. (See figure 2.1) Their electrical properties reveal certain characteristic features typical of metals and others rather like those of semiconductors. For example, on the one hand the semimetals show a relatively high electrical conductivity with a positive temperature coefficient, in this their behaviour resembles the metals at all temperatures; on the other hand many carrier properties, such as density, energy gap, effective mass and mobility, and their sensitivity to impurity and defects, are similar to those observed in semiconductors; Cohen, Falicov and Golin (1964) have shown that most of the qualitative features of the energy bands and semimetallic character result directly from the rhombohedral A7-structure itself. Therefore, it is worthwhile examining this particular crystal structure in more detail.

Following the description of the crystal structure, the Brillouin zone of the group V semimetals will be described. To analyse the galvanomagnetic effects, a model of the Fermi surface must be assumed and this chapter ends with that.

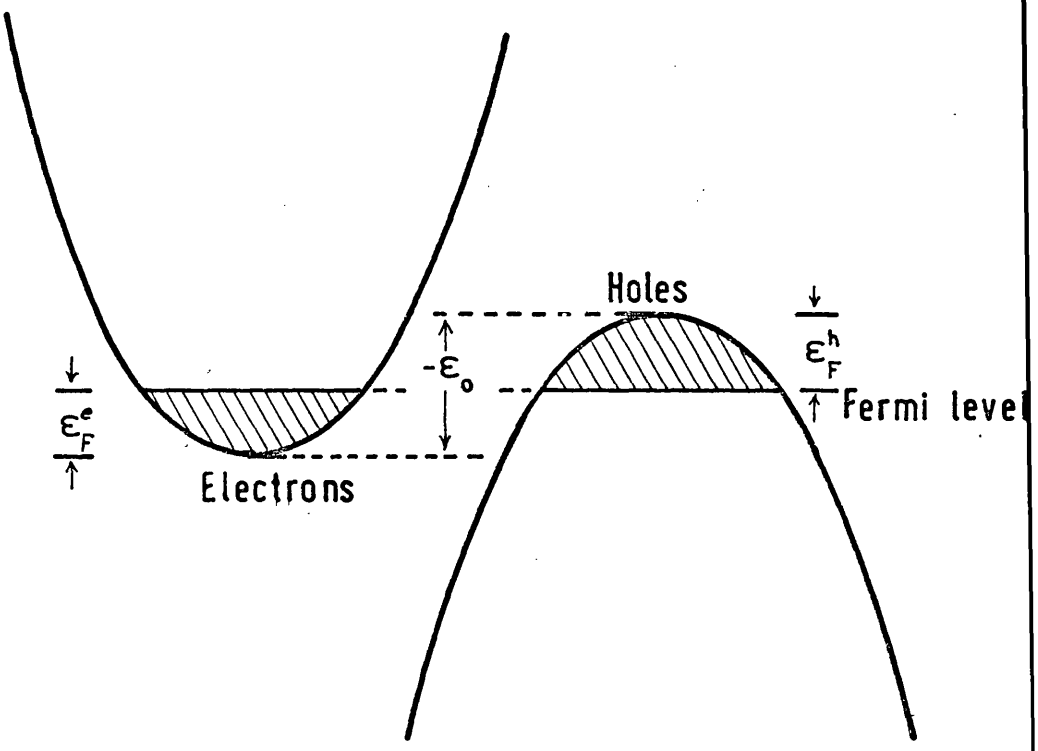

Fig.(2.1) Schematic diagram of the electron and hole bands in semimetals. In antimony $-\varepsilon_o$ is about 0.2 eV.

2.2 The crystal structure

The lattice can be obtained from a simple cubic lattice by separating it into two face-centred cubic lattices as shown in figure 2.2 (and figure 2.2a for rhombohedral structure).

The two sublattices are separated by a translation along the body diagonal so that the corner of one is at the centre of the other. Then by causing a slight trigonal distortion that slightly alters the value of rhombohedral angle (α) (which is 60^{o} prior to the distortion (see table 2.1)), the structure of the three elements bismuth, antimony and arsenic can be obtained.

The internal displacement of the atoms can be visualised easily by considering the simple cubic structure as being composed of two interpenetrating face centred cubic lattices. If it is assumed that the shear along the body diagonal has already been applied, the face centred cubic lattices in fact form two face centred rhombohedral lattices. Then the A7-structure is obtained by shifting one of these rhombohedral lattices towards the other along the sheared diagonal, which retains its symmetry and becomes the trigonal axis of A7-structure. The parameter u is defined by

$$\tau = ud \quad ; \quad u \leq 0.25$$

where 2τ is the smallest distance between the two atoms along this diagonal direction, and d is the length of rhombohedral body diagonal. The value $u = 0.25$ corresponds to the simple rhombohedral structure in a simple cubic lattice. The reason that many workers in the field have chosen to use the face centred cubic (fcc) cartesian axes is that there is a close relationship between the space lattices (see Falicov and Golin (1965)).

TABLE 2.1

Structure	α	u	ε
Simple cubic	60	0.250	0
Bismuth	57° 14	0.237	0.0420
Antimony	57° 14	0.234	0.0416
Arsenic	54° 10	0.226	0.0877

The resulting face centred rhombohedral lattice contains four primitive rhombohedral cells, each with two atoms. The primitive rhombohedral translation vectors can also be generated from the face centred cubic structure by including the effect of the distortion; they are:

$$\begin{aligned} \bar{a}_1 &= a_0\{\varepsilon,1,1\} \\ \bar{a}_2 &= a_0\{1,\varepsilon,1\} \\ \bar{a}_3 &= a_0\{1,1,\varepsilon\} \end{aligned} \qquad (2.2)$$

where { } indicated the reactangular coordinates and a_0 is half of the face-centred cubic lattice parameter; ε is related to the primitive rhombohedral angle α by

$$\cos\alpha = (1+2\varepsilon)/(2+\varepsilon^2) \qquad (2.3)$$

and $\varepsilon = 0$ corresponds to $\alpha = 60^\circ$ (which is the fcc lattice) so that ε is a measure of the distortion of the lattice from fcc. The parameter a_0 is related to ε and a by

$$a_0 = \frac{a}{\sqrt{2+\varepsilon^2}} \qquad (2.4)$$

The distortion of Bi and Sb from the cubic structure is small so that some directions, which would be symmetry axes in cubic structure, still produce back reflection Laue X-ray pictures which look as if the symmetry is preserved; such directions are usually referred to be the prefix "pseudo". An orthogonal set of crystallographic coordinates is usually defined as follows: the binary (x) axis is normal to any one of the three mirror planes, mutually oriented at 120°, which intersect in the three fold inversion (z) axis. The bisectrix (y) axis is in the mirror plane and completes the right handed orthogonal set. However, for the A7-structure this choice of coordinate system

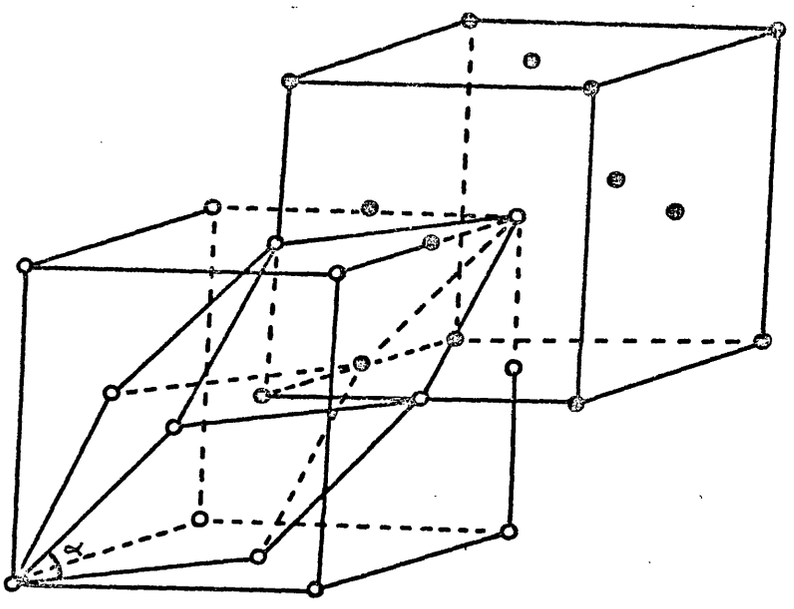

Figure (2.2) The relationship between the cubic lattice and the rhombohedral unit cell of the A7 structure.

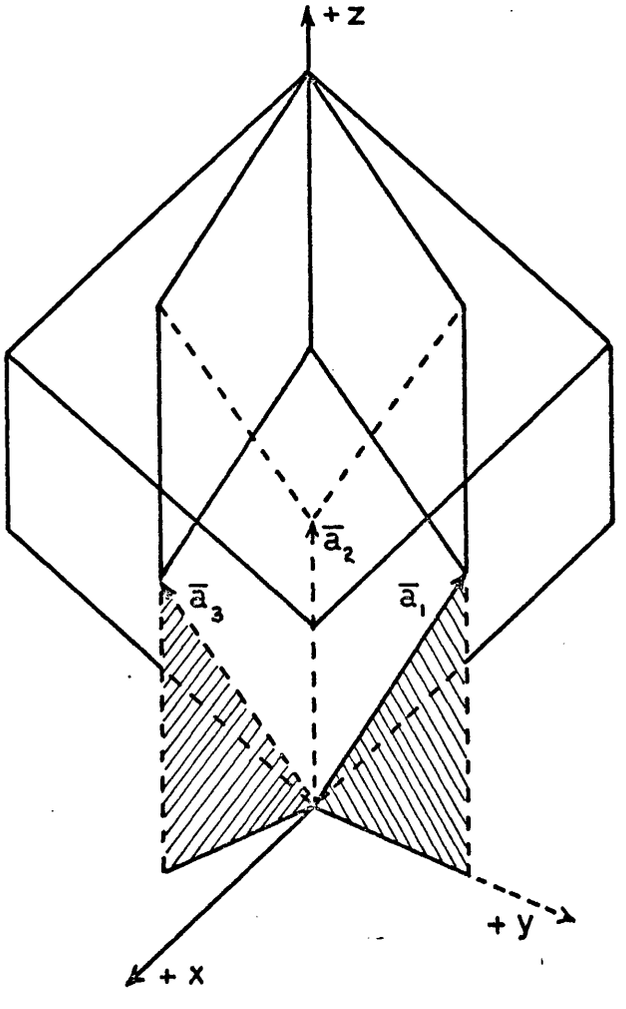

Figure (2.3) The primitive rhombohedral cell sited inside the large face-centred rhombohedron. The primitive translation vectors are denoted by $\bar{a}_i$ ($i = 1,2,3$), y axis is chosen by projecting one of the $\bar{a}_i$ on to (111) plane and the positive direction points outwards from the origin O of the $\bar{a}_i$.

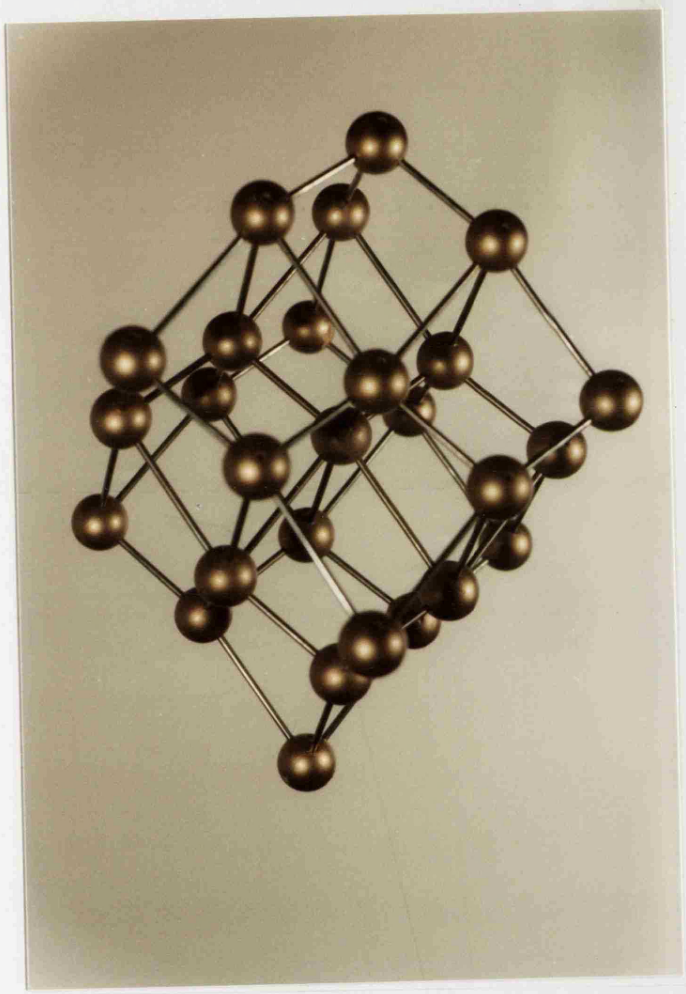

Fig.(2.2a) The rhombohedral($3\bar{m}$),A7-structure of antimony.

is not complete; it introduces ambiguities in the definition of the sign of some tensor components and hence the sense of the ellipsoidal angle of tilt (see Öktü and Saunders 1967, Akgöz and Saunders 1975). The usual convention (Jeavons and Saunders 1969) for definition of the right handed coordinates system is based on the geometry of the basis vectors of the primitive rhombohedral unit cell; the positive z-axis is taken along the body diagonal of the primitive rhombohedral unit cell defined by lattice translation vectors $\bar{a}_1$, $\bar{a}_2$ and $\bar{a}_3$ of equations 2.2, the y-axis is then defined by the projection of the $\bar{a}_i$-axis onto the trigonal plane. The positive y-direction is taken outward from the origin o (see Figure 2.3). A positive x-axis completes the right handed set. In the orientation of the crystals used here $+y$ and $-y$ directions could be identified in two ways; firstly, from the symmetry shown on the Laue-back reflection pictures (this experimental technique will be explained in detail in a later chapter); secondly from the orientation of the triangular etch pits on the xy plane (see Akgöz, Farley and Saunders 1972).

2.3 The Brillouin zone

Once the crystal structure is known, the Brillouin zone can be obtained by geometrical construction in K-space. The first Brillouin zone of the A7-structure with the symmetry points in standard notation is shown in Figure 2.4 (Akgöz 1975). This can be likened to the Brillouin zone of the face centred cubic structure but compressed along the trigonal direction ΓT. The square face in the Brillouin zone of the face centred cubic lattice now becomes reactangular and the hexagonal faces, not normal to the trigonal direction, now have unequal adjacent sides. The faces normal to the trigonal axis remain

regular hexagons. One of the mirror planes is exemplified by UTZLNXUΓ in the Brillouin zone; the binary ΓK, and the bisectrix ΓN, axes are also shown. ΓX and ΓL correspond to the pseudo-four fold and pseudo-three fold directions of the crystal structure respectively.

An important feature is that in the mirror plane rotation from the trigonal axis ΓT toward the bisectrix axis can be taken in one of the two senses, either through the point X or through the point L (Windmiller 1966). The ambiguity which arises from the fact that the binary axis cannot be uniquely defined, can be resolved through consideration of the sense of this rotation. Thus, one rotational cartesian co-ordinate system can be defined so that the rotation is that from the trigonal axis ΓT towards the bisectrix axis passing through ΓL; equally the system could be defined in the sense passing through ΓX.

2.4 The Band Structure

Detailed bandstructures have been calculated for bismuth (Golin 1968), antimony (Falicov and Lin 1966) and arsenic (Lin and Falicov 1966) by using the pseudopotential approach. These accord with experimental data : the essential features of the Fermi surface are now mapped out and turn out to be rather complicated, as might be expected from the distorted crystal structure. All these semimetals have similar electron surfaces, namely sets of six half-warped ellipsoids, which coalesce into three warped whole surfaces, centred about energy minima at the centre of the six irregular hexagon faces of the Brillouin zone (Figure 2.4); these minima lie in the three reflection planes. Each electron ellipsoid has one principal axis coincident with an axis of two fold symmetry - there are three of these, each obtainable

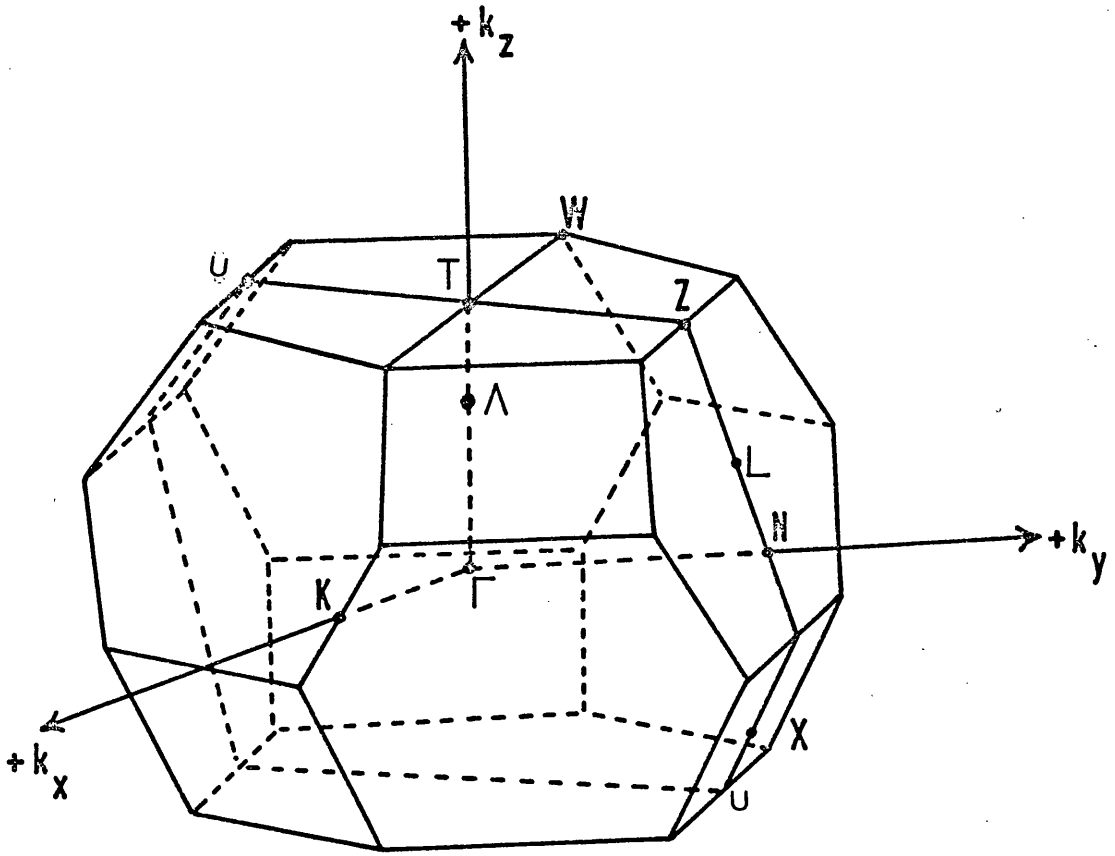

Figure (2·4) The Brillouin zone of Antimony.

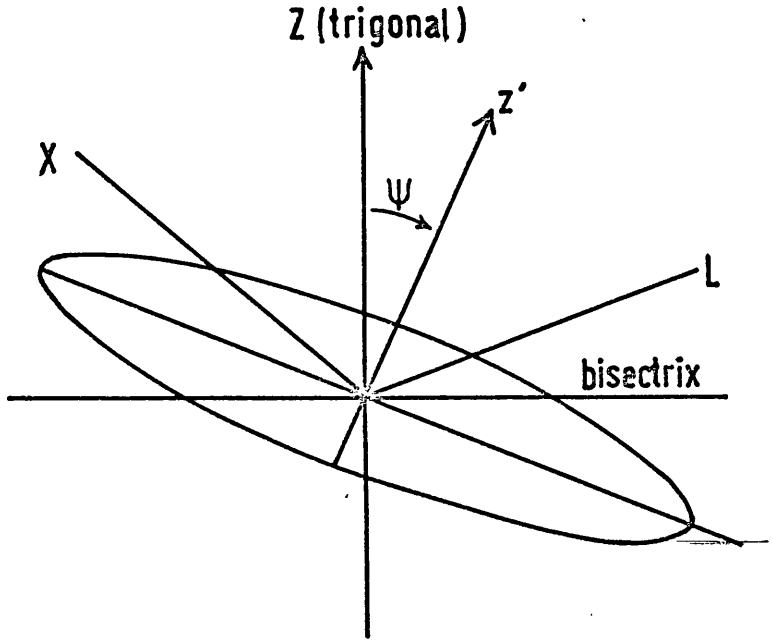

Figure(2·5) Cross section of an ellipsoid in the y-z plane.

from the others by a rotation of $\pm 120^{o}$ about the trigonal axis - while the other ellipsoid principal axis lies in the mirror plane. The configuration is illustrated in Figure 2.5. The tilt angles are collected in Table (6.6). The fact that in the A7-structure rotations by identical amounts in the mirror plane away from the trigonal axis towards the directions ΓX or ΓL are not equivalent is reflected in the tilt angles of the ellipsoids. To avoid the ambiguity, the sense of the tilt angle must be defined through specification of the direction employed for this rotation experimentally this is made easier from back reflection Laue photographs.

The hole surfaces differ considerably from one semimetal to another; in bismuth there is one ellipsoid of rotation about the trigonal axis (see Sümengen *et al* 1974), while in antimony and arsenic there are six highly tilted pockets. In arsenic these pockets are connected by the necks (Saunders 1968).

One intent of Fermi-surface studies is to sharpen our understanding of transport properties. Fundamental detail of the band and mobility parameters can now be obtained from measurements of the galvanomagnetic effects. Abeles and Meiboom (1956) first showed that the galvanomagnetic effect data in bismuth can be interpreted on the basis of a Fermi surface comprised of electron and hole ellipsoids. The method is incapable of providing an independent determination of the number of ellipsoids or their positions. However, a valuable feature is that galvanomagnetic effects do allow direct experimental discrimination between the carriers. Until recently, little experimental evidence was available to assign the electrons and holes to the two sets of pockets found for both antimony (Öktü and Saunders 1967) and arsenic (Jeavons and Saunders 1969).

Indeed for antimony the carriers in the highly tilted pockets were conventionally, although incorrectly, alluded to as electrons. This led to much confusion; measurements of the magnet-oresistivity tensor in antimony (Öktü and Saunders 1967), tin-doped antimony (Saunders and Öktü 1967), have shown that the holes are sited in each case in the most canted pockets. This is in agreement with the predictions obtained by Falicov and Lin (1966) and Lin and Falicov (1966), from the pseudopotential band structure calculation.

The experimental information can be summarised in the following way: (Öktü and Saunders 1967)

1. Both sets of pockets have at least binary or mirror symmetry
2. Both sets of pockets are tilted in the trigonal-bisectrix plane; i.e. that exemplified by UTZLNXU in the Figure(2.4).

The de-Haas van Alphen effect data of Windmiller (1966) shows that one set of pockets gives a maximum area for a magnetic field direction of about 6.5^{o} from trigonal axis in the quadrant containing ΓT, ΓL and ΓN (henceforth these will be described as the small tilt pockets). The other set gives a maximum area at a magnetic field direction of about 30^{o} in the same quadrant (called the large tilt pockets). The tilt angle sign must also be taken into consideration; this was detailed by Akgöz and Saunders (1974). So far all the reported theoretical and experimental work agrees that the cross-sections of the ellipsoids in the mirror plane are highly anistropic. All the tilt angles will be measured from the $+Ky$ direction. A positive tilt angle is then defined when $+y$ axis is rotated towards the ΓL direction, and if negative, when $+y$ axis is moved towards ΓX direction in the Brillouin zone. According to this definition, the electron and hole pocket tilt angles for antimony and arsenic are negative, while that for electron pockets in bismuth is positive. However,

for antimony the electron and hole pockets are not true ellipsoids (Falicov and Lin 1966): the direction of minimum areas are 87.7^{o} and 52.6^{o} respectively in the adjacent quadrant containing ΓT, ΓX and ΓL. The deviation of the pockets from ellipsoids is clear; for true ellipsoids the sum of the two angles of the minimum and maximum area directions measured in the two adjacent quadrant would be equal to 90^{o}, see Figure (2.5). The general situation of the number of pockets and their positions for antimony has been established and reviewed by Öktü and Saunders (1967).

The recent theoretical and experimental predictions can now be summarised. The electron and the hole pockets can both be approximated to ellipsoids, as can be seen from figures (2.6) and (2.7), and lie in the sets of three trigonal-bisectrix planes exemplified by ΓZLNUXΓ in the Brillouin zone. There are six hole pockets close to *T*, each having mirror symmetry and three electron pockets with *2/m* symmetry centred at *L*-point. This can only be true if the holes are assigned to the large tilt pockets and the electrons to the small tilt pockets, as established by Öktü and Saunders (1967), Windmiller and Priestley (1965). Because the number of electrons is equal to the number of holes, in this model the volume of a small tilt pocket must be twice that of a large tilt pocket (Öktü and Saunders 1967). A further result is that one principal axis of the ellipsoids is coincident with the binary axis of the crystal, while the other two lie in the mirror plane figure (2.5). A photograph of a model of the Fermi surface of antimony constructed in the Brillouin zone, is shown in Figure (2.8).

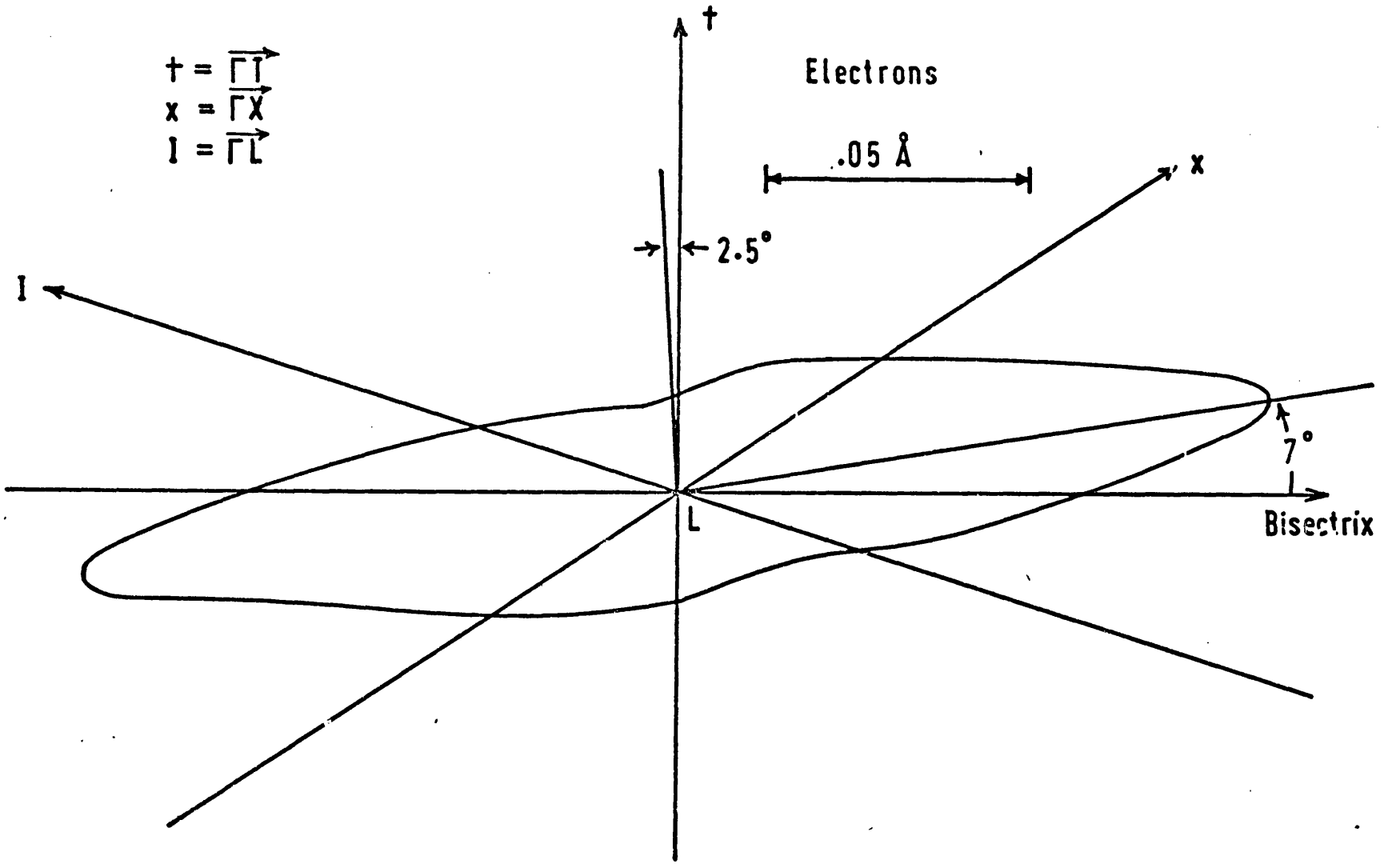

Fig.(2·6) Calculated cross-section of electron pockets in the mirror plane (Falicov and Lin 1966).

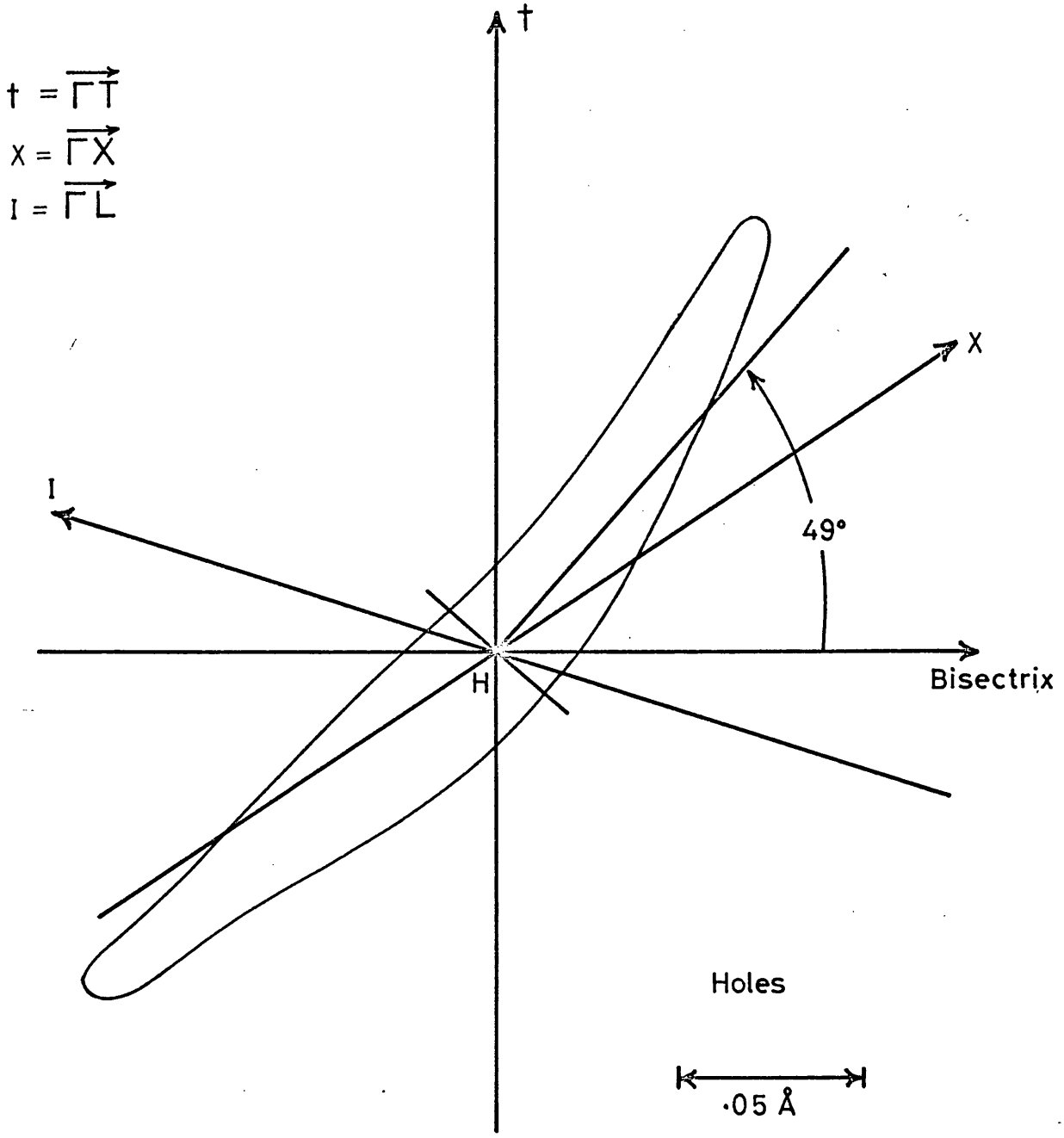

Fig. (2·7) Calculated cross section of hole pockets in the mirror plane (Falicov & Lin 1966).

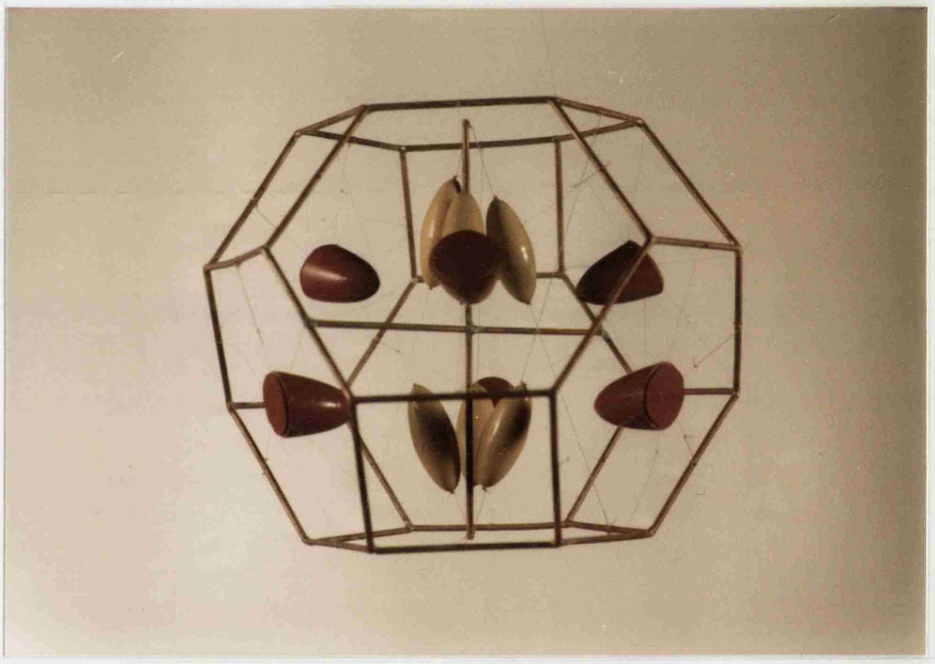

Fig.(2.8) A model of the Fermi surface of antimony.Red coloured surface contains electrons and the green,holes.

2.5 The effect of alloying antimony

The simultaneous presence of electrons and holes in antimony at all temperatures is due to overlapping of the valence and conduction bands (Dresselhaus 1971). The main effect of alloying with either group IV or group VI elements is to alter the Fermi level, which gives rise to interesting effects on the band structure, Fermi surface and carrier transport properties.

An important contribution to the understanding of the Fermi surface of semimetals has come from alloying experiments made with the intention of establishing the sign of the carriers in particular sets of pockets. Two approaches are available:

1. Either find the effects of donor (tellurium) or the acceptor (tin, germanium, lead) doping on the extrema cross-section areas of the Fermi surface using the de Haas van Alphen effects or quantum resonance phenomena.
2. or measure (an either pure or alloyed crystal) the galvanomagnetic effects. Which give the carrier signs and the density directly.

The results of such experiments can be compared with the detailed energy band calculations now available (Falicov and Lin 1966, Falicov and Golin 1965). Such a procedure has been particularly useful in the case of antimony, for which there has been some controversy about the assignment of carriers into the Fermi surface pockets (Datars and Dexter 1961; Smith, Galt and Merritt 1960). Alloying experiments have helped to answer the question: are the holes in the large or the small tilt pockets? The pseudopotential calculation (Falicov and Lin 1966) predict that the holes are in more tilted pockets.

Ishizawa and Tanuma (1965) found that when antimony is doped with tin, there is a decrease in the period of the de Haas-van Alphen oscillations corresponding to the large tilt pockets, while the periods due to extrema with small tilt angle increase. Tin doping should introduce extra holes. Now the period P of the de Haas-van Alphen oscillations is given by

$$P = \frac{2\pi e}{\hbar c A(E)} \quad ,$$

so the period of oscillations is inversely proportional to the cross sectional area $A(E)$ of the Fermi surface; the more tilted pockets expand with acceptor doping; under the same conditions the low tilt pockets decrease in volume: these must contain electrons. Tellurium, which would act as a donor (group VI) does not form solid solutions with antimony of sufficient concentration to make an appreciable difference to the carrier density (Prof. G.A. Saunders, private communication).

Hall and Seebeck coefficient measurements allow direct discrimination between the carriers. The controversy about which type of carriers occupy which set of pockets was started when Saunders *et al* (1965) pointed out that the Seebeck coefficient data on pure antimony can only be fitted if the carriers in the low tilt pockets are electrons. This suggestion has been confirmed by analysis of the low field magneto-resistivity tensor (Öktü and Saunders 1967) and of the Seebeck coefficient (Saunders and Öktü 1968) of antimony single crystals as well as by the work of Ishizawa and Tanuma (1965). Further confirmation of the carrier assignment has come from measurements of galvanomagnetic effects in antimony alloyed sufficiently heavily with tin (1.7 to 8 at %) to depress the Fermi level deeply into the valence band: the tilt angle of the pockets containing the

majority holes was found to be ($-19^{o} \pm 3^{o}$) in these alloys (Öktü and Saunders 1967, Saunders and Öktü 1968).

Further experimental evidence of the placement of the carriers into correct pockets arises from the present work: the galvanomagnetic effects in single crystals of pure antimony and of dilute antimony alloys with tin and germanium can only be explained by assigning the holes to the large tilt pockets. This will be discussed in due course.

A mirror plane cross section of the reciprocal lattice is used in figure (2.9) to illustrate for antimony the position of the electron and hole pockets in the Brillouin zone. This picture illustrates the results of the combined efforts of many experimentalists, including those who have made the studies of tin-antimony alloys outlined above, and finds a firm foundation in the calculated band structure (Falicov and Lin 1966). In order to depress the Fermi level below the conduction band edge, it is necessary to alloy antimony with a sufficient quantity of group IV elements; this then allows investigation of the valence band in a *p*-type material without the complicating effects produced by having electrons present as well; inspection of the data of Brown and Lane (1941) would indicate that 0.1 at % of tin should be sufficient to bring the alloy into the region of one carrier conduction; however, the results of Epstein and Juretschke (1963) imply that rather more than 1 at % tin is required to produce solely *p*-type alloys. More recently Dunsworth and Datars (1973) have studied the de Haas-van Alphen effect in antimony doped up to 0.29 at % *Sn*, their aim has been to explore the band structure near the Fermi level. In the 0.29 at % *Sn* alloy the electron frequencies are less than half those

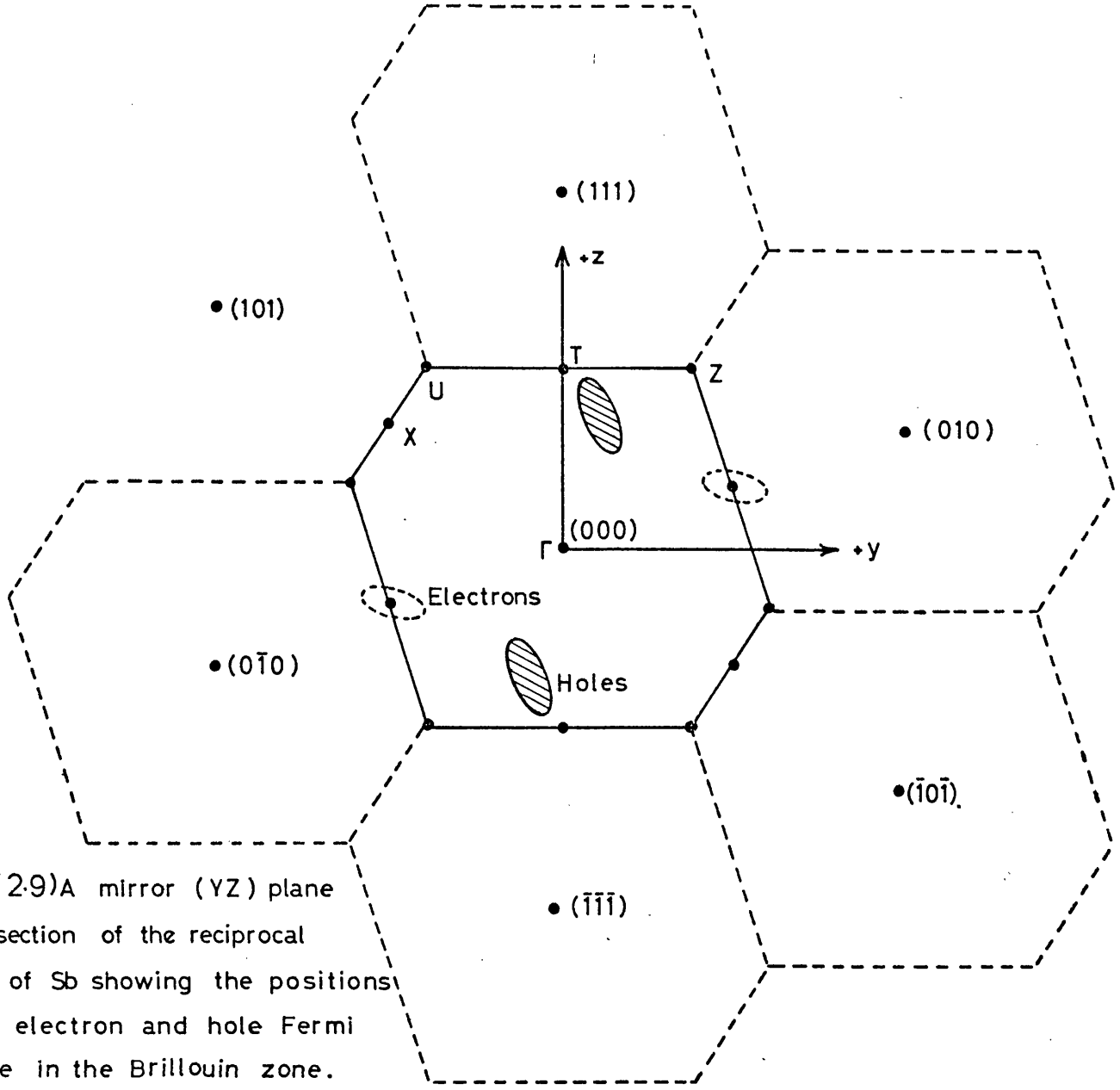

Figure (2·9) A mirror (YZ) plane cross-section of the reciprocal lattice of Sb showing the positions of the electron and hole Fermi surface in the Brillouin zone. (after Saunders 1974)

in pure antimony, while those corresponding to the hole surface are 75% larger. The tilt angles of the Fermi pockets do not alter significantly with acceptor concentration. They found a slight decrease in the axial ratio of the hole surfaces in the alloy as compared with that in pure antimony. That both conduction and valence bands are non-parabolic is evidenced by a decrease in electron cycltron mass, while the hole mass increases as the acceptor concentration is raised. Very recently (Harte and Priestley, private communication) have reported from de Haas-van Alphen studies of antimony crystals doped with up to 0.5 at % tin, that hole pocket dimensions expand with tin doping; under the same condition the electron pockets decrease in volume.

Now an important question still to be answered is: what is the valency of the dopants? Early workers noted that some elements seem to be more effective in altering the carrier density than others in the same column of the periodic table. For instance, when bismuth is doped with the group IV elements tin or lead, both introduce holes, but tin is three times more effective than lead (see Saunders 1974). It has proved difficult to assess the amount of tin necessary to produce purely *p*-type alloy of antimony; it is interesting to note that Dunsworth and Datars (1973) found from de Haas-van Alphen measurements that each tin atom removes one electron. This would be expected on the basis of the valency difference between these elements. Thus the electron pocket should become empty in an alloy containing 0.35 at % *Sn*. In contrast Harte and Priestley (private communication) estimate that the tin concentration needed to remove completely the electron pockets is $0.75 \pm 0.5\%$. Thus there is still a considerable discrepancy between the doping levels required to remove electrons completely

found by Dunsworth and Datars and Harte and Priestley. One aim of this present work has been devoted an attempt to resolve this and related problems. This study has been undertaken to determine how the transport properties and the Fermi surface of antimony, alloyed with tin (*Sn*) or germanium (*Ge*) differ from those of pure antimony and whether the differences observed are in agreement with the theories of alloys, particularly the rigid band theory. A determination of the required alloying percentage of tin or germanium to produce one carrier conduction has been made. Measurements have been taken (between 4.2K and 300K) of electrical resistivity (zero field) and magnetoresistivity components of antimony single crystals, alloyed with tin (0.5 at % to 1 at %) and germanium (1 at % to 2.2 at %). These were analysed using the field dependent tensor method (Akgöz and Saunders 1974) an approach which has never previously been used on these materials. In fact the properties of antimony-germanium alloys have never been measured before using any technique. In the next chapter the theory of the galvanomagnetic effects, the basis of the interpretation of the experimental data is to be discussed.

CHAPTER THREE

THEORETICAL BACKGROUND

3.1 Introduction

Conduction of electricity in a crystalline solid is described by the phenomenological linear transport equation:

$$\varepsilon_i = \rho_{ij}(B) J_i + \alpha_{ij}(B) \nabla_j T \qquad (3.1)$$

where ε is an electromotive force, **J** is the electrical current density and ∇T is the temperature gradient. $\rho_{ij}(B)$ and $\alpha_{ij}(B)$ are second rank polar magnetic field dependent tensors representing the magnetoresistivity and magnetothermoelectric power respectively. The principle of covariance requires both the function and their arguments to transform under any symmetry operation; thus it is required that all the components of a field dependent tensor transform among themselves under the action of all elements of the relevant point group. Akgöz and Saunders (1975) used the transformation law expressed as:

$$\rho_{ij}(|R|R_{1q}B_q, |R|R_{2q}B_q, |R|R_{3q}B_q) = R_{im}R_{jn}R_{mn}(B_1, B_2, B_3) \qquad (3.2)$$

to obtain the phenomenological forms of the magneto-resistivity tensor $\rho_{ij}(B)$ for crystal of all the 32 point groups. Treatment of $\rho_{ij}(B)$ as a field dependent tensor has an important impact on the study of the galvanomagnetic effect in crystals. Previous practice in such studies has been to expand $\rho_{ij}(B)$ as a power series in **B**.

$$\rho_{ij}(B) = \rho^0_{ij} + \rho^{(1)}_{ijK_1} B_{K_1} + \rho^{(2)}_{ijK_1K_2} B_{K_1K_2} + \ldots\ldots \qquad (3.3)$$

where the coefficient has the form:

$$\rho_{ijK_1K_2\ldots K_N} = \frac{1}{(N!)} \left(\frac{\partial^N \rho_{ij}(B)}{\partial B_{K_1} \ldots \partial B_{KN}} \right) \Bigg|_{B=0} \qquad (3.4)$$

Then these low field galvanomagnetic coefficients $\rho^{(1)}_{ijK_1}$ and $\rho^{(2)}_{ijK_1K_2}$ (which are constant tensors) were measured and the results interpreted in terms of band model parameters, using the equations first derived by Drabble and Wolfe (1956) and Abeles and Meiboom (1956), giving data for carrier densities, mobilities and tilt angles of the Fermi-surface ellipsoids (or some other Fermi-surface model). Recently, Bottzmann's transport theory has been used to explain the field dependent tensor components in terms of the band and mobility parameters for the group *V* semimetals (Fuchser *et al* 1970, Aubrey 1971, Sümengen and Saunders 1972); thus the theoretical formulation is now no longer restricted to the low field ($\mu B<<1$) condition and includes the so-called intermediate field region in which galvanomagnetic data previously could not be interpreted quantitatively. Analysis of field dependent tensor components now offers a powerful method of obtaining information about fundamental carrier transport processes in solids and renders the low field method obsolete. With this development a new dimension has been added to the area of galvanomagnetic studies (Akgöz and Saunders 1974). The field dependent tensor method is more practical, easier experimentally, and capable of predicting more accurate and comprehensive data of wider application than the low field method.

The purpose of the present work is to apply this new method further. The elemental group *V* semimetals arsenic, antimony and bismuth have usually been among the first materials on which experimental examinations of the theoretical predictions of transport theory have been carried out. As a test of the tensor field method, measurements of the field and orientation dependence of the components of $\rho_{ij}(B)$ have been made in the group *V* semimetals and other alloys (Saunders and Sümengen 1972, Akgöz and Saunders 1974, Sümengen *et al* (1974);

and the carrier densities, mobilities and tilt angles of the Fermi-surface ellipsoids determined. These band model parameters have been shown to be in reasonable agreement with those calculated from low field galvanomagnetic coefficient data. We extend here these measurements of the field and orientation dependence of the components of $\rho_{ij}(B)$ to antimony and its dilute alloys.

3.2 Transport tensors

The interpretation of galvanomagnetic effects rests upon assumptions concerning the nature of the Fermi surface. As described in chapter two the Fermi surface of antimony consists of two sets of closed, somewhat warped prolate ellipsoids, one of which corresponds to electrons, and the other to holes. The electron pockets of antimony are centred at the "*L*" points of the Brillouin zone and are tilted with respect to the trigonal plane. The hole pockets are located at the so called "*T*" points in the mirror planes and are also tilted with respect to the trigonal plane. For an ellipsoidal two band model the electron and hole mobility tensors in the right hand crystallographic $(+x,+y,+z)$ reference frame take the form

$$\mu = \begin{pmatrix} \mu_{11} & 0 & 0 \\ 0 & \mu_{22} & \mu_{23} \\ 0 & \mu_{32} & \mu_{33} \end{pmatrix}$$

and

$$\nu = \begin{pmatrix} \nu_{11} & 0 & 0 \\ 0 & \nu_{22} & \nu_{23} \\ 0 & \nu_{32} & \nu_{33} \end{pmatrix} \qquad (3.5)$$

respectively; thus μ_{11} and ν_{11} are parallel to the binary direction, the other two major axes of the ellipsoids associated with μ and ν lie in the mirror plane and are rotated about the axis by θ_μ and θ_ν respectively. A positive rotation corresponds to a positive tilt angle and is defined in the sense that the $+y$ axis would be rotated through the first quadrant towards $+z$ axis. The tilt angles are given by

$$\tan 2\theta_\mu = \frac{2\mu_{23}}{(\mu_{22}-\mu_{33})}$$

and

$$\tan 2\theta_\nu = \frac{2\nu_{23}}{(\nu_{22}-\nu_{33})} \qquad (3.6)$$

μ_{ij} and ν_{ij} are the electron and hole mobility tensor components expressed in the crystallographic axial system, for transformation equations for the mobilities from the ellipsoidal axis system to the crystallographic system see appendix I.

Thus the multivalley Fermi-surface model for antimony gives rise to a ten parameter model for the transport properties; these are effectively six mobility tensor components of μ and ν, carrier densities for electrons (N) and for holes (P) ($P=N$ for pure antimony) and tilt angles for electron and hole pockets.

To obtain solutions for these model parameters from measurements of the magneto-resistivity tensor components, the first step is to express the magnetoresistivity components in terms of magnetoconductivity components through

$$\rho_{ij}(\mathbf{B}) = (-1)^{i+j} \text{ cof.}\sigma_{ij}(\mathbf{B}) \,/\, \text{Det.}\sigma(\mathbf{B}) \qquad (3.7)$$

where cof. and Det. are the cofactor and determinant of $\sigma_{ij}(\mathbf{B})$ and $\sigma(\mathbf{B})$ respectively. The total magnetoconductivity tensor for a crystal

can now be written down by summing the three partial magnetoconductivities of a band and then summing over the two bands of the model, paying due attention to the sign. The resulting expressions are cumbersome for arbitrary directions of magnetic field, but take on the following simplified forms for **B** directed along the three crystal axes.

(i) $\mathbf{B} = (B,0,0)$

$$\sigma_{11} = (\mu_1'+d_e B^2)a_1 + \tfrac{1}{2}(\mu_1'+3\mu_2'+4d_e B^2)a_2 + (\nu_1'+d_h B^2)a_3 + \tfrac{1}{2}(\nu_1'+3\nu_2'+4d_h B^2)a_4$$

$$\sigma_{22} = \mu_2' a_1 + \tfrac{1}{2}(3\mu_1'+\mu_2')a_2 + \nu_2' a_3 + \tfrac{1}{2}(3\nu_1'+\nu_2')a_4$$

$$\sigma_{33} = \mu_3'(a_1+2a_2) + \nu_3'(a_3+2a_4)$$

$$\sigma_{23} = (\mu_4' - \frac{d_e}{\mu_1'}B)a_1 - \left[\mu_4' + \tfrac{1}{2}(3\mu_1'\mu_3' + \frac{d_e}{\mu_1'})B\right]a_2 + (\nu_4' + \frac{d_h}{\nu_1'}B)a_3 - \left[\nu_4' - \tfrac{1}{2}(3\nu_1'\nu_3' + \frac{d_h}{\nu_1'})B\right]a_4;$$

$$a_1 = ne\,(1+\frac{d_e}{\mu_1'}B^2)^{-1}\;; \quad a_2 = ne\left[1 + \tfrac{1}{4}(3\mu_1'\mu_3' + \frac{d_e}{\mu_1'})B^2\right]^{-1}$$

$$a_3 = ne\,(1+\frac{d_h}{\nu_1'}B^2)^{-1}\;; \quad a_4 = ne\left[1 + \tfrac{1}{4}(3\nu_1'\nu_3' + \frac{d_h}{\nu_1'})B^2\right]^{-1} \qquad (3.8.i)$$

(ii) $\mathbf{B}(0,\ B,\ 0)$

$$\sigma_{11} = \mu_1' b_1 + \tfrac{1}{2}(\mu_1'+3\mu_2') b_2 + \nu_1' b_3 + \tfrac{1}{2}(\nu_1'+3\nu_2') b_4$$

$$\sigma_{22} = (\mu_2'+d_e B^2) b_1 + \tfrac{1}{2}(3\mu_1'+\mu_2'+4d_e B^2) b_2$$

$$+ (\nu_2'+d_h B^2) b_3 + \tfrac{1}{2}(3\nu_1'+\nu_2'+4d_h B^2) b_4$$

$$\sigma_{33} = \mu_3'(b_1+2b_2) + \nu_3'(b_3+2b_4)$$

$$\sigma_{12} = \mu_1'\ \mu_4' B(b_1-b_2) - \nu_1'\ \nu_4' B(b_3-b_4)$$

$$\sigma_{23} = \mu_4'(b_1-b_2) + \nu_4'(b_3-b_4)$$

$$\sigma_{31} = -\ \mu_1'\ \mu_3' B b_1 - \tfrac{1}{2}(\mu_1'\mu_3' + \frac{3d_e}{\mu_1'}) B b_2 + \nu_1'\ \nu_3' B b_3 + \tfrac{1}{2}(\nu_1'\nu_3' + \frac{3d_h}{\nu_1'}) B b_4 \ ;$$

$$b_1 = ne\ (1+\mu_1'\mu_3' B^2)^{-1} \ ; \quad b_2 = ne \left[1 + \tfrac{1}{4}(\mu_1'\mu_3' + \frac{3d_e}{\mu_1'}) B^2\right]^{-1}$$

$$b_3 = ne\ (1+\nu_1'\nu_3' B^2)^{-1} \ ; \quad b_4 = ne \left[1 + \tfrac{1}{4}(\nu_1'\nu_3' + \frac{3d_h}{\nu_1'}) B^2\right]^{-1}$$

(3.8.ii.)

(iii) $\mathbf{B} = (0,\ 0,\ B)$

$$\sigma_{11} = \sigma_{22} = \frac{3}{2}\left[(\mu_1'+\mu_2') c_1 + (\nu_1'+\nu_2') c_2\right]$$

$$\sigma_{33} = 3\left[(\mu_3'+d_e B^2) c_1 + (\nu_3'+d_h B^2) c_2\right]$$

$$\sigma_{12} = 3\left[-\ \mu_1'\ \mu_2' B c_1 + \nu_1'\ \nu_2' B c_2\right] \ ;$$

$$c_1 = ne\ (1+\mu_1'\mu_2' B^2)^{-1} \ ; \quad c_2 = ne\ (1+\nu_1'\nu_2' B^2)^{-1}$$

(3.8.iii.)

All other elements can be obtained from the onsager relation or are zero. In these expressions, the symbols μ_i' and d_e refer to electrons, and ν_i' and d_h to the holes, the quantities μ_i', ν_i' and e all being positive.

3.3 Galvanomagnetic effects

In general, measurements of all the components of the magnetoresistivity tensor $\rho_{ij}(B)$ as a function of magnetic field strength and temperature provide sufficient experimental data to describe the galvanomagnetic effects of the particular crystal under consideration.

A field-dependent polar tensor of the second rank can be expressed as the sum of even and odd functions of the magnetic induction B:

$$\rho_{ij}(B) = \overset{\text{even}}{\rho_{ij}}(B) + \overset{\text{odd}}{\rho_{ij}}(B) \tag{3.9}$$

where

$$\overset{\text{even}}{\rho_{ij}}(B) = \overset{\text{even}}{\rho_{ji}}(B) \; ; \quad \overset{\text{odd}}{\rho_{ij}}(B) = - \overset{\text{odd}}{\rho_{ji}}(-B) \tag{3.10}$$

However, a common practice in the study of galvanomagnetic effects is to write the $\rho_{ij}(B)$ as the sum of the symmetric(s) and anti-symmetric(a) parts (with respect to the indices i and j).

$$\rho_{ij}(B) = \rho^s_{ij}(B) + \rho^a_{ij}(B) \tag{3.11}$$

where

$$\rho^s_{ij}(B) = \rho^s_{ji}(B) \; ; \quad \rho^a_{ij}(B) = - \rho^a_{ji}(B) \tag{3.12}$$

for a $\rho_{ij}(B)$, which obeying the Onsager relation

$$\rho_{ij}(B) = \rho_{ji}(-B) \tag{3.13}$$

we shall simply show that the symmetric part of $\rho_{ij}(B)$ is an "even" function of B, and the antisymmetric part is an "odd" function of B.

Let us first express $\overset{even}{\rho_{ij}}(B)$ and $\overset{odd}{\rho_{ij}}(B)$ in terms of $\rho_{ij}(\pm B)$.

$$\rho_{ij}(B) = \overset{even}{\rho_{ij}}(B) + \overset{odd}{\rho_{ij}}(B) \tag{3.14}$$

$$\rho_{ij}(-B) = \overset{even}{\rho_{ij}}(-B) + \overset{odd}{\rho_{ij}}(-B) \tag{3.15}$$

using equations (3.13) and (3.10) equation (3.15) becomes

$$\rho_{ij}(-B) = \overset{even}{\rho_{ij}}(B) - \overset{odd}{\rho_{ij}}(B) \tag{3.16}$$

Addition and subtraction, respectively of equation (3.16) from equation (3.14) leads to

$$\overset{even}{\rho_{ij}}(B) = \tfrac{1}{2}\left[\rho_{ij}(B) + \rho_{ij}(-B)\right] \tag{3.17}$$

$$\overset{odd}{\rho_{ij}}(B) = \tfrac{1}{2}\left[\rho_{ij}(B) - \rho_{ij}(-B)\right] \tag{3.18}$$

Application of the Onsager equation (3.13) and equation (3.12) to the right hand side of equation (3.18) yields

$$\rho_{ij}(-B) = \overset{(s)}{\rho_{ij}}(B) - \overset{(a)}{\rho_{ij}}(B) \tag{3.19}$$

Again addition and subtraction respectively of equation (3.19) from equation (3.11) yields

$$\overset{(s)}{\rho_{ij}}(B) = \tfrac{1}{2}\left[\rho_{ij}(B) + \rho_{ij}(-B)\right] \tag{3.20}$$

$$\overset{(a)}{\rho_{ij}}(B) = \tfrac{1}{2}\left[\rho_{ij}(B) - \rho_{ij}(-B)\right] \tag{3.21}$$

From equations (3.17) and (3.20) we get

$$\overset{even}{\rho_{ij}}(B) = \overset{(s)}{\rho_{ij}}(B) \tag{3.22}$$

and from equations (3.18) and (3.21) we get

$$\rho_{ij}^{odd}(B) = \rho_{ij}^{(a)}(B) \qquad (3.23)$$

Thus the symmetric part of $\rho_{ij}(B)$ is an even function of B, and the antisymmetric part is an odd function of B. However, this equivalence does not hold in general for other field-dependent tensors. It is better to employ the odd and even terminology in order to utilize the equivalent simplifications afforded in $\alpha_{ij}(B)$ (Akgöz and Saunders 1975). Furthermore, it is these even and odd terms which can be separated experimentally by reversal of the magnetic field direction and which have the more direct physical meaning.

Separation of $\rho_{ij}(B)$ into "even" and "odd" functions of B allows a major simplification of the description of the resistivity in a magnetic field. We can define the even part of $\rho_{ij}(B)$ as the magnetoresistance and odd part as the Hall-effect. This definition was probably first suggested by Casimir (1945), unfortunately throughout this vast subject there have been few followers of this definition, e.g. Logan and Marcus (1952) and Grabner (1960) in their Hall effect measurements of germanium crystal have adopted it and so has Jan (1957) in his review article. Later, Harman and Honig (1967) in their multiband formulations of the galvanomagnetic effects have found it convenient to split each transport tensor entry into "even" and "odd" contributions, and very recently Akgöz and Saunders (1974) used the field dependent tensor method in their treatment of the arsenic-antimony-alloy crystals.

On the other hand, several workers in the study of galvanomagnetic effects (see the example, Herring 1955; Landau and Lifshitz 1960 page 97; Shtrikman and Thomas 1965; Bhagavantam 1966 page 198,

Lifshitz *et al* 1973, page 168) have defined the magnetoresistance as the symmetric part of $\rho_{ij}(\mathbf{B})$ and the Hall-effect as the antisymmetric part of $\rho_{ij}(\mathbf{B})$; this we shall refer to as the second definition.

Beer (1963, page 71) and Hurd (1974) and some of the followers of the second definition have described the magnetoresistance and Hall effect by using both the first and second definitions. In fact because of the equalities (3.22) and (3.23), the two definitions turn out to be the same (see Akgöz and Saunders 1975). However, for the following two reasons we prefer to use the first definition:

1. The application of the symmetric and antisymmetric terminology to the other transport tensors for which equalities (3.22) and (3.23) do not hold, can make the description of these tensors complicated.
2. Experimentally components of $\rho_{ij}(\mathbf{B})$ this being the sum for even and odd functions of $\mathbf{B}$ can be measured by using the sample and merely reversing the sign of $\mathbf{B}$. On the other hand, measurements of the symmetric and antisymmetric part of the same components of $\rho_{ij}(\mathbf{B})$ (without making use of the property that the $\rho_{ij}(\mathbf{B})$ are even and odd functions of $\mathbf{B}$), may require two samples. As an example, consider the tensor component $\rho_{ij}(B_1)$ in point group $\bar{3}m$. To obtain the symmetric and antisymmetric part of $\rho_{ij}(B_1)$ the following equations may be used:

$$\overset{(s)}{\rho}_{23}(B_1) = \tfrac{1}{2}\left[\rho_{23}(B_1) + \rho_{32}(B_1)\right] \tag{3.24}$$

$$\overset{(a)}{\rho}_{23}(B_1) = \tfrac{1}{2}\left[\rho_{23}(B_1) - \rho_{32}(B_1)\right] \tag{3.25}$$

Thus, to measure $\rho_{23}(B_1)$ and $\rho_{32}(B_1)$, two differently oriented

(z-cut and y-cut) samples are required. But equations (3.17) and (3.18) show that "even" and "odd" parts of $\rho_{23}(B_1)$ can be obtained from one sample (z-cut). Kao and Katz (1958) have adopted another definition for the Hall-effect and magnetoresistance (third definition). If the measured field ($\vec{E}_{meas.}$) is normal to $\bar{J}$, they call the dependence $\vec{E}_{meas.}(\bar{J},\bar{B})$ a Hall effect; if $\vec{E}_{meas.}$ is parallel to $\bar{J}$, then $\bar{E}(J,\bar{B})$ is called the magnetoresistance. In this definition the off-diagonal even components $\rho_{ij}^{(even)}(B)$ $(i\neq j)$ are automatically included in the Hall effect. Since this definition considers $\rho_{ij}^{(even)}(B)$ $(i\neq J)$ to be part of the Hall effect, it can be the source of various Hall effects (see Akgöz 1974). We thus believe that this definition is not practical and makes the issue complicated and hence should be avoided.

3.3a Magnetoresistance

The magnetoresistance effect is the change in the electrical resistivity in the presence of a magnetic field induction B. We have already defined the magnetoresistance as a part of the magneto-resistivity tensor $\rho_{ij}(B)$ which is the "even" function i.e. $\rho_{ij}^{even}(B)$ this can be divided into two parts, diagonal components and off-diagonal components. The diagonal part can further be divided into two parts $\rho_{ij}^{even}(B_i)$ and $\rho_{ij}^{even}(B_K)$ $(i\neq K)$.

In the literature $\rho_{ij}^{even}(B_i)$ is often called the longitudinal magnetoresistance and $\rho_{ij}^{even}(B_K)$ $(i\neq K)$ the transverse magnetoresistance. The off-diagonal components of $\rho_{ij}^{even}(B)$, i.e. $\rho_{ij}(B_K)$ $(i\neq K)$, will be just called even off-diagonal components. Later, in a separate section we shall show that the co-existence of "even" off diagonal components with "odd" (Hall-effect) components is the main cause of the Umkehr effect in $\rho_{ij}(B)$.

It is obvious that the zero field resistivity tensor components are contained in $\rho_{ij}^{even}(B)$ and they can always be obtained by putting $B = 0$. In addition to the measurements of the components of $\rho_{ij}^{even}(B)$ as a function of B, measurements of the tensor components as a function of field direction (angular dependence) are a useful source of information about the shape of the constant energy surface of conductors.

Recently, polar data in bismuth and certain bismuth-antimony alloys obtained by Jacobson (1973), and on As(25.5%)-Sb alloy by Akgöz and Saunders (1974) and bismuth by Sümengen *et al* (1974) have been used to compute the band model parameters of these materials.

3.3b Hall effect

We have already defined the Hall efect as a part of $\rho_{ij}(B)$ which is an "odd" function of B that is $\rho_{ij}^{odd}(B)$, in any configuration of the sample the Hall field vanishes when $B = 0$.

Hall-effect measurements are usually made by employing samples in rectangular parallelopiped geometry. Constant current is maintained through the long direction of the sample. In general when an external magnetic field is applied to the sample, a potential difference perpendicular to the current direction develops. Part of this voltage which changes sign on reversal of the sign of B, is called the Hall-field. Notice that in this configuration current direction is always normal to the Hall-field. But we have no condition for B; it can be applied in any direction. The off-diagonal even components (which we include under the magneto-resistance) have frequently been considered as a part of the Hall-effect and several different names have been called for them (see Akgöz 1974).

The group *V* semimetals *Bi*,*Sb* and *As* crystallize in the rhombohedral A_7-structure point group $\bar{3}m$. The form of $\rho_{ij}(\mathbf{B})$ for this point group is (Akgöz and Saunders 1975)

$$\rho_{ij}(B_1) = \begin{pmatrix} \rho_{11}(B_1) & 0 & 0 \\ 0 & \rho_{22}(B_1) & \rho_{23}(B_1) \\ 0 & 0 & \rho_{33}(B_1) \end{pmatrix} + \begin{pmatrix} 0 & 0 & 0 \\ 0 & 0 & \rho_{23}(B_1) \\ 0 & 0 & 0 \end{pmatrix}$$

$$\rho_{ij}(B_2) = \begin{pmatrix} \rho_{11}(B_2) & 0 & 0 \\ 0 & \rho_{22}(B_2) & \rho_{23}(B_2) \\ 0 & 0 & \rho_{33}(B_2) \end{pmatrix} + \begin{pmatrix} 0 & \rho_{12}(B_2) & \rho_{13}(B_2) \\ 0 & 0 & 0 \\ 0 & 0 & 0 \end{pmatrix}$$

$$\rho_{ij}(B_3) = \begin{pmatrix} \rho_{11}(B_3) & 0 & 0 \\ 0 & \rho_{11}(B_3) & 0 \\ 0 & 0 & \rho_{33}(B_3) \end{pmatrix} + \begin{pmatrix} 0 & \rho_{12}(B_3) & 0 \\ 0 & 0 & 0 \\ 0 & 0 & 0 \end{pmatrix} \qquad (3.2\ 6.)$$

where **B** is directed in turn along each of the crystallographic axes (x,y,z) (we write suffixes 1,2,3 for x,y,z respectively). The procedure adopted to obtain a component $\rho_{ij}(B_1,B_2,B_3)$ is to cut rectangular parallelopiped samples; pass a current along the long direction (j) and measure the voltage developed in the ith direction as a function of the applied magnetic field. When the orientation dependence is required, the magnetic field direction is taken stepwise around the chosen plane.

3.4 The Umkehr effect in $\rho_{ij}(B)$

For space time symmetry as shown by Akgöz and Saunders (1975), the Umkehr effect can occur in certain off-diagonal components of the magnetoresistivity tensor. Over the years the occurrence of the Umkehr effect in $\rho_{ij}(B)$ has been the subject of some debate (see, Casmir and Gerritsen 1941; Jan 1957 for review, and Akgöz and Saunders 1975). In the previous section we showed that certain magnetoresistivity tensor components contain both odd and even terms. When measurements of such components are made, the potential difference developed with, depend upon the sense of the magnetic field direction. To show that the Umkehr effect can occur in $\rho_{ij}(B)$, let us consider the case of $\rho_{23}(B_1)$ for A_7-structure ($\bar{3}m$ point group) semimetals. In measurement of such components the even and odd part can readily be separated by reversing the direction of magnetic field (from $(+x)$ $(+B_1)$ to $(-x)$ $(-B_1)$) with the current along the $+z$ direction. The potential difference (v) developed in the y-direction is then

$$v_2(+B_1) = v^{\text{even}}(B_1) + v^{\text{odd}}(B_1) \tag{3.27}$$

$$v_2(-B_1) = v^{\text{even}}(B_1) - v^{\text{odd}}(B_1) \tag{3.28}$$

Akgöz and Saunders (1975) in their phenomenological approach showed that $v_2(B_1)$ and $v_2(-B_1)$ should not be equal because $\rho_{23}(B_1)$ is not identical to $\rho_{23}(-B_1)$ and thus that an Umkehr effect can exist in the magnetoresistivity. The question now is whether or not the difference is measurable? We can answer this by inserting known band model parameters into the expression for $\rho_{23}(\pm B_1)$ and thus calculating the expected magnitude of the Umkehr effect in bismuth and antimony in the following way:

$$\rho_{23}(\pm B_1) = \frac{-\sigma_{23}(\pm B_1)}{\sigma_{22}(B_1)\,\sigma_{33}(B_1) - \sigma_{23}(-B_1)\,\sigma_{23}(B_1)} \qquad (3.29)$$

where

$$\sigma_{22}(B_1) = \mu_{22}a_1 + \tfrac{1}{2}(3\mu_{11}+\mu_{22})a_2 + 3\nu_{11}a_3$$

$$\sigma_{33}(B_1) = \mu_{33}(a_1+2a_2) + 3\nu_{33}a_3$$

$$\sigma_{23}(\pm B_1) = (\mu_{23} \pm \frac{de}{\mu_{11}} B_1)a_1 - (\mu_{23} \pm (3\mu_{11}\mu_{33} + \frac{de}{\mu_{11}})B_1)a_2 \pm 3\nu_{11}\nu_{33}B_1 a_3$$

and

$$a_1 = ne\left(1+ \frac{de}{\mu_{11}} B_1^2\right)^{-1}$$

$$a_2 = ne\left(1+\tfrac{1}{4}(3\mu_{11}\mu_{33}+ \frac{de}{\mu_{11}})B_1^2\right)^{-1}$$

$$a_3 = ne\left(1+\nu_{11}\nu_{33}B_1^2\right)^{-1}$$

$$de = \mu_{11}(\mu_{22}\mu_{33}-\mu_{23}^2)$$

By inserting known band parameters into the expression for $\rho_{23}(\pm B_1)$ following the method of Aubrey (1971), Akgöz and Saunders (1975), we have calculated the expected magnitude of the Umkehr effect in bismuth at 77K for B_1 = 0.5 Tesla.

$$\rho_{23}(+B_1) = 18.8 \times 10^{-7}\Omega m, \quad \rho_{23}(-B_1) = -4.9 \times 10^{-7}\Omega m$$

Thus,

$$\rho_{23}^{\text{even}}(B_1) = 6.9 \times 10^{-7}\Omega m$$

and

$$\rho_{23}^{\text{odd}}(B_1) = 11.9 \times 10^{-7}\Omega m$$

Umkehr effect for antimony crystal at 77K for B_1 = 0.5 Tesla (Fig.(3.1).

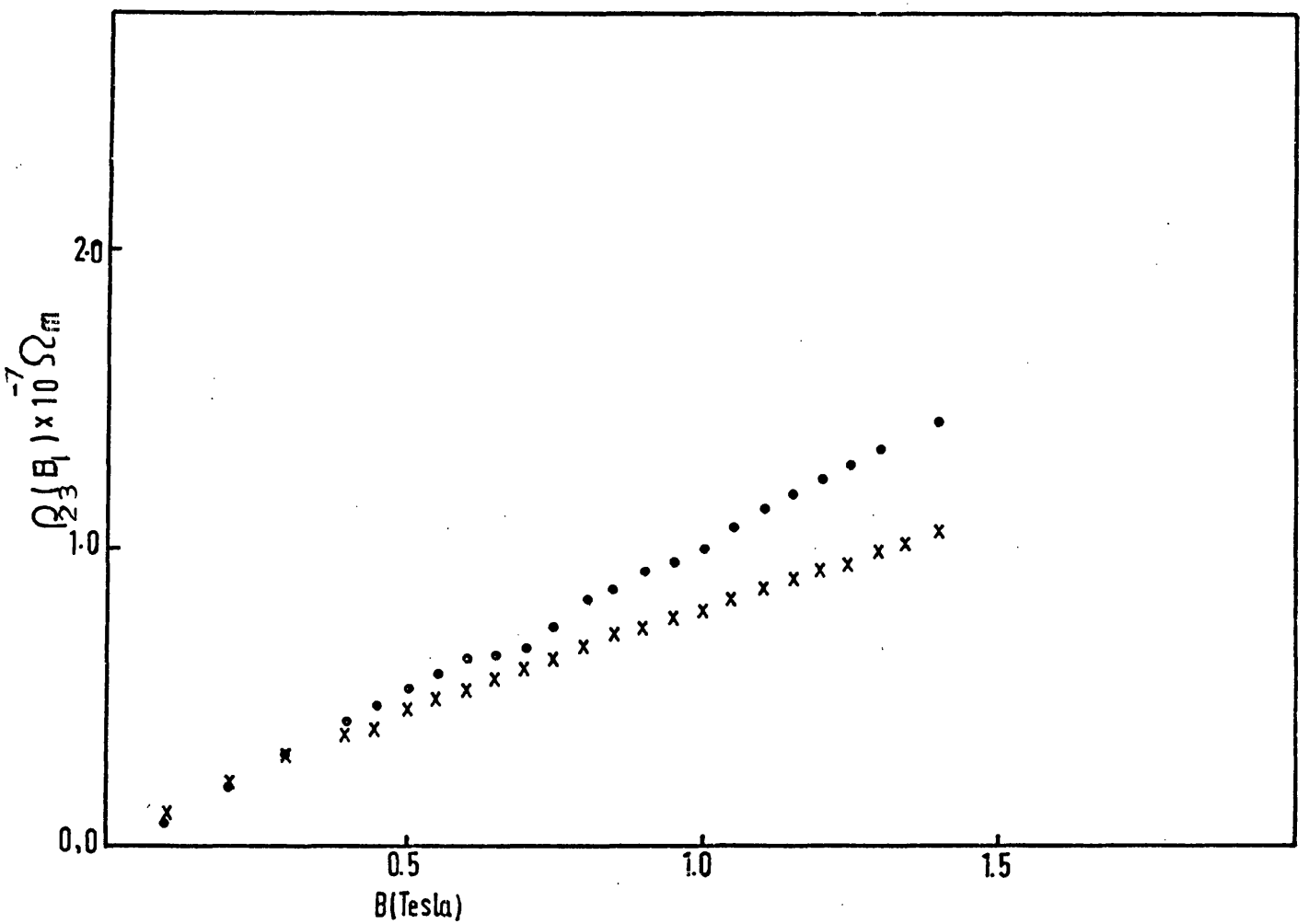

Fig(3.1) The variation of $\rho_{23}(B_1)$ with the magnetic field at 77°K.

(x) $-B_1$ direction
(·) $+B_1$ direction

$$\rho_{23}(+B_1) = 5.41 \times 10^{-8}\Omega m, \quad \rho_{23}(-B_1) = -3.95 \times 10^{-8}\Omega m$$

Thus

$$\rho_{23}^{\text{even}}(B_1) = 0.73 \times 10^{-8}\Omega m$$

and

$$\rho_{23}^{\text{odd}}(B_1) = 4.68 \times 10^{-8}\Omega m$$

The Umkehr effect in $\rho_{23}(B_1)$ is substantial. The existence of even terms of $\rho_{23}(B_1)$ depends on the presence of tilt angle Fermi surface ellipsoidal. If there were no tilt angle there would be no Umkehr effect in $\rho_{23}(B_1)$, because when the tilt angles are put to zero in the equation for $\rho_{23}(\mathbf{B})$ then

$$\rho_{23}(B_1) \text{ equal } \rho_{23}(-B_1).$$

CHAPTER FOUR

GROWTH OF ANTIMONY ALLOY SINGLE CRYSTALS BY ZONE LEVELLING AND EXPERIMENTAL DETAILS.

4.1 Elementary Principle to Zone Levelling

In choosing a crystal growth method, certain parameters have to be taken into account. Generally melt growth is capable of producing large single crystals and is usually chosen when possible in preference to the vapour and solution growth methods. Critical parameters in melt growth are melting point, congruency of melting point, vapour pressure and compatability with crucible materials. An additional important requirement for this work was to achieve a uniform distribution of dopant; for these reasons the zone levelling method was chosen.

Below, a brief description is given of the zone levelling technique together with an outline of the problems that can arise in preparing antimony alloy crystals. The furnace and growth technique actually used are then described, followed by an assessment of the success of the method and the quality of the finished product.

The purpose of zone levelling is to produce a uniform distribution of solute in an ingot. In this case, the solute is tin and the solvent is antimony. Before giving a description of the zone levelling technique, we need to discuss an important parameter, namely the distribution coefficient.

Figure 4.1 shows the phase diagram for the special case in which the constitutional forms a solid solution over the whole concentration range. Now the equilibrium distribution coefficient K_o is defined by

$$K_o = \frac{\text{concentration of solute in solid solution}}{\text{concentration of solute in the liquid}} \qquad (4.1)$$

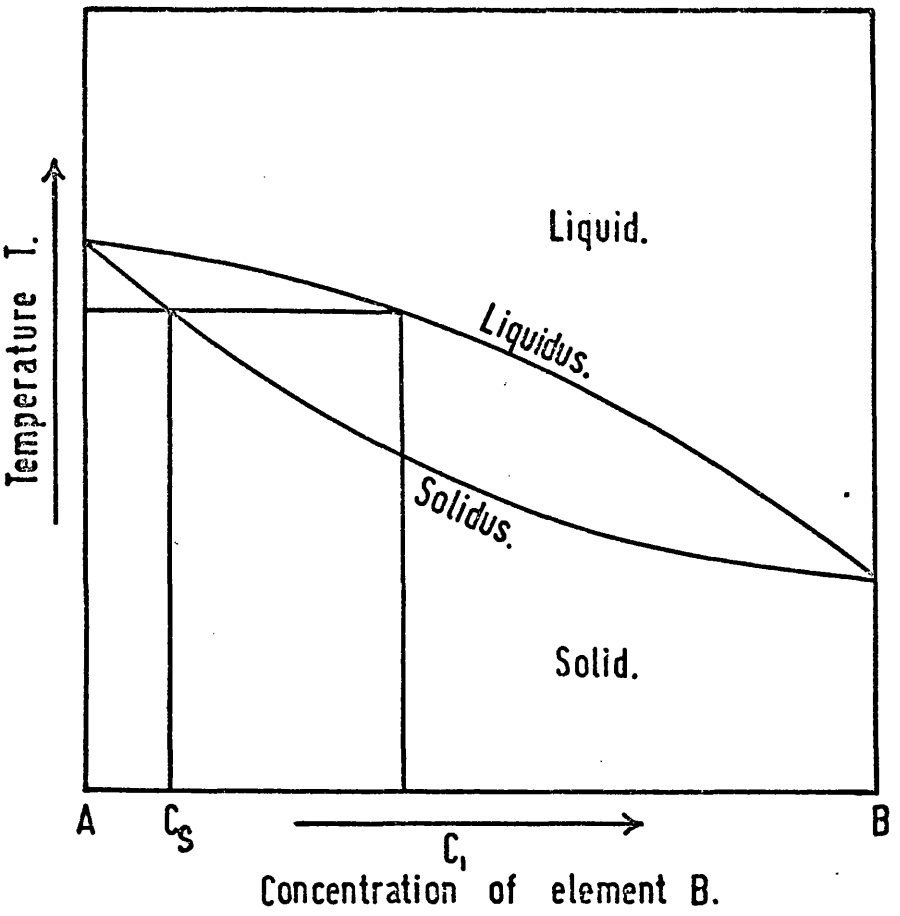

Figure (4.1) Phase diagram of a simple binary alloy

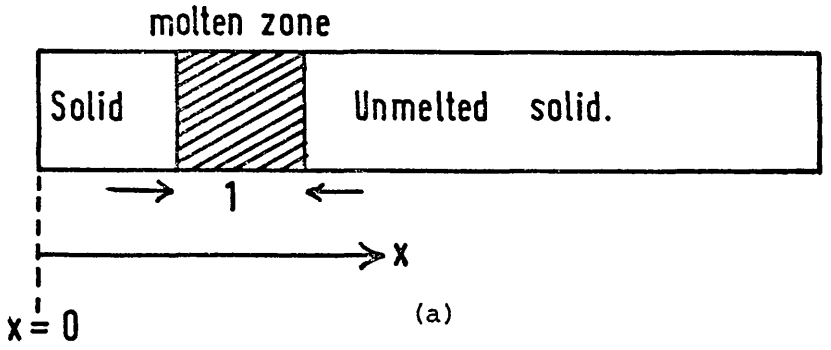

(a)

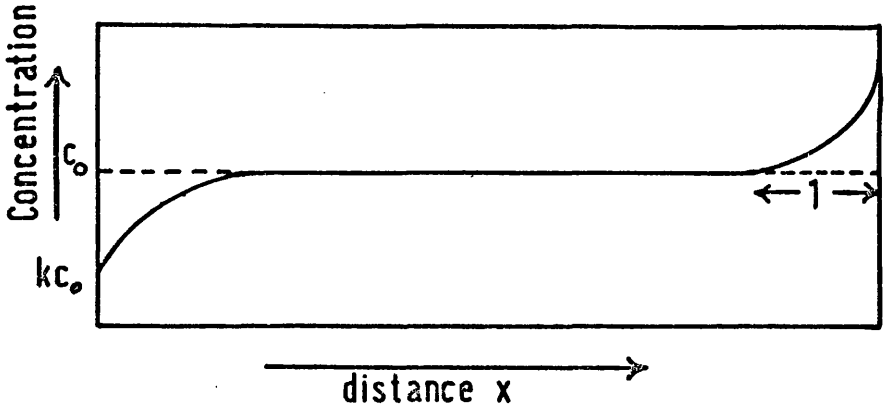

(b)

Figure (4.2) Principles of zone-levelling (after Pfann, 1966)

and therefore can be obtained from the phase diagram directly. In practice K_o is not quite the same as the effective distribution coefficient K which is defined as

$$K = \frac{\text{solute concentration in freezing solid}}{\text{solute concentration in main body of liquid}} \qquad (4.2)$$

Now consider Figure (4.2a) and take K to be less than one. (This occurs when the solubility of the solute in the solid is less than in the liquid); this corresponds to "rejection" of solute atoms by the solid as it forms, and therefore to a progressively increasing concentration of solute in the remaining liquid (Tiller *et al* 1953); that is, the tin lowers the melting point of antimony and so K is less than unity for the alloy system under consideration. Let us consider that change of concentration C_o and that a portion of it (length ℓ) is melted and moved along the bar. At the start the molten zone has the concentration C_o, but as it advances it freezes out a solid of concentration KC_o ($KC_o < C_o$); and it also, at its leading edge, takes in a solid of concentration C_o. This means that the zone gets richer in concentration of solute as it proceeds along the bar, and freezes out a solid which in its turn becomes richer in solute. This state of affairs continues until the concentration of the molten zone reaches C_o/k, at which point it is taking in the solid of concentration C_o at its leading edge, and freezing out the solid of concentration C_o at its trailing edge. This region of uniform deposition of C_o lasts until the zone reaches the end of the bar when the zone itself freezes into a region of higher solute concentration. The final distribution of the concentration of solute in the bar which results from the zone passage is shown in the Figure (4.2b).

In the present work, the required concentrations of solid and liquid zone were found from the phase diagrams. Thus, returning to Figure (4.1), if an alloy of final concentration C_s is desired, the zone to be melted is made up with concentration C_ℓ. Here we are using the equilibrium distribution coefficient K_o in setting up the starting changes, but this is not very different from K. (in the present work at 1.0at% tin crystal the value of K is about 0.25)

4.2 Growth procedure

In growing an alloy of desired concentration X, the first step was to determine, from the phase diagram, the necessary concentration to be used in making the liquid zone; when this had been done, the amounts of antimony and tin needed to produce charges of the desired size and concentration were calculated from the following formula:

$$W_1 = \frac{VA_1\rho_1\rho_2}{\rho_2 A_1 + (\frac{1-x_1}{x_1})\rho_1 A_2} \tag{4.3}$$

$$W_2 = \frac{VA_2\rho_1\rho_2}{\rho_1 A_2 + \rho_2 A_1 (\frac{x_1}{1-x_1})} \tag{4.4}$$

W_1 = weight of element one needed to give an alloy containing an atomic fraction x_1 of one

W_2 = weight of element two needed for the same alloy

V = volume of charge

A_1, A_2 = atomic weight of element one and two

ρ_1, ρ_2 = densities of elements one and two.

4.3 The Furnace

The furnace comprised a toroidally wound Kanthal "A" resistance wire heater powered by a stepless Eurotherm SR-10 temperature controller, the sensor for which was a Pt-PtRh 13% thermocouple embedded deep in the heater assembly to increase the temperature gradient. The technique provided a temperature gradient of $40^{\circ}C/Cm$ at the solidus-liquidus interface (measured with a thermocouple embedded in the surface of the alloys). Water cooled copper coils were mounted on either side of the furnace. The entire assembly was able to traverse the bed by virtue of a screw thread driven by a variable speed motor (traversing speeds of 0.2 mm - 2.5 mm/hr. were available).

Before the growth process, the high purity elements (99.9999% pure antimony) were fused together in a vacuum (10^{-3}torr) and raised to $650^{\circ}C$ to drive off volatile oxides; continuous shaking of the alloys promoted mixing. The frozen polycrystalline boule was then transferred to the quartz boat and melted within the zone leveller (for more details see Lichnowski 1975 and Figure 4.5).

The difficulty of maintaining a constant width of molten zone, especially during growth of these alloys, did not lead us to expect uniformity of concentration over the whole length of the ingot, and this was found to be the case. The concentration gradient over the middle section of the bar used in cutting samples was of the order of 0.03 at % per cm. in 0.5 at % Sn (Hart 1974). Samples taken from the start of the ingot were invariably more concentrated than those taken from the end.

4.4 Orientation of the Crystals

The boules were etched to show up any grain boundaries and thus to ensure that samples were cut from single crystal regions. Several potential etching reagents were examined; the etch composed of three parts hydrofluoric acid (40%), five parts concentrated nitric acid, three parts glacial acetic acid and a few drops of bromine; the crystals were immersed in this mixture for one or two seconds, followed by washing in distilled water.

4.4a Laue - back reflection photographs

Crystallographic orientation of the as-grown crystal was accomplished by means of Laue-back reflection X-ray photography, the cartesian coordinate system assigned to the rhombohedral lattice is described in Chapter two. The trigonal axis (z) was easily identified by the typical three-fold symmetry (cleaved plane) (see Figure 4.7), the binary (x) axis by the two-fold symmetry (see Figure 4.6), and the bisectrix (y) axis was recognised from its relationship with the trigonel (z) axis (see Figure 4.8)

To orient A7-structure crystals in general and the Sb-Sn alloys in particular, the sense of the y direction has to be determined, subsequent to and consistent with an arbitrary choice of a positive direction along the trigonal (z) axis. To achieve this end, we have used the following technique (for more detailed account see Akgöz and Saunders 1971).

The process involved in aligning a crystal of an A7-structure material depends on the fact that this structure is closely related to the simple cubic structure from which it can be obtained, by applying two independent small distortions (Falicov and Golin 1965, Windmiller 1966) (see Chapter two for details of the rhombohedral

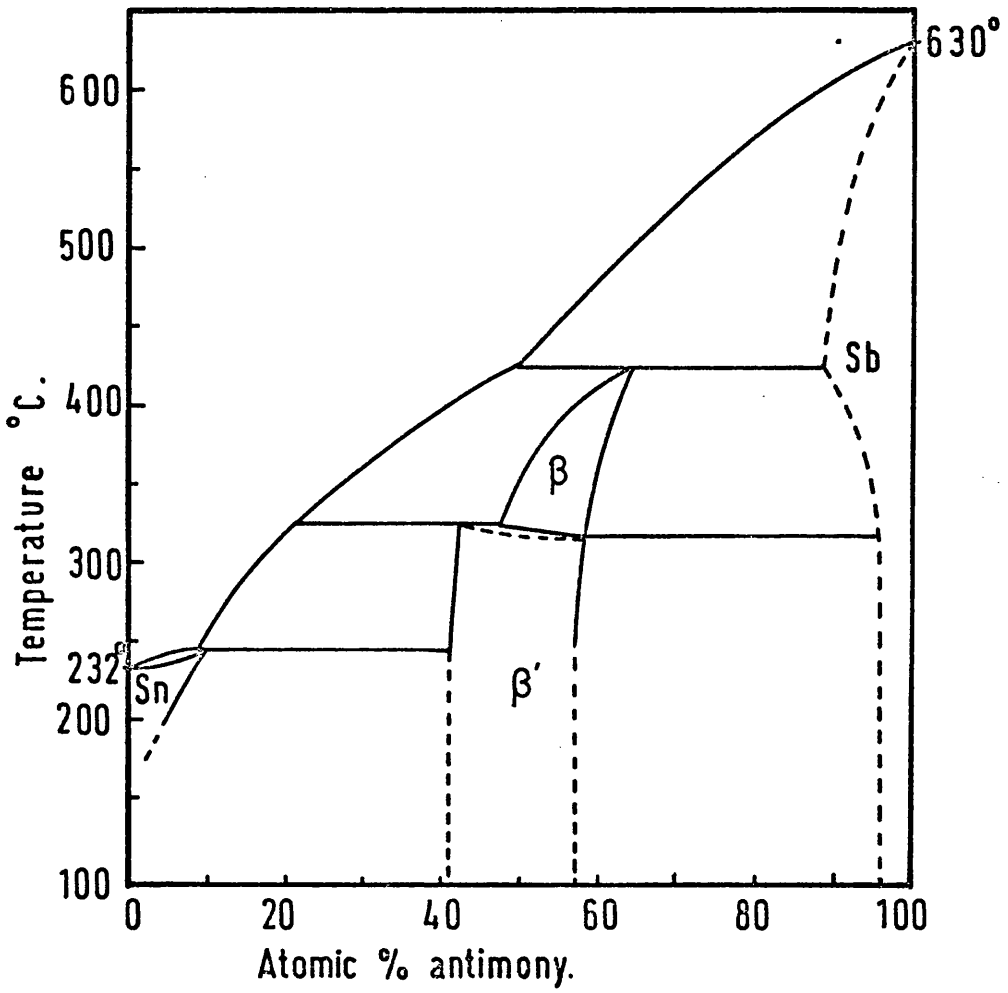

Figure (4.3) Phase diagram of antimony-tin alloys

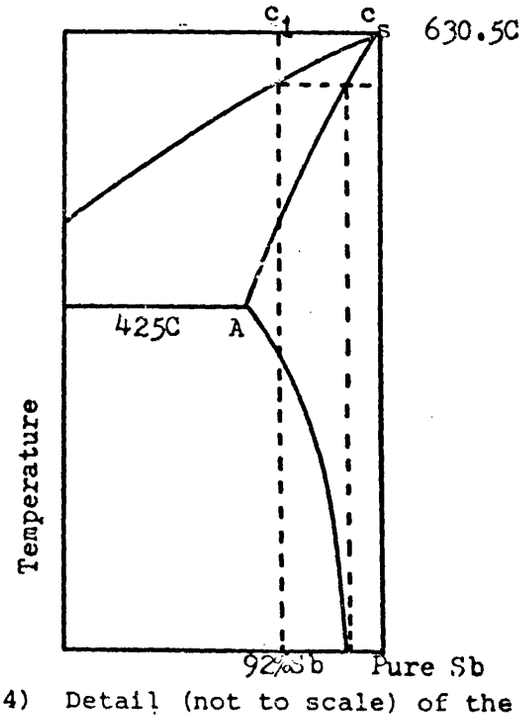

Figure (4.4) Detail (not to scale) of the antimony-tin pnase diagram

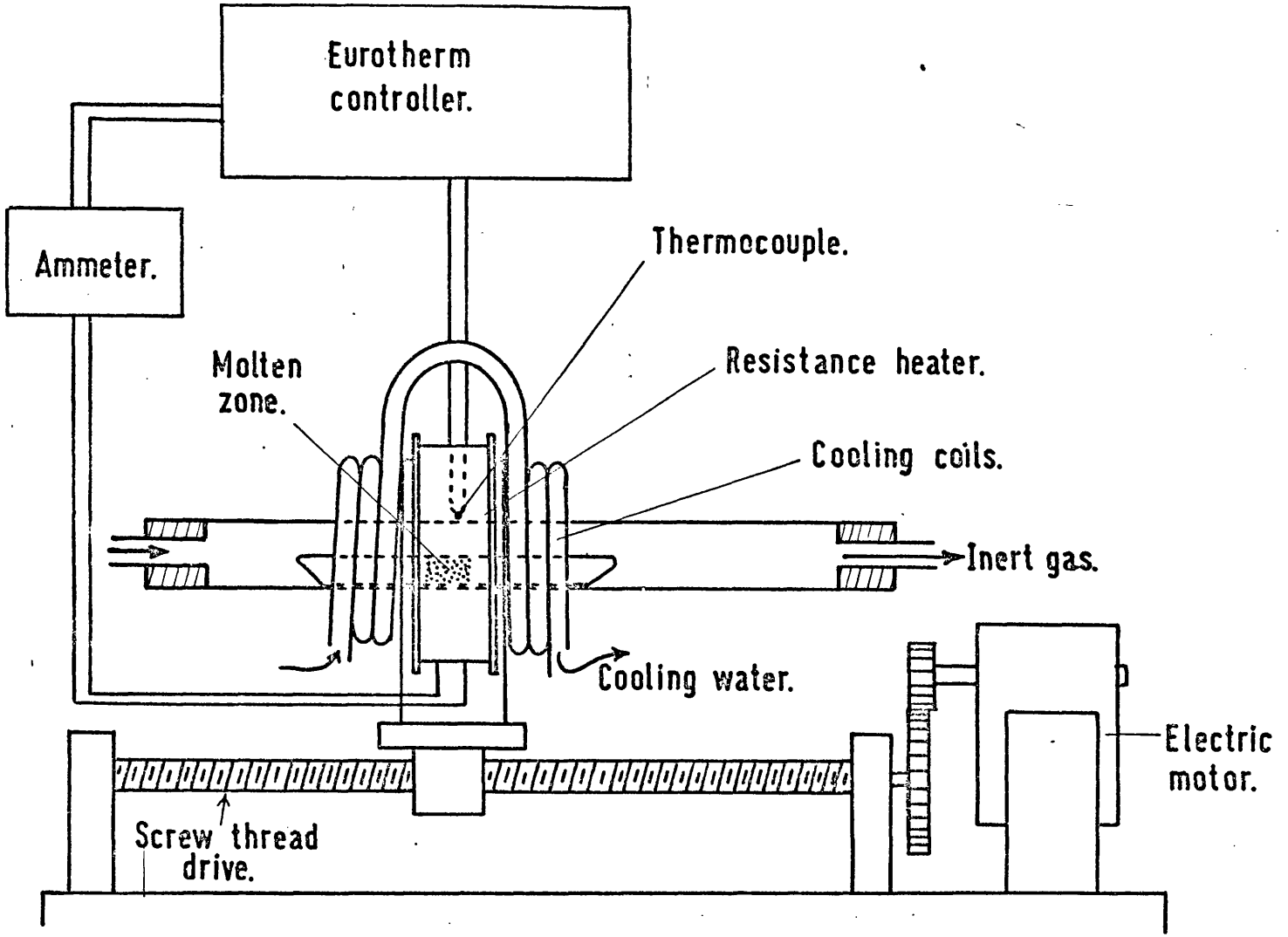

Figure (4.5) The Zone Leveller

Figure (4.6) Laue-reflection X-ray photograph of antimony along the binary (x) axis.

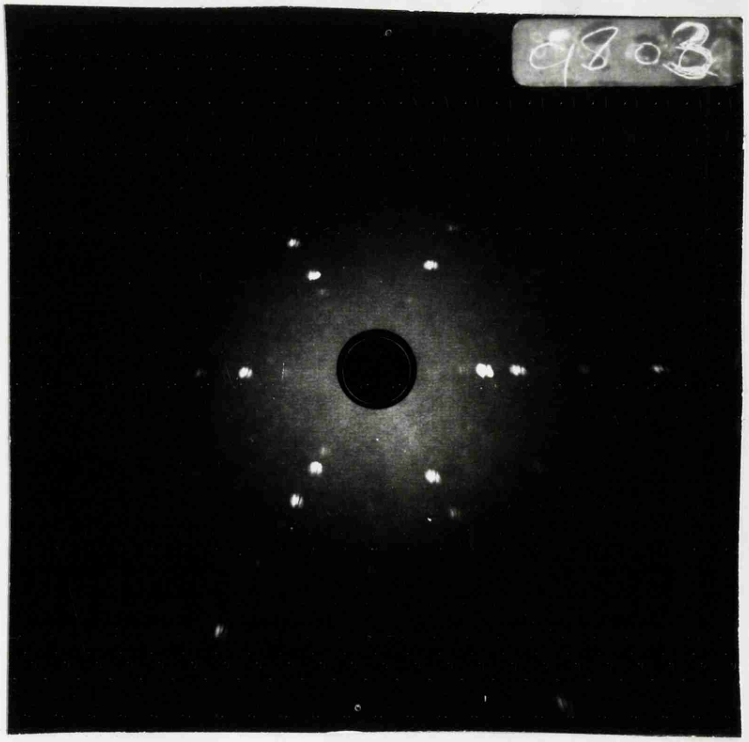

Figure (4.7) Laue-reflection X-ray photograph of antimony along the trigonal (z) axis.

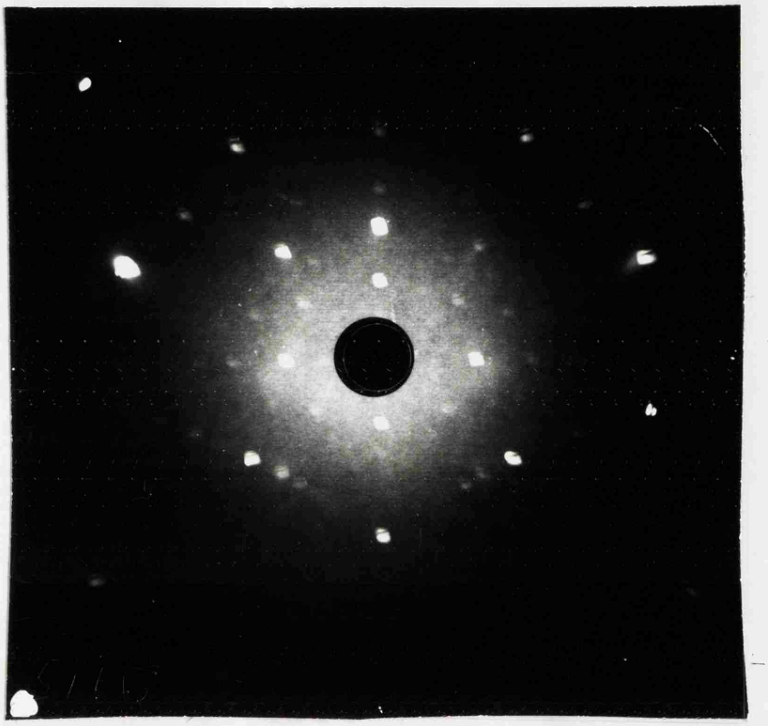

Figure (4.8) Back reflection photograph of antimony taken with the X-ray beam in a bisectrix direction and the cleavage plane horizontal. The Pseudo three fold spot (ringed) lies in the lower half of the photograph, so that for *a* + *z* axis chosen vertically upwards the + *y* axis lies in the direction of the incident X-ray beam.

structure). The normals to the $\{100\}_{fcr}$ planes exhibit pseudo-four fold symmetry and normals to the $\{111\}_{fcr}$ planes pseudo-three fold symmetry (Akgöz & Saunders 1971). Referred to the primitive rhombohedral unit cell, these pseudo-axes are the normals to the $\{011\}_{Prh}$ and $\{100\}_{Prh}$ plane respectively. Hence the quadrant in the mirror plane formed by the $+y$ and $-z$ axes (and $-y$ and $+z$ axes) contains a pseudo-four fold axis and that formed by the $+y$ and $+z$ axes (and $-y$ and $-z$ axes), contains pseudo-three fold. When a back reflection photograph is taken with the X-ray beam incident along a bisectrix axis of the crystal with its cleavage plane horizontal a pattern with mirror symmetry is obtained. The photograph also shows a spot corresponding to the pseudo-three fold reflection. (Details for bismuth can be found in the publication of Brown *et al* (1968), for As-Sb alloys in Akgöz 1974, and for pure antimony, see Figures 4.6, 4.7 and 4.8).

If the $+z$ direction is chosen to be the outward normal to the cleavage surface, then the $+y$ direction is determined since the pseudo-three fold reflection must be in the $+y$, $+z$ (or $-y$, $-z$) quadrant. The angles between pseudo-axes and $+y$ axis are listed in Table 4.1.

4.5 Growth parameter for the present system

The binary phase diagram for the antimony-tin alloys is shown in Figure 4.3-4. We are concerned here only with the extreme antimony-rich end. In fact, a requirement for this work is that the composition of the alloys be so well to the right of the diagram, that they are beyond the limit of the two-phase region; as indicated by the dotted lines, the actual composition at which phase separation would ensue is by no means certain. Therefore, care has been taken to examine

TABLE (4.1) Angles between Pseudo-axes and $+y$ axis in A7-structure semimetals (Akgöz and Saunders 1974)

Material	Pseudo-three fold angle between $[\bar{1}2\bar{1}]_{Prh}$ and the normal to $(010)_{Prh}$	Pseudo-four fold angle between $[\bar{1}2\bar{1}]$ and the normal to $(010)_{Prh}$
As	17.167^{o}	31.717^{o}
Sb	18.317^{o}	33.496^{o}
Bi	18.366^{o}	33.578^{o}

the alloy crystal to ensure that they are single phase. Microscopic studies and back reflection Laue photographsof the single crystals showed no evidence of a second phase; X-ray powder photographs showed only the rhombohedral phase of antimony itself.

The two main factors which have to be taken into account in deciding the growth conditions necessary for avoiding constitutional super cooling are:

1 - The growth rate must be slow

2 - The temperature gradient at the interface must be large.

Both these conditions were met in the zone levelling equipment used for crystal growth. The necessary growth conditions were quantified by putting the various growth parameters in the following equation established by Tiller *et al* (1953) which showed that the critical growth parameters obeyed the criterion

$$\frac{R}{G} \leq \frac{D_\ell}{m(C_s - C_\ell)} \qquad (4.5)$$

where R is the growth rate

G is the temperature gradient in the melt at the freezing interface

D_ℓ is the diffusion coefficient of the solute in the melt.

m is the slope of the liquidius line at C_ℓ

C_s, C_ℓ are the solute concentrations at the interface in the solid and liquid respectively.

Thus, for a crystal of given composition and for a furnace providing a given temperature gradient, there is a certain critical growth rate above which constitutional super cooling will occur and have an important influence on the crystal structure. In the present experiment, the critical growth rate (R_c) for the cost concentrated sample grown (Sb + 1 at % Sn) was calculated from the formula,

$$R_c = \frac{GD_\ell}{m(C_s - C_\ell)} \qquad (4.6)$$

using the approximate values for the parameters:

$G \sim 40^{\circ}C/cm$

$m \sim 2.3^{\circ}C$/atomic% (from phase diagram)

$C_s - C_\ell \sim 4$ at % (also from the phase diagram)

$D_\ell \sim 5 \times 10^{-5}$ cm^2/S (estimated from various values of the self diffusion and interdiffusion coefficient in Sb-Sn alloys, given by Belashchenko *et al* 1971).

This gives $R_c \sim 0.22$mm/min. When attempts were made to grow crystals at a faster rate than this, poor results were obtained; this is almost certainly because constitutional super cooling had set in.

Subsequent attempts at much slower growth rate (with growth rate of 2.4 mm/hr.) were more successful in their outcome, (the temperature gradient was kept at $40^{\circ}C$). The successful crystals were pure antimony, 0.5 at % Sn, 0.75% Sn, and 1 at % Sn. Homogeneous single crystal growth was then accomplished by several zone passes. Inspection of the alloys by chemical etching and X-ray analysis indicated that the entire charge was easily converted into single crystals and tended to grow in a direction perpendicular to the trigonal direction, as observed and discussed on the basis of thermal conductivity by Yim and Dismukes (1967).

4.6 Sample preparation

The galvanomagnetic effect employed here required samples of a rectangular bar shape (about $1.5 \times 0.25 \times 0.25$ cm). The sizes were measured with a travelling microscope with an error about 0.001 cm, oriented along the x, y and z axes. Crystals were aligned

using the symmetry shown on Laue back-reflection photographs (and the sense of the y-axis checked by Laue back-reflection orientation) as described in section (4.4a).

Antimony and its dilute alloys cleave easily along the (111) planes. To prevent damage to the material, all the cutting and polishing was performed by a servomet spark machine (Metal Research Ltd. Royston). The main advantage of the technique is that because the cutting action results from electrical spark erosion, no mechanical stresses are induced by the pressure of cutting (for more detail see Lichnowski 1975). Slight mechanical deformation occurs only at the sample interface, which can readily be removed by chemical etching.

4.7 Sample contact

The four-probe configuration usual for galvanomagnetic effect measurements was employed; that is, two longitudinal contacts separated by about 0.8 cm and two transverse contacts centred on the sample. A number of methods for attaching electrical contacts to the sample were considered, and soldering was the method adopted. Voltage probes were of 0.002" diameter copper wire soldered to the sample with a low melting point (95^{o}C) alloy (32% Pb - 16% sn -52%Bi) and positioned well away from the sample ends to minimize Hall-field shorting (Volger 1950); the contact diameter was 0.01". The sample holder was identical in design to that used by Akgöz (1974)

4.8 Measuring System

The block diagram shown in Figure (4.9) represents the main features of the system used for measuring the sample voltage and

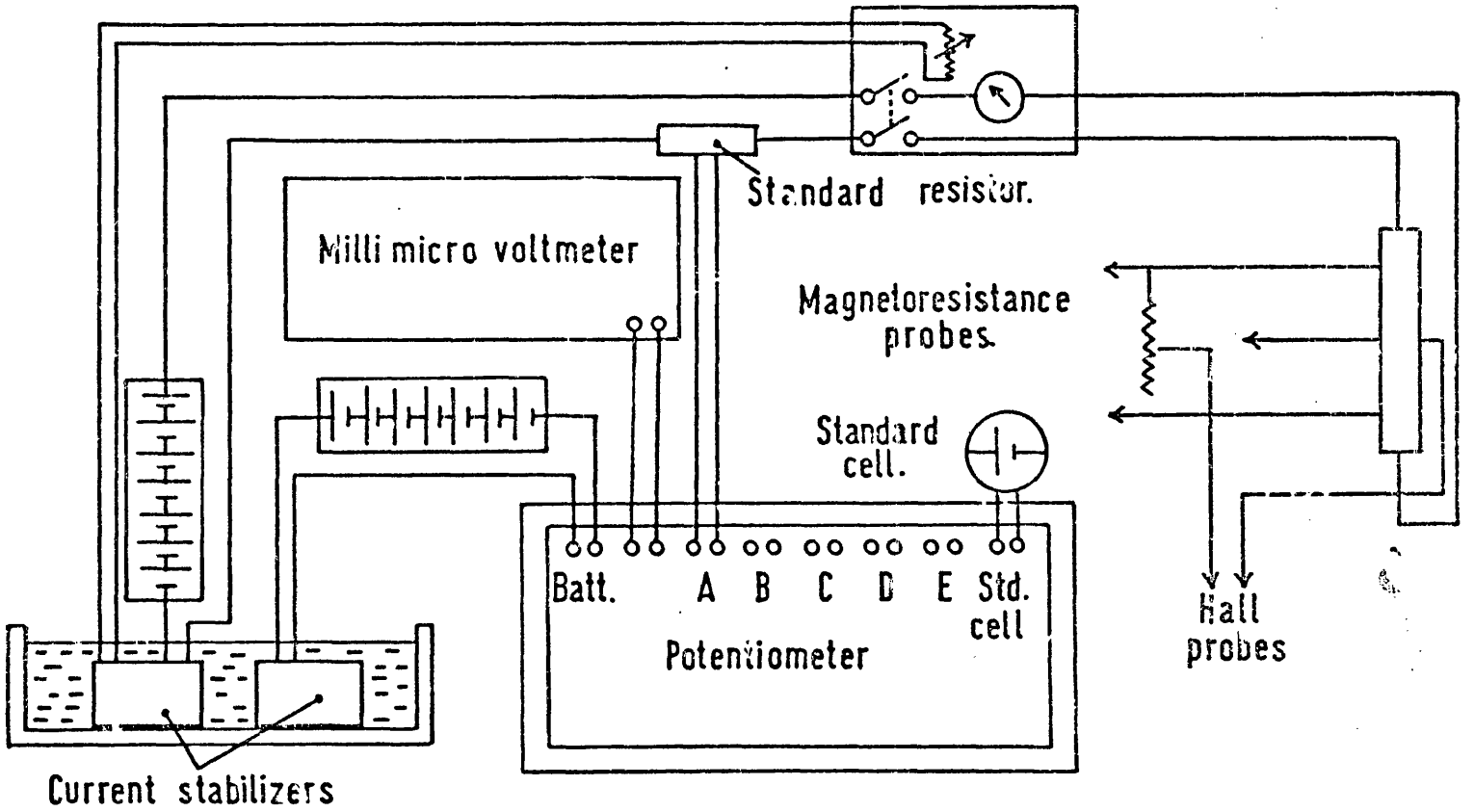

Fig.(4.9) The measuring system

thus for the determination of galvanomagnetic tensor components. Essentially it was the same system as that used for measurements of the low field galvanomagnetic tensor coefficient in antimony (Öktü and Saunders 1967), in arsenic (Jeavons and Saunders 1969) in bismuth (Sümengen and Saunders1971) and arsenic-antimony alloy by using field dependent tensor (Akgöz and Saunders 1974).

The potentiometer was a precision instrument (Pye type 7600) based on the decade principle (Stout 1960) and switches were employed throughout; the smallest switched voltage step was 0.1 μv. Akeithley (type 149) electronic millimicro-voltmeter was used as a null-detector for measurements at the nanovolt level. This instrument has a sensitivity comparable to the best light-beam galvanometer systems and combines the advantages of fast response, high input resistance and robustness. The resolution of the instrument was sufficient to detect signals below the nanovolt level with stability of 10 nanovolts in 24 hours.

Because of the inherent isolation and line pick-up problems involved in these types of null detectors, the elimination of severe mains pick-up required a modification (see Jeavons 1969) mainly confined to some isolations, such as the mains transformer and change of the original 50 HZ chopper frequency to a value of 60 HZ. Stray thermal e.m.f.'s in the measuring circuit were minimized by using copper wires throughout; connections were carefully cleaned and clamped where possible. "Low thermal" solder (70% cd + 30% sn) was used whenever soldering was absolutely necessary.

A sample current of about 0.5 amps (with a stability of better than 1 part in 10^6 was used), and was measured from the drop across a 0.01Ω standard resistance. The current stabilizer,

standard resistance and standard cell were all kept in an oil bath to prevent temperature changes (for more details see Jeavons 1969).

The magnetoresistivity measurements were usually made at three fixed temperatures (Liquid Nitrogen, dry ice in acetone and room temperature). The sample holder was constructed from stainless steel and since the sample immersed directly into these liquids, there were no problems resulting from temperature gradients.

4.9 The magnetic field alignment

Since the magnetoresistivity components are a function of the magnetic field, an accurate knowledge of magnetic field strength is necessary to reduce the errors. The magnet was calibrated by Newport Equipment Ltd., and re-calibrated in this laboratory by two different methods: firstly by the nuclear magnetic resonance technique (using an ageous solution of a lithium salt) to an accuracy of higher than ±2% (see J.Sci.Instrum. 36 page 481 1959) and secondly by a gaussmeter (type 750); this instrument was capable of measuring from zero to 1,000 G on the low range and from zero to 50,000 G on the high range with an error less than ±1.5%. Both these ranges and zero Gauss Chamber enabled instrument calibration before every measurement. Field values were always set by increasing the magnet coil current, finishing at saturation. The magnet coil current was not reversed. The magnet was rotated to reverse the magnetic field and to establish the various orientations with respect to the crystal. The magnetic field and sample were centralised on the axis of rotation. Sample alignment in the magnetic field was achieved mechanically by reference to the planar pole-tip faces.

4.10 The measuring procedure

To remove the error voltage due to exact probe positioning and to separate Hall and magnetoresistance components, both current and magnetic field reversal were employed. The measurement procedure was as follows:

1. The apparatus was switched on and left overnight to allow it to establish stability.
2. The magnetic field orientation was set and the Gaussometer calibrated (see previous section).
3. The potentiometer was standardised and the sample current stabilizer put into operation.
4. The potentiometer was switched on to measure the sample voltage and the system checked for drift.
5. The sample voltage and magnetic field were measured at the required fields and directions.
6. The sample current was reversed and the measurements repeated.

4.11 The results

Figures (4.10) and (4.11) represent the temperature dependence between 4.2°K and 300°K for components of the zero field resistivity of antimony - tin (from 0.5 at % to 1.7 at % tin) and antimony-germanium (from 1.16 at % to 2.2 at % germanium) alloy single crystals. The experimental data of Akgöz and Saunders (1974) in arsenic-antimony alloy are also shown for comparison.

The magnetoconducitivity tensor components $\sigma_{ij}(B)$ have themselves been directly related (Akgöz and Saunders 1974) to the band model parameters as was discussed in chapter three, and to obtain these parameters, measurements have been made of certain components of $\rho_{ij}(B)$. Results obtained at 77°K, 196°K and 300°K for each sample are shown in figures (4.12) to (4.25) for pure antimony, antimony-tin and antimony-germanium alloys single crystals. The experimental data are given by the points. The curves are the results of theoretical calculations with choice of parameters to best fit the experimental data. The y-cut sample in antimony-germanium alloys was misorientated by 14° from the xz-plane, for which reason the mirror plane is shifted by about 15° from the z-direction in the figures (4.22) and (4.23).

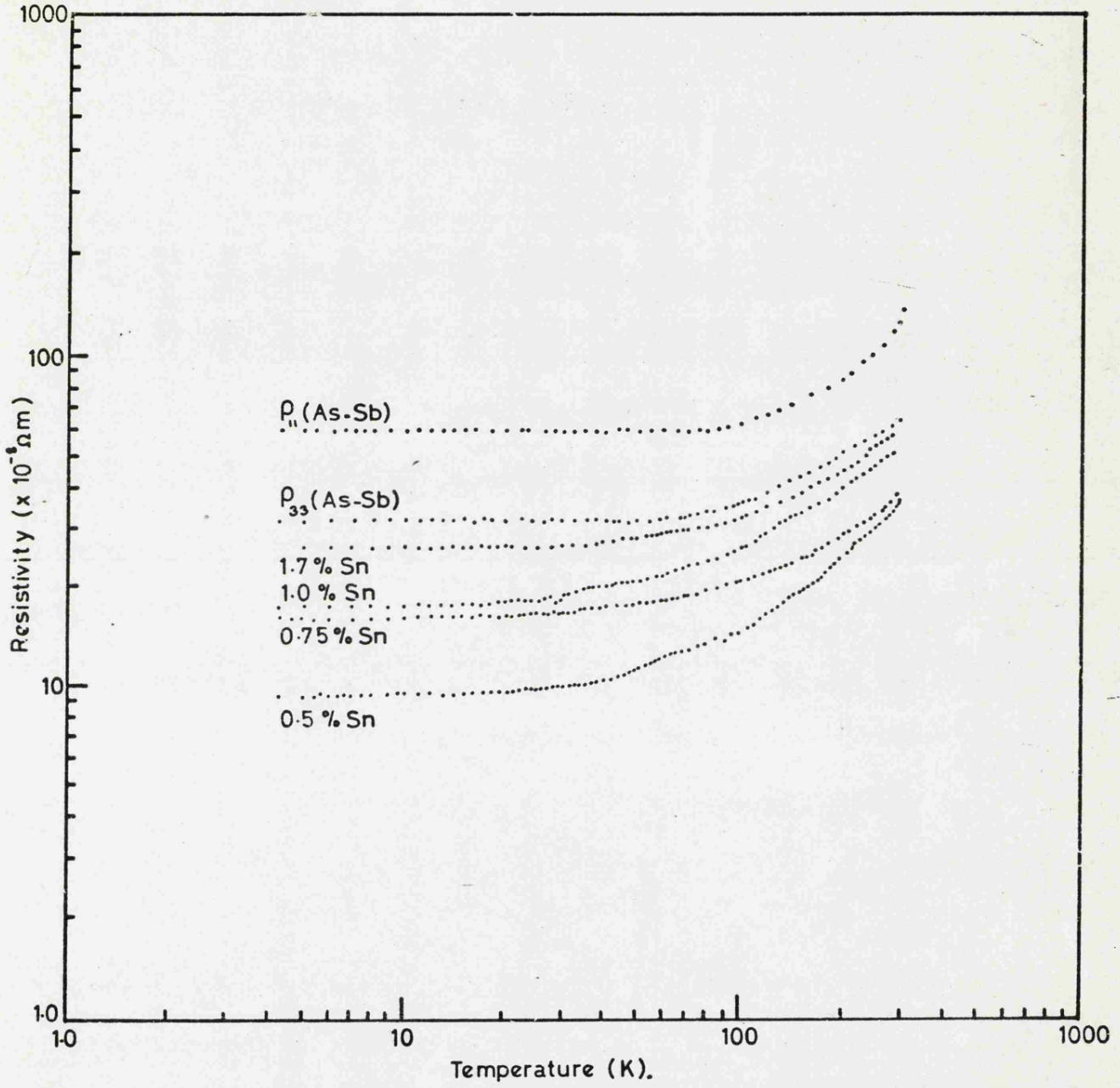

Figure (4.10) The temperature dependence of the component ρ_{11} and ρ_{33} of the resistivity tensor in antimony tin alloys (present work) and arsenic-antimony alloys (Akgöz and Saunders 1974).

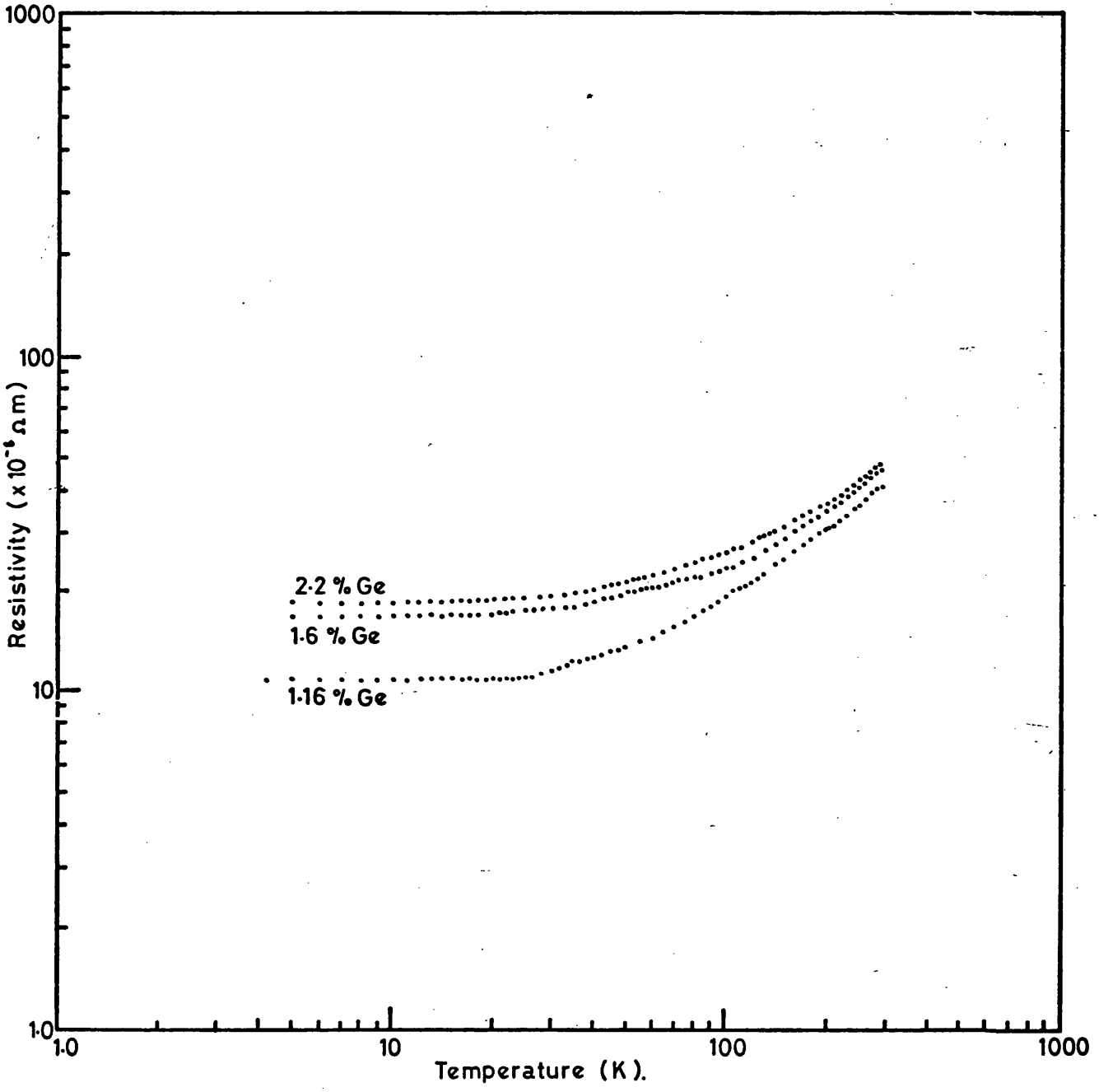

Figure (4.11) The temperature dependence of the component ρ_{11} of the resistivity tensor in antimony-germanium alloys.

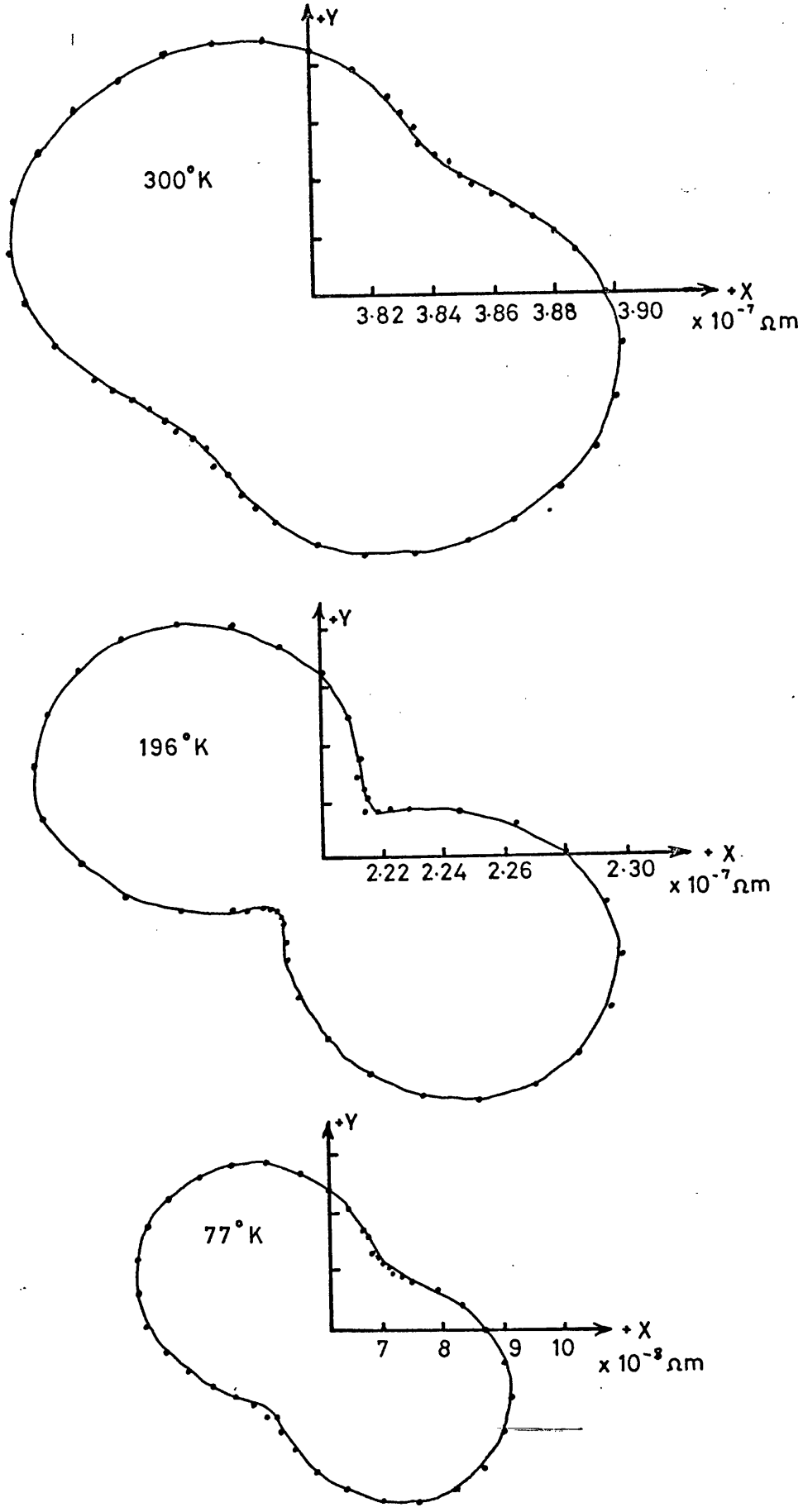

Fig. 4.12 Angular dependence of ρ_{11} (B) at B = 1.33T. B is in X-Y plane of Antimony.

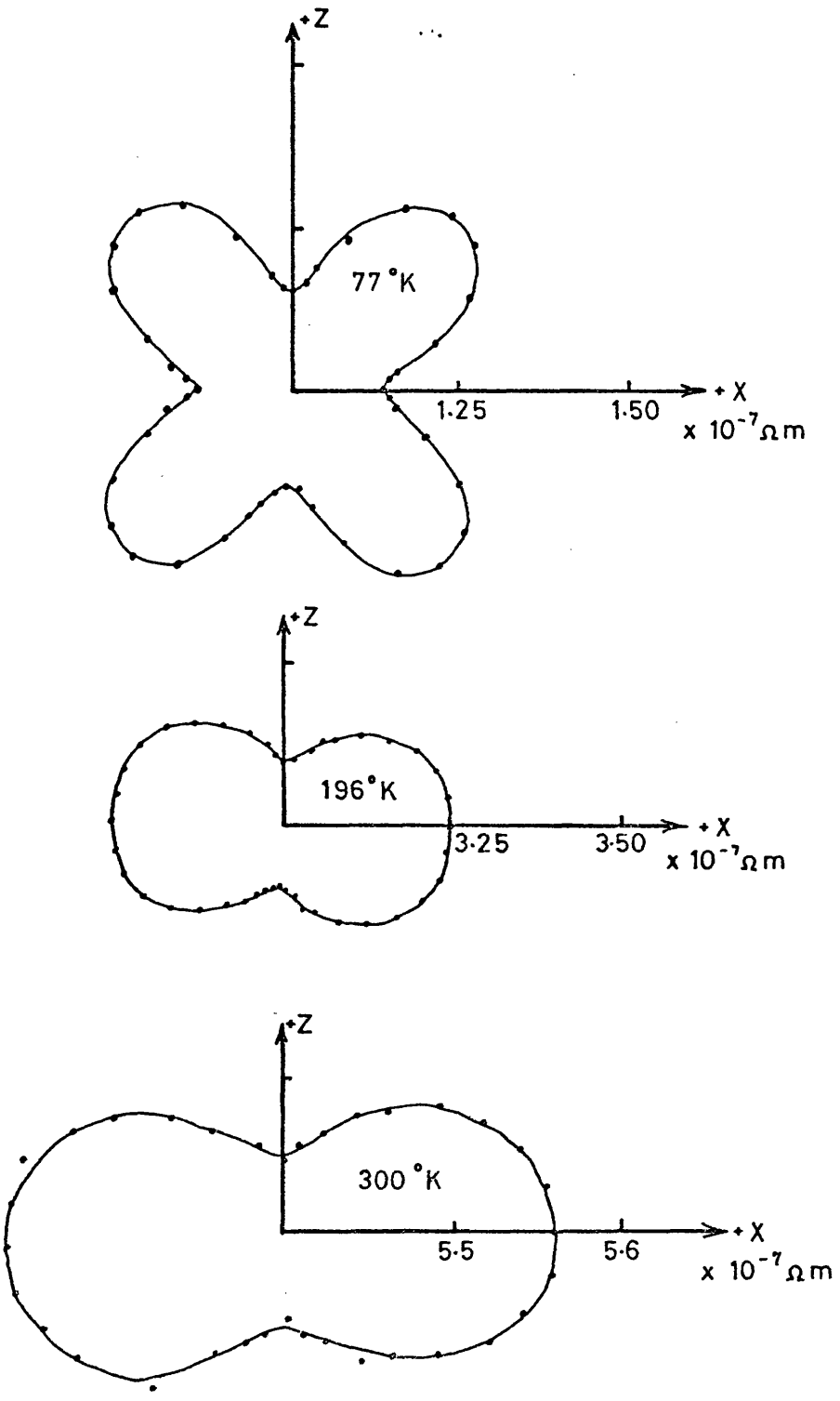

Fig. 4.13 Angular dependence of $\rho_{\perp}$ (B) at B = 1.33T. B is in X-Z plane of Antimony.

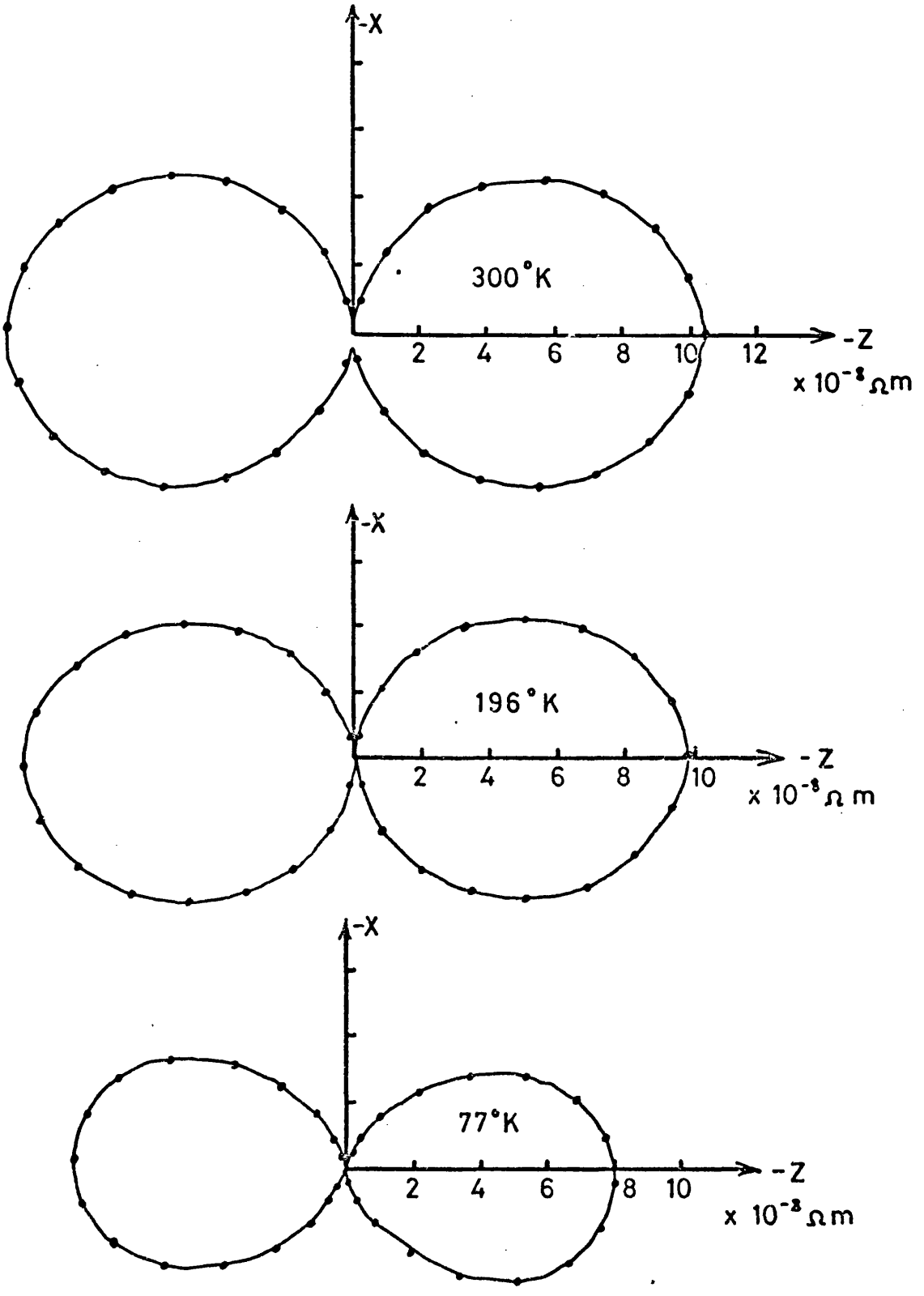

Fig.4.14 Angular dependence of ρ_{21} (B) at B = 1.33T. B is in X-Z plane of Antimony.

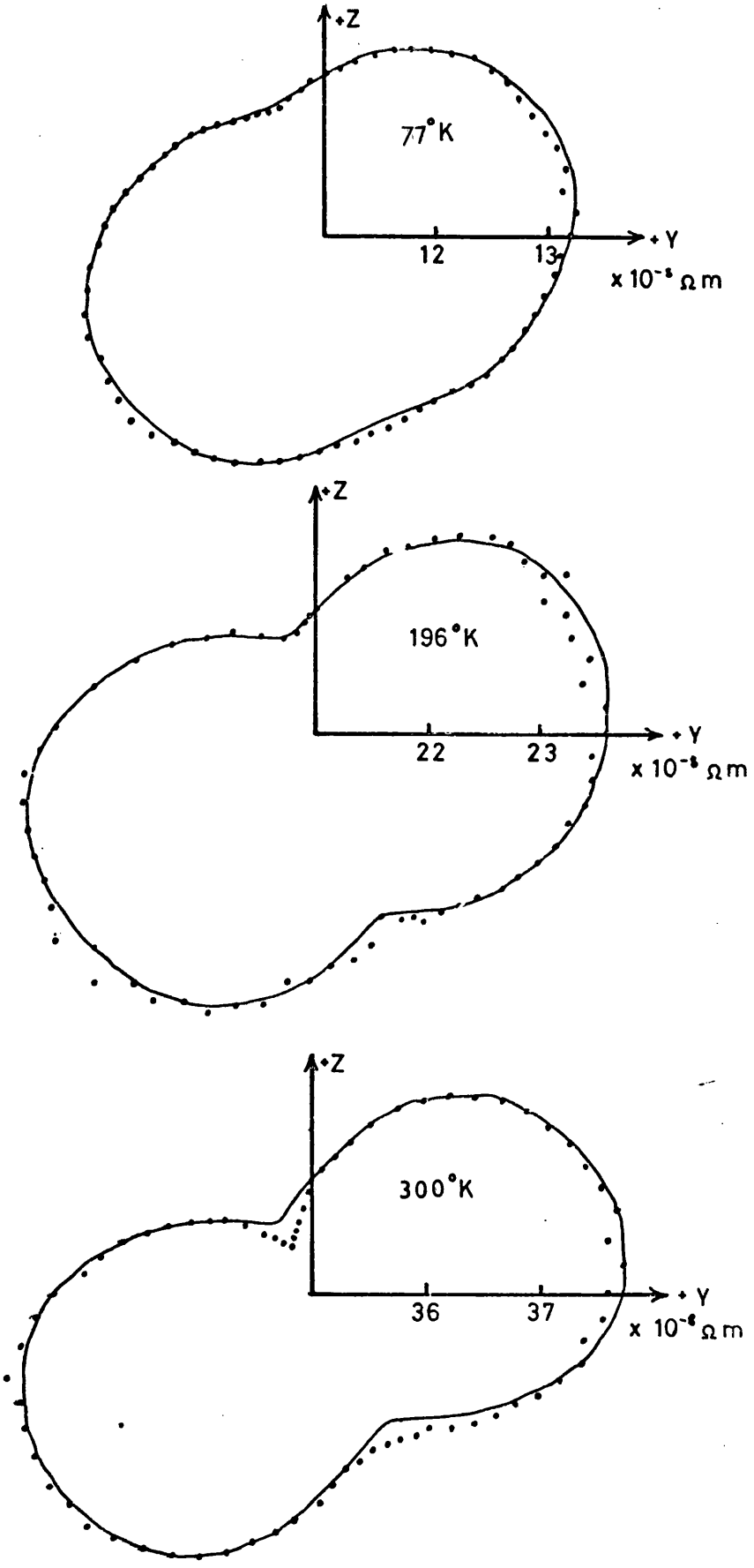

Fig. 4.15 Angular dependence of $\rho_{\perp}$ (B) at B = 2.19T for 300°K, B = 1.33T for 77°K and 196°K. B is in Y-Z plane of (Sb 0.5 at % Sn) alloy.

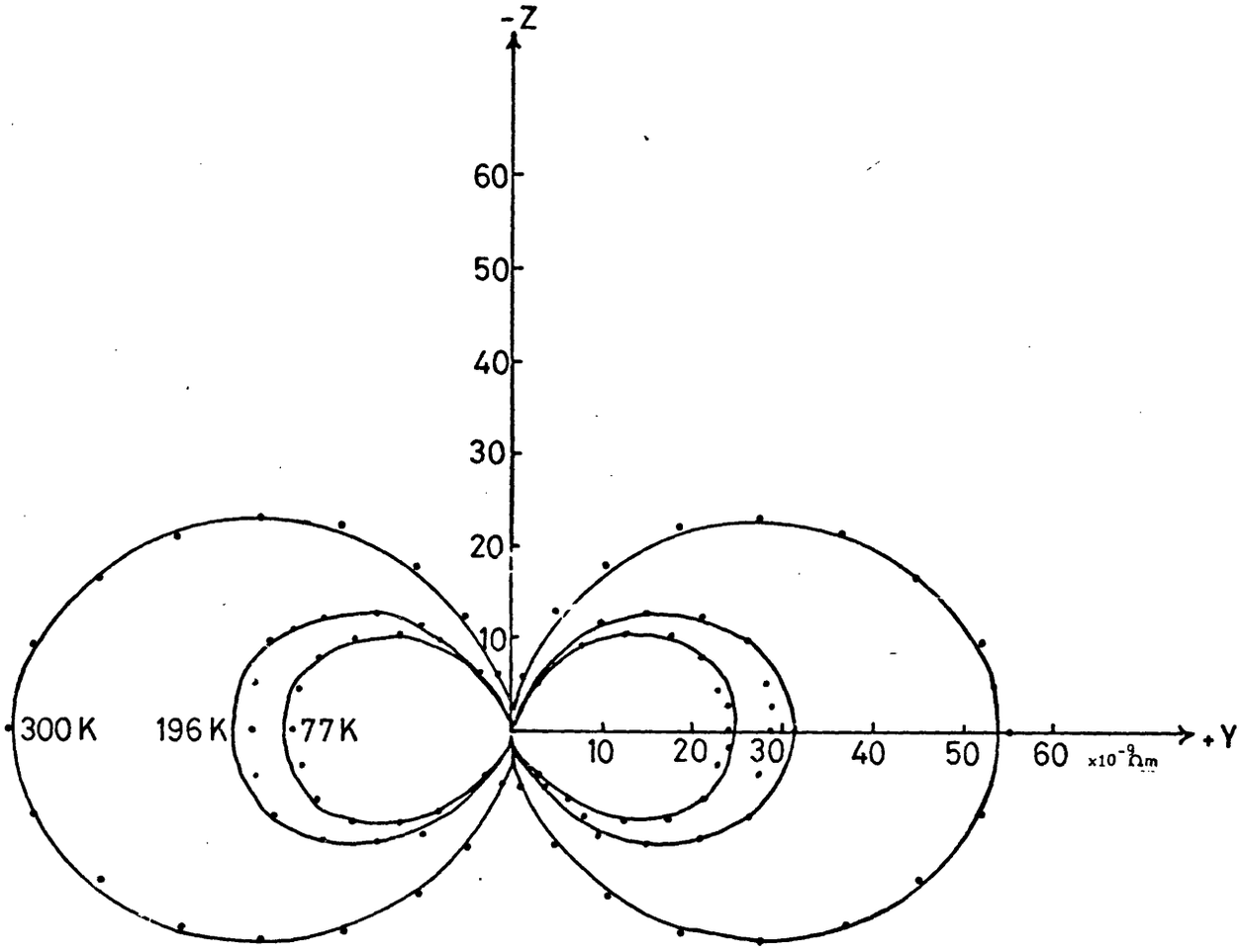

Fig. 4.16 Angular dependence of ρ_{31} (B) at B = 2.19T for 300°K, B = 1.33T for 77°K and 196°K. T is in Y-Z plane of (Sb 0.5 at% Sn) alloy.

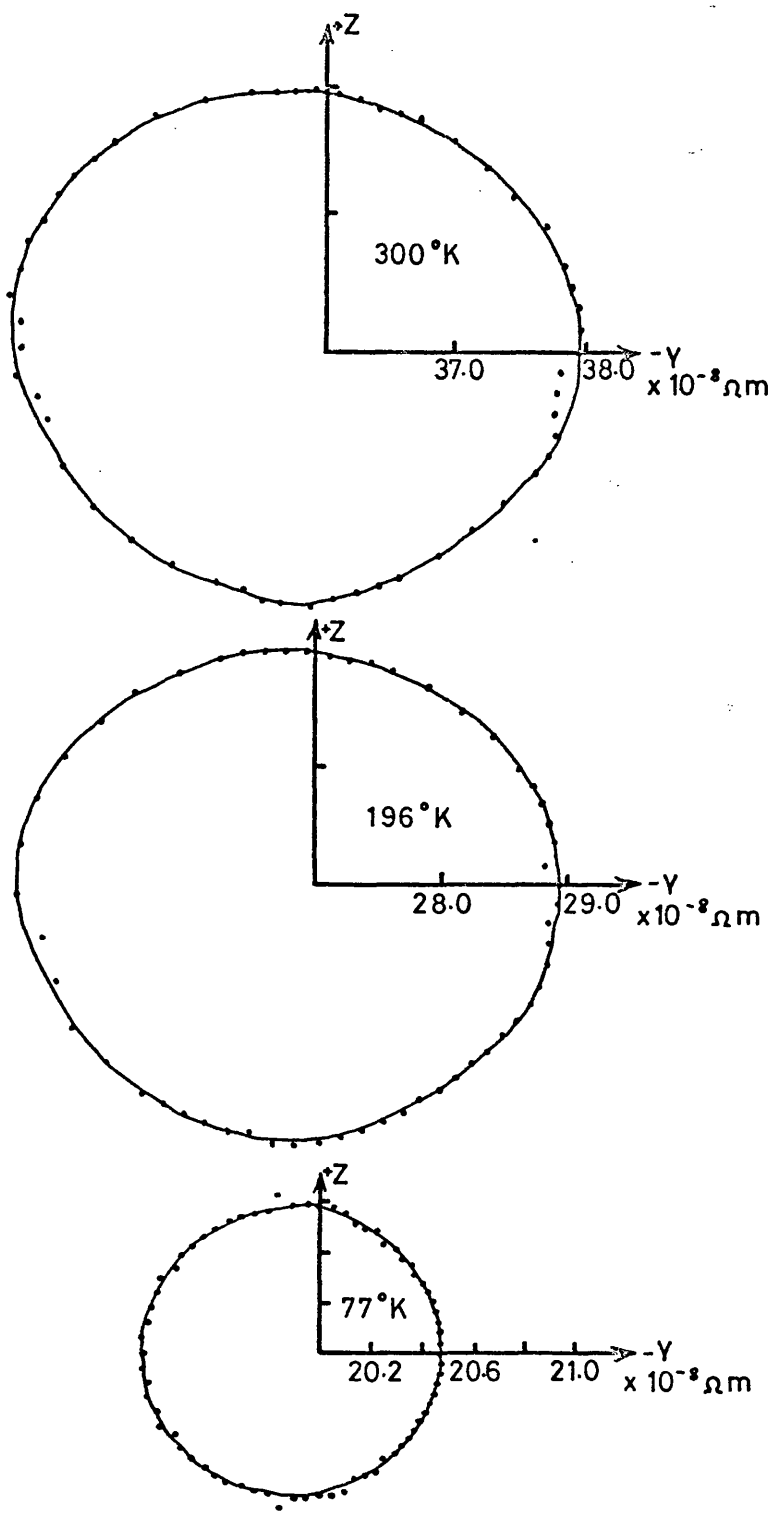

Fig. 4.17 Angular dependence of $\rho_{\perp}$ (B) at B = 1.33T for 77°K, B = 2.19T for 196°K and 300°K. B is in Y-Z plane of (Sb 0.75 at % Sn) alloy.

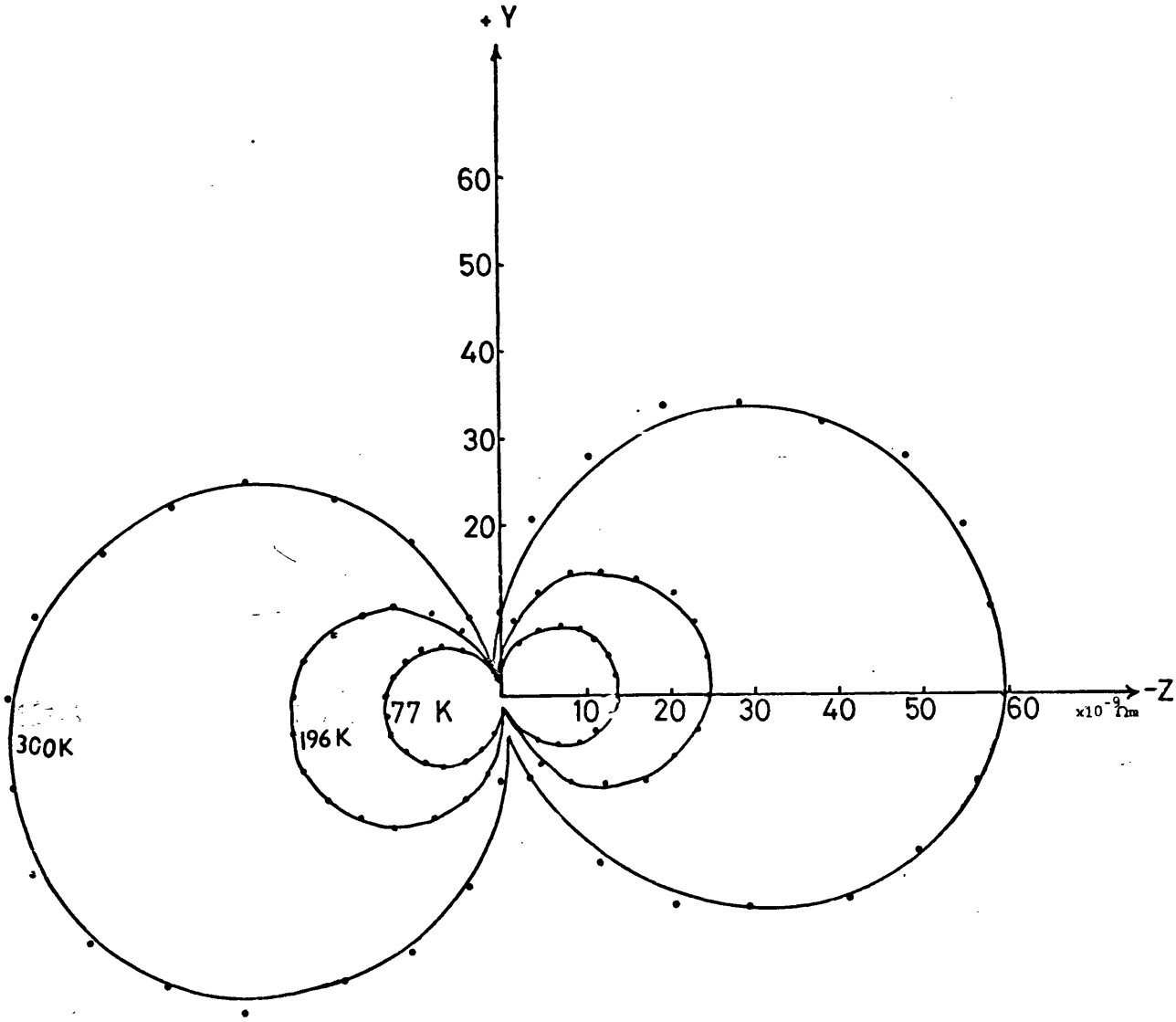

Fig. 4.18 Angular dependence of ρ_{21} (B) at B = 1.33T for 77°K, B = 2.19T for 196°K and 300°K. B is in Y-Z plane of (Sb 0.75 at % Sn) alloy.

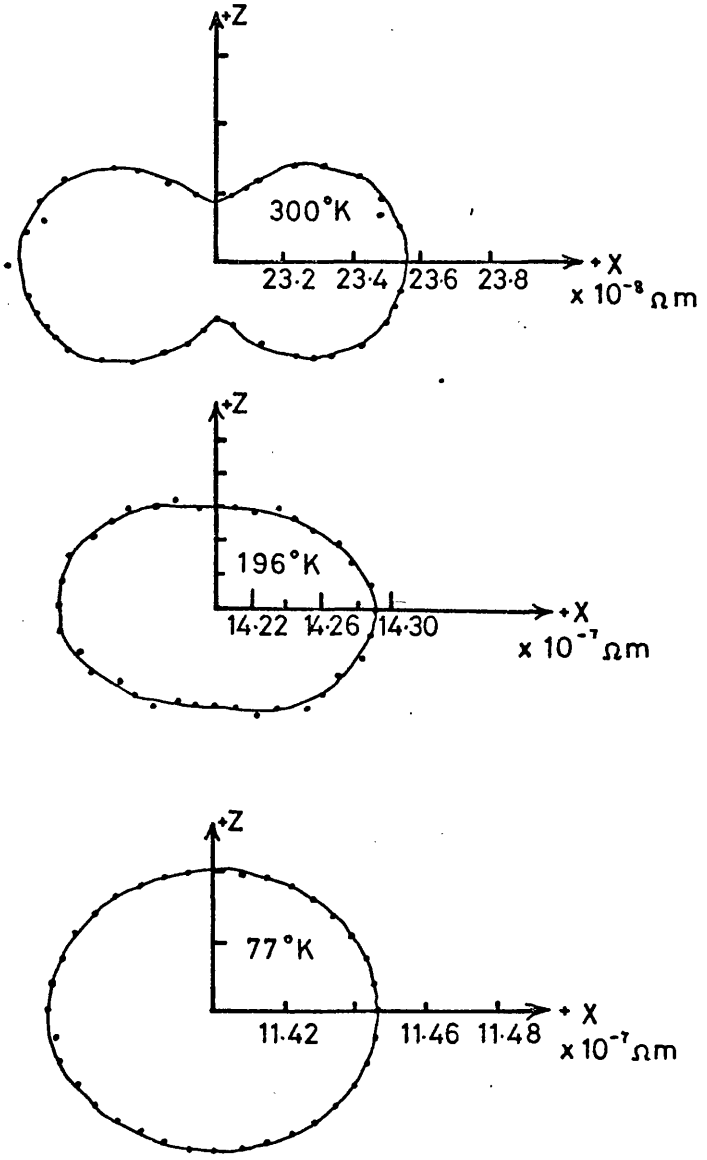

Fig. 4.19 Angular dependence of $\rho_{\perp}$ (B) at B = 2.19T for 300°K, B = 1.33T for 196°K and 77°K. B is in X-Z plane of (Sb 1.0 at % Sn) alloy.

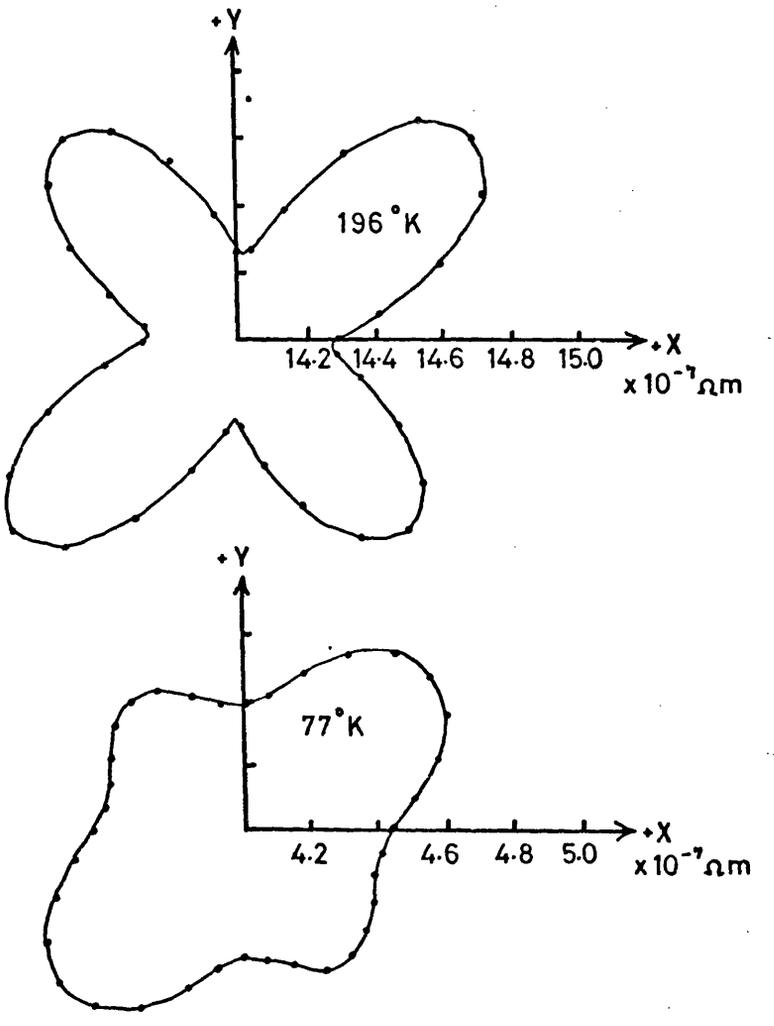

Fig. 4.20 Angular dependence of ρ_{33} (B) at B = 1.33T. B is in X-Y plane of (Sb 1.0 at % Sn) alloy.

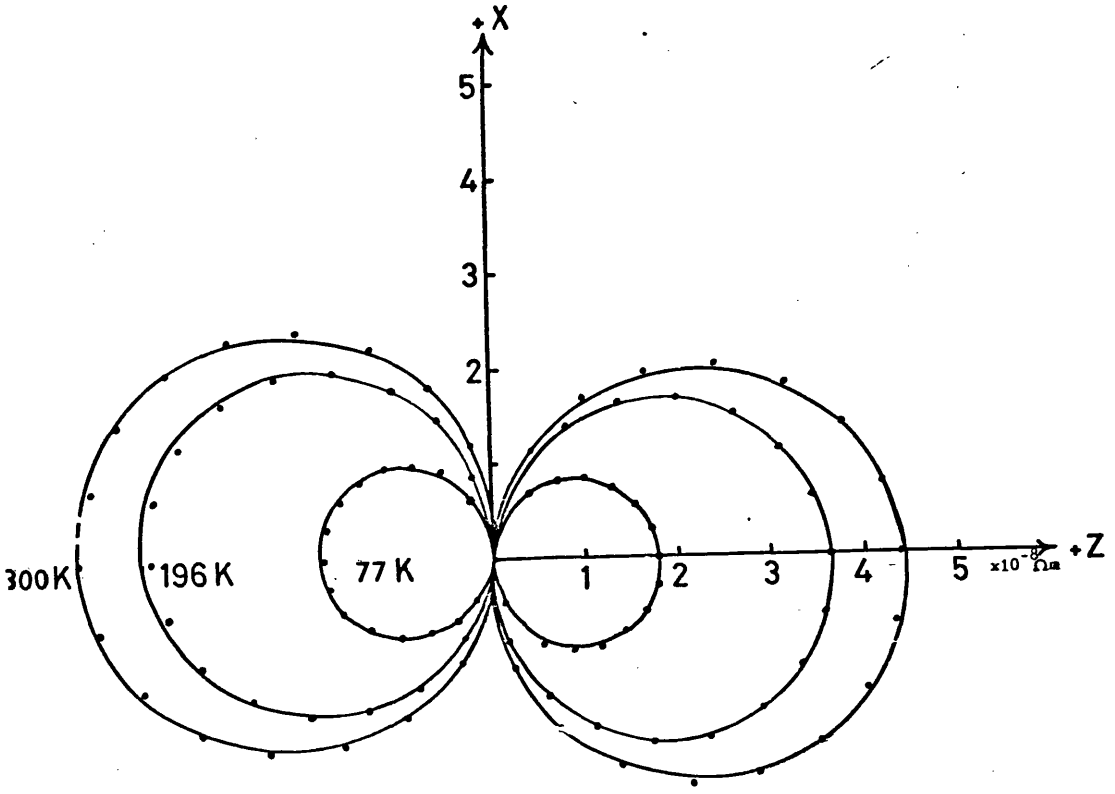

Fig. 4.21 Angular dependence of ρ_m (B) at B = 2.19T for 300°K, B = 1.33T for 196°K and 77°K. B is in X-Z plane of (Sb 1.0 at % Sn) alloy.

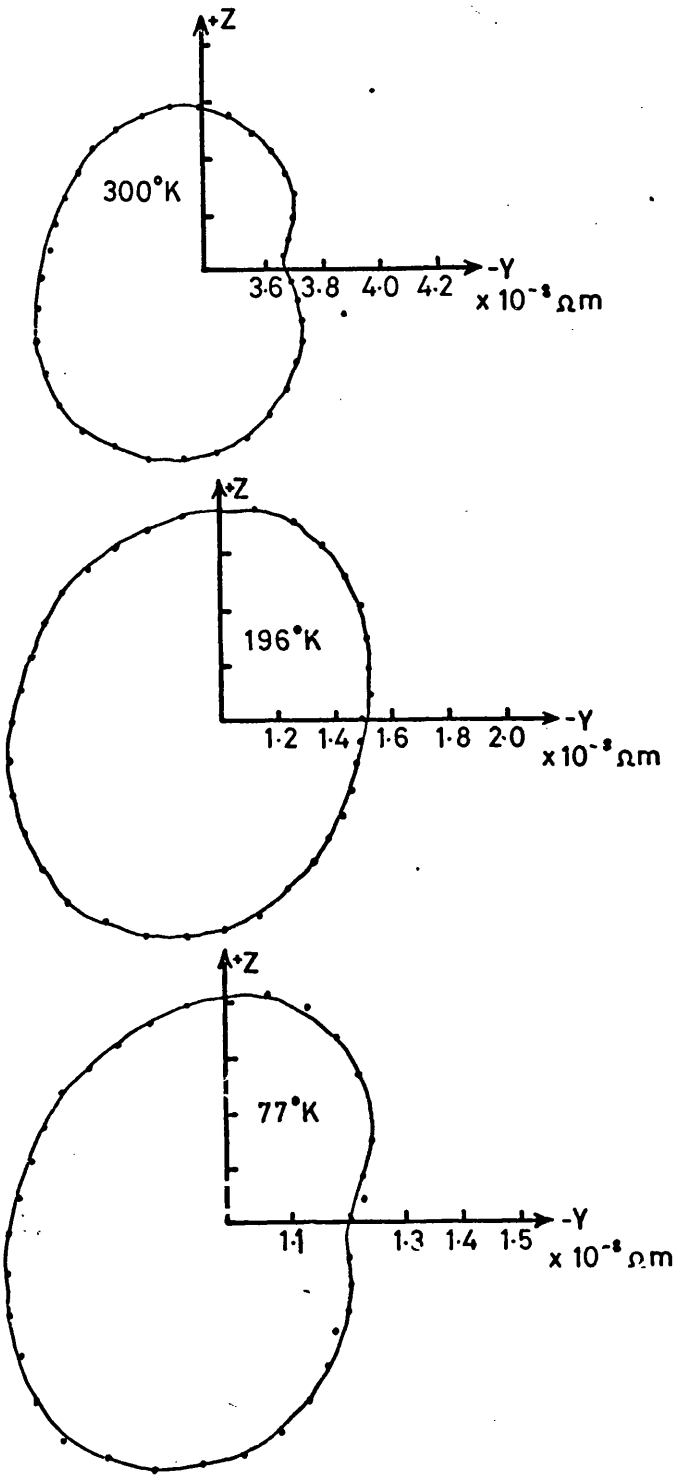

Fig. 4.22 Angular dependence of $\rho_{\perp}$ (B) at B = 2.19T for 300°K, B = 1.33T for 196°K and 77°K. B is in Y-Z plane of (Sb 1.16 at % Ge) alloy.

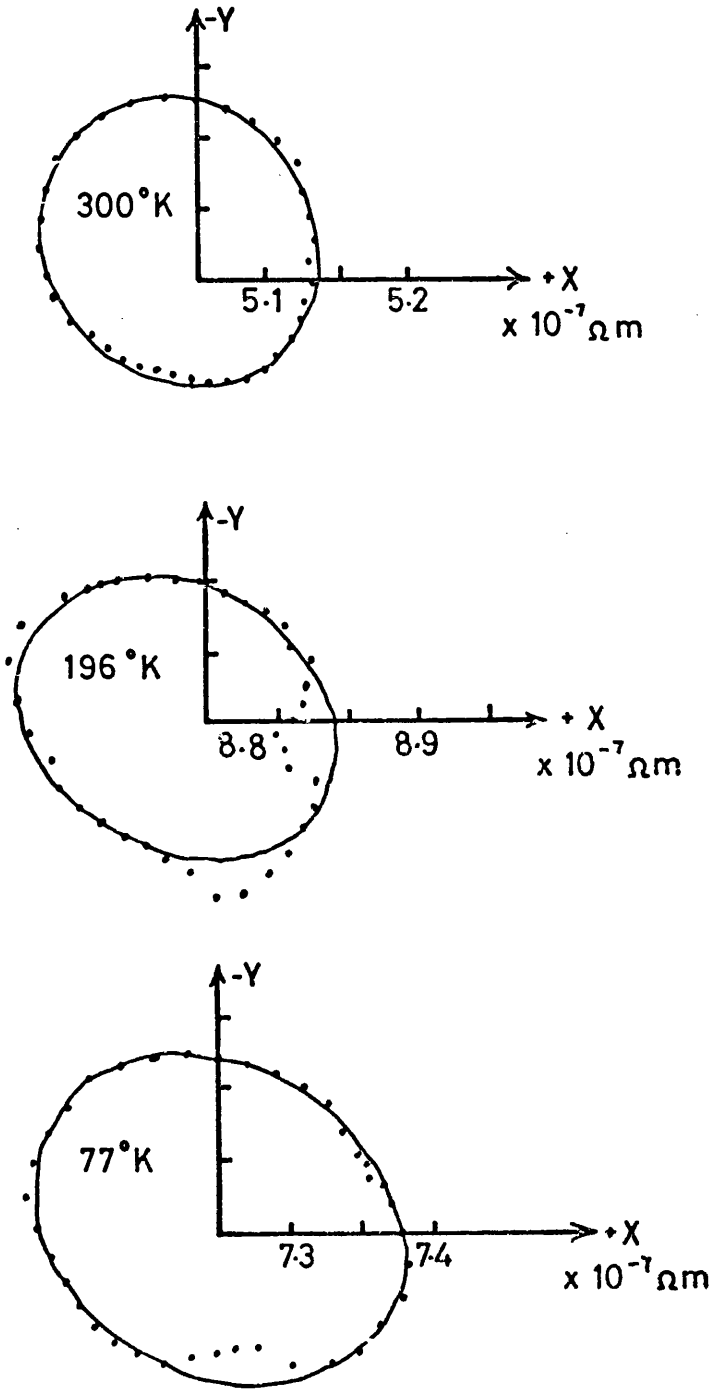

Fig. 4.23 Angular dependence of ρ_{33} (B) at B = 2.19T for 300°K, B = 1.33T for 196°K and 77°K. B is in X-Y plane of (Sb 1.16 at % Ge) alloy.

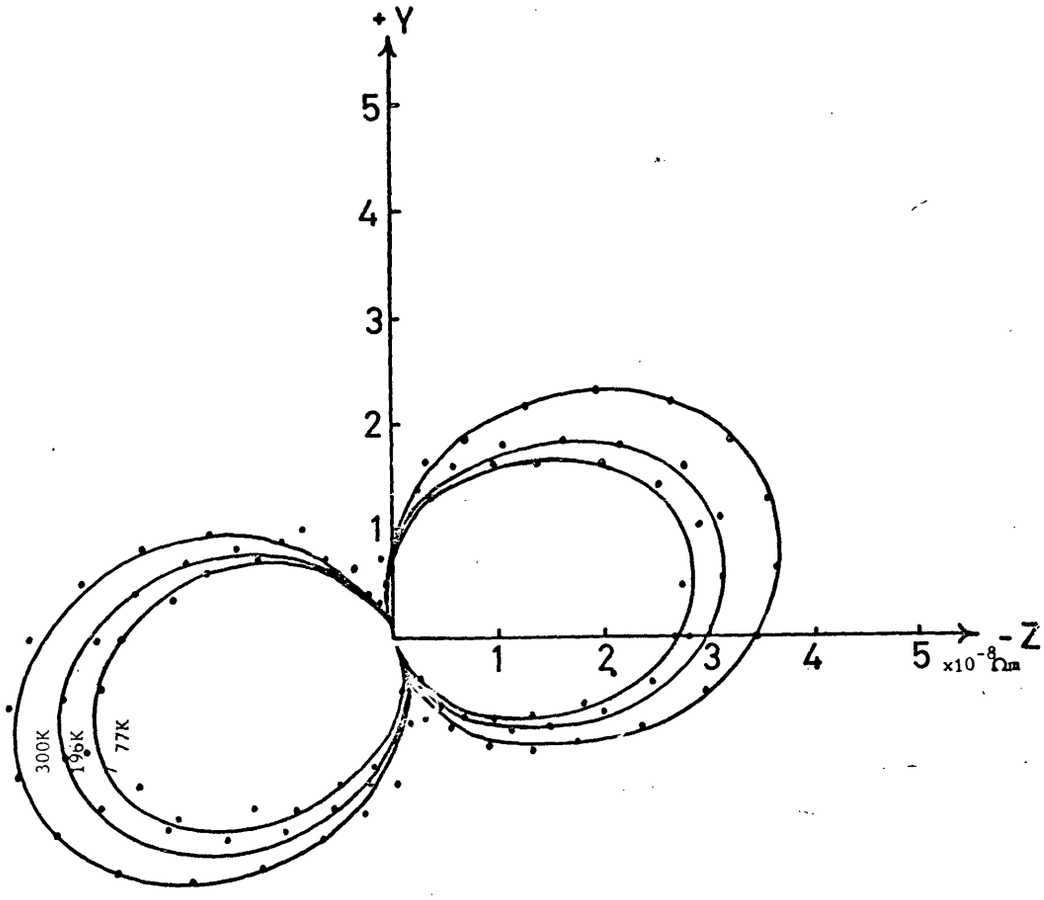

Fig. 4.24 Angular dependence of ρ_{12} (B) at B = 2.19T for 300°K, B = 1.33T for 196°K and 77°K. B is in Y-Z plane of (Sb 1.16 at % Ge) alloy.

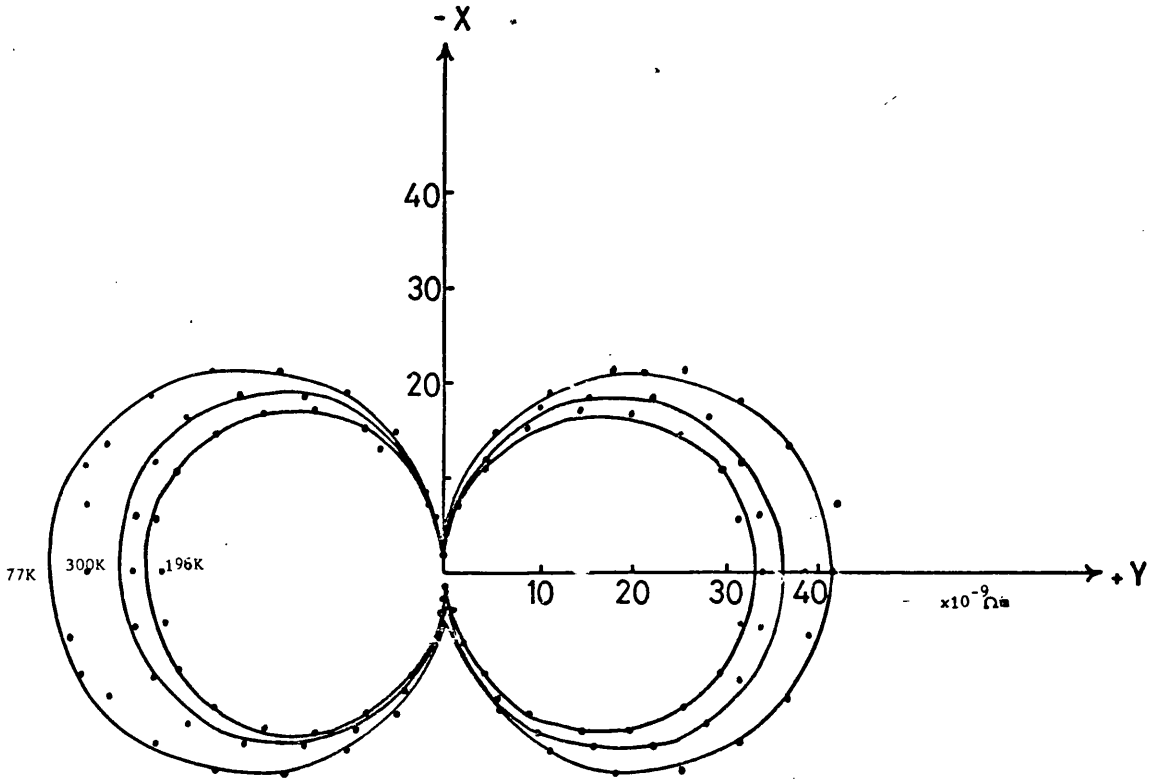

Fig. 4.25 Angular dependence of ρ_{13} (B) at B = 2.19 for 300°K, B = 1.33T for 196°K and 77°K. B is in X-Y plane of (Sb 1.16 at % Ge) alloy.

CHAPTER FIVE

COMPUTATION OF THE BAND PARAMETERS

5.1 Introduction

Ten parameters namely the principal electron and hole mobilities (μ_i and ν_i respectively (where i=1,2, and 3)), the number of carriers (N,P) and tilt angles (θ_μ and θ_ν) can be obtained as a function of temperature and impurity concentration, from the magnetoconductivity tensor components by means of the equations derived by Akgöz and Saunders (1974). Although in principle a direct solution of these equations can be obtained, this is impractical because the magnetoconductivity tensor components depend on these parameters in a complicated way. A direct solution by the elimination of the unknown variable is not only impractical but also the adoption of such a procedure would magnify the experimental errors, because a high power of the measured coefficient would then become involved in the equations. Therefore, it is necessary to develop a different method of solution. By making use of a computer, there are many different approaches through which a solution can be obtained. One method is to estimate first the order of magnitude of the parameters, then to calculate magnetoconductivity tensor components for an arbitrary set of parameters selected from the estimated range, and then to compare the calculated values with the experimental values. This procedure would then be repeated until a satisfactory fit was obtained. A faster computer than was available is necessary for this method, which in any event is unnecessarily unwieldy.

An alternative method is to estimate some of the parameters by solving the equations among the set and then to change the rest arbitrarily. Such a method was developed by Freedman and Juretschke (1961) to analyse their low field galvanomagnetic results on antimony

at room temperature. This method still has disadvantages because a direct solution is used in part. It is inherently biased in favour of certain coefficients.

In 1967 Öktu and Saunders made a fresh approach in which the principle of a direct solution was abandoned. They analysed their low field galvanomagnetic results on antimony and antimony-tin alloys (high concentrations) by solving eight equations in nine variables and choosing the other two variables arbitrarily.

A much more satisfactory approach to the problem is to use a least-mean-square procedure in dimensional space; Jeavons and Saunders (1969) developed such a procedure to analyse their arsenic results, where the minimization is of a function defined by

$$\text{SUM} = \sum \left[w_J \left(1 - \frac{CAL(J)}{CO(J)} \right) \right]^2 \qquad (5.1)$$

On substitution of arbitrary values for the ten unknowns, a calculated value ($CAL(J)$) for a particular equation J in the set is obtained; $CO(J)$ is the corresponding measured value. W_J is a weighting factor used to put more emphasis on the most accurately measured coefficient; this method also provides a feed-back control for the values over which the variables must be swept for the minimizations of the term SUM in the above equation (5.1). The result is steady progress towards the best approximation. The initial trial-solution could take any value, provided that the appropriate sweeps are chosen and a sufficiently large number of cycles is allowed.

Akgöz and Saunders (1974) extended the Jeavons and Saunders (1969) procedure and analysed their arsenic-antimony alloy single crystal results by introducing a minimization program. The present work has developed from this line but has modified it.

The actual procedure adopted will now be discussed.

5.2 The method of calculation

The experimental results presented in chapter four, for both the magnetoresistance and Hall-effect in antimony and its alloy single crystals can now be quantitatively discussed on the basis of the Fermi surface model presented in chapter two. In chapter three, the theoretical expressions for magnetoresistivity tensor components have been formulated in terms of charge carrier densities and mobilities. A comparison between the theory and experimental data requires a fit to the equations involved in terms of the ten band parameters $\mu_1,\mu_2,\mu_3,\theta\mu,\nu_1,\nu_2,\nu_3,\theta\nu,N$ and P for antimony. The determination of these parameters provides basic information on the carrier transport properties of antimony and on the effect of alloying antimony.

Thus the major aim of this work is to analyse the polar data, which has been shown to be the most accurate by Akgöz and Saunders (1974), and the effect of varying the magnetic field strength, thus obtaining the model parameters, and then to compare it with those found by Öktü and Saunders (1967) from the low field components. Using the two band tilted ellipsoidal Fermi surface model, Akgöz and Saunders (1974) have obtained explicit expressions for the magnetoconductivity tensor $\sigma_{ij}(B)$ valid over the classical range of magnetic field. These equations have been extended here to analyse the data taken when the field is in the *XY*-plane, *XZ*-plane and *YZ*-plane, the equations developed for this analysis being presented in appendices II, III and IV respectively.

To transform from the measured components of the magnetoresistivity tensor to the magnetoconductivity tensor components, the following relations have been used:

$$\rho_{11}(B1,B2) = \frac{\sigma_{22}(B1,B2)\sigma_{33}(B1,B2) - \sigma_{32}(B1,B2)\sigma_{23}(B1,B2)}{|\sigma_{ij}(B1,B2)|}$$

$$\rho_{11}(B1,B3) = \frac{\sigma_{22}(B1,B3)\sigma_{33}(B1,B3) - \sigma_{32}(B1,B3)\sigma_{23}(B1,B3)}{|\sigma_{ij}(B1,B3)|}$$

$$\rho_{21}(B1,B3) = \frac{-\sigma_{21}(B1,B3)\sigma_{33}(B1,B3) - \sigma_{31}(B1,B3)\sigma_{23}(B1,B3)}{|\sigma_{ij}(B1,B3)|}$$

where $|\sigma_{ij}(B1,B2)|$ and $|\sigma_{ij}(B1,B3)|$ are the determinants of the magnetoconductivity tensor when $B3 = 0$ and $B2 = 0$ respectively. We can obtain the rest of the magnetoresistivity components by using the determinants of the magnetoresistivity tensor $|\rho_{ij}(B1,B2,B3)|$ for $B1 = 0$, $B2 = 0$, and $B3 = 0$ respectively.

Using these transformations and the expression for $\sigma_{ij}(B)$ given in the appendices II, III and IV, a minimization procedure has been used to obtain the best fit solution for the model parameters from experimental data $\rho_{ij}(B)$. From each sample two magnetoresistivity components at least have been measured as a function of the orientation of a magnetic field; one of the components is magnetoresistance and the other is the Hall component. As an example of the method, the experimental curves for the components $\rho_{11}(B1,B2)$, $\rho_{11}(B1,B3)$ and $\rho_{21}(B1,B3)$ for pure antimony (given in figures (4.12) and (4.14).

To obtain solutions for the model parameters, special minimization programs have been used to fit the theory to each of the measured curves of $\rho_{ij}(B)$ when the magnetic field is expressed as

$$B = B_o\ (\cos\phi, \sin\phi) \tag{5.3}$$

Then the angular-dependence form of the theory can be related to the experimental data. The computations made for each curve have been based on a collective set of data points taken at 5^o intervals, when the symmetry is included; this provides an over-determined set of thirty-six data points for each component $\rho_{ij}(\phi)$ from which a set of ten unknowns is to be determined.

The complete minimization program consists of thirty two subroutines collectively called MINUIT as shown in the flow diagram figure (5.1). MINUIT is a system of programs which solve the problems outlined above. As MINUIT is in principle designed to handle any function $F(x_i)$ where x_i are the unknown parameters, it is quite general, and may suit the needs of quite different users. A user, however, who spends much time minimizing a restricted class of function may well be able to write faster minimizing routines by making use of known properties of this function. For such users MINUIT may still offer a suitable organizational framework in which to embed his own routines as subroutines.

To the standard user MINUIT offers the possibility within one program of catering for different kinds of function, since it incorporates three different minimization methods, each of which may be used alone or in combination with the others, depending on the behaviour of the function and the requirements of the user. The three minimizing subroutines SEEK, SIMPLX, and MIGRAD, may be briefly described as follows:

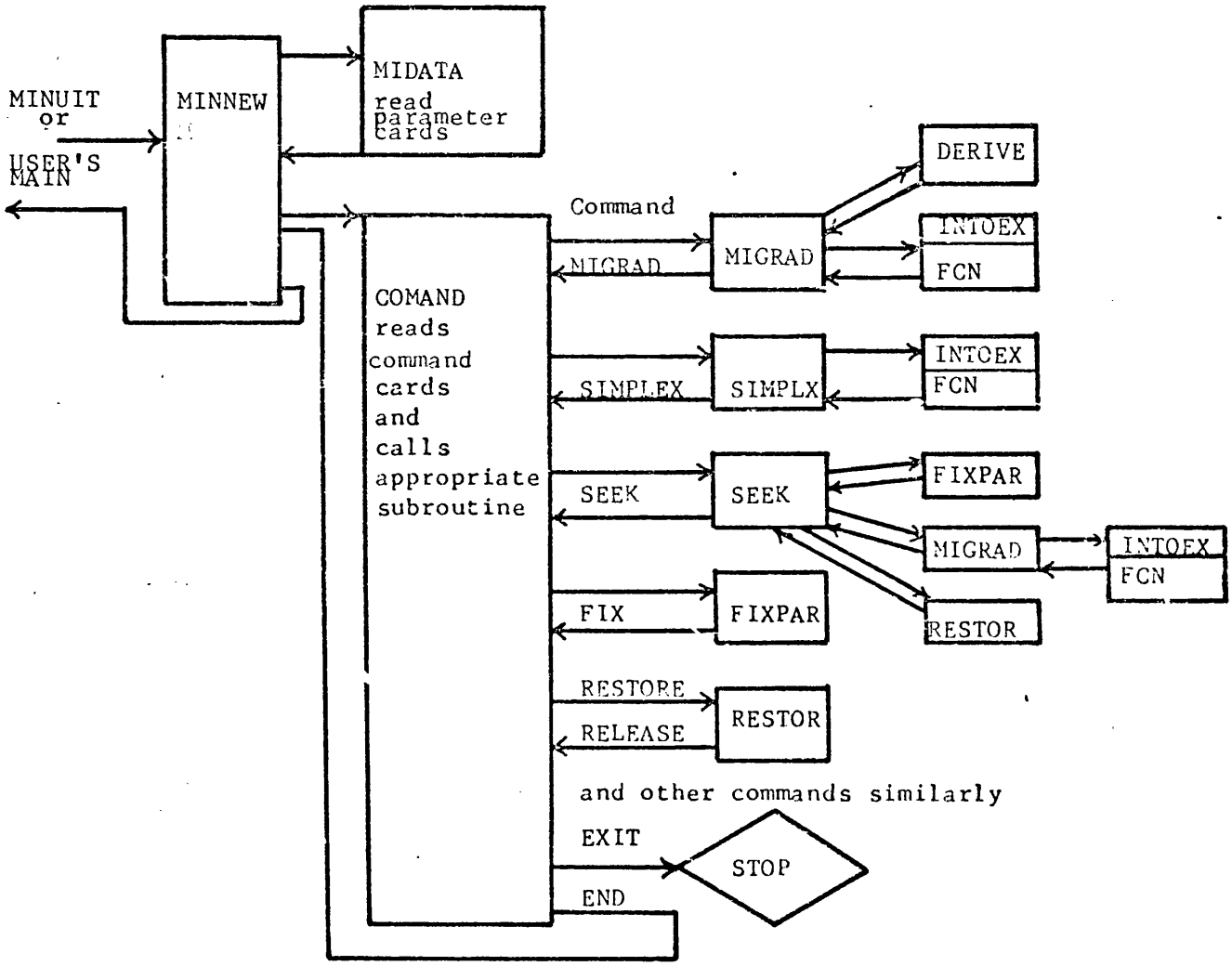

Fig.(5.1) Flow diagram for the MINUIT

1 SEEK :

is a Monte Carlo searching subroutine. It may be used at the beginning of a search for a fit when no reasonable starting point is known, or when it is suspected that there are several minima; however, it must not be expected to converge in the first trial.

2 SIMPLX :

is a minimization subroutine using a simplx method developed by Nelder and Mead (1965). It is very safe and reasonably fast when far from the minimum, and may also be used to converge to the exact minimum. It does not compute the covariance matrices, but gives order of magnitude estimates of their diagonal elements (the parametererrors).

3 MIGRAD :

is a minimization subroutine based on a variable matrix method by Fletcher (1970). It is extremely fast near a minimum or nearly quadratic region, but slower if the function is badly behaved. It uses the first derivatives of the functions, which may either be supplied by the user or estimated by MINUIT.

Some global logic is built into the program, for example, if MIGRAD fails, it automatically causes SIMPLX to be called to make another attempt. In addition, the minimization can be guided or separated into steps by use of the command subroutines FIX, RELEASE, and RESTORE (for more detail of these subroutines and a copy of the MINUIT program see the sub report), which causes a variable parameter to be fixed at a constant value or restored to

a variable status in between minimization steps. The program can also be instructed to force the value of any variable parameters to stay within limits during the minimizations.

User subroutine

The principle subroutine which must be supplied by the user is FCN (for a copy of the sub routine see appendix V) since, it is in FCN that the function to be minimized (F) must be calculated. Subroutine FCN calculates the value of the function to be minimized or studied.

The solution obtained for the computed model parameters is given in table (5.1) for pure antimony. The model parameters at different temperatures show a satisfying self-consistency which attests to the choice of a reasonable model.

This minimization has been used to obtain best fit solutions for the model parameters from the data given in figures (4.12) - (4.14) for $\rho_{11}(B1,B2,0)$ $\rho_{11}(B1,0,B3)$ and $\rho_{21}(B1,0,B3)$ for pure antimony, taken altogether at a given temperature, the solutions obtained at 77K, 196K, and 300K are given in table (5.1). There is good agreement between the model parameters obtained from the present work and those obtained by Öktü and Saunders (1967) using the low field method (see table (5.2)).

The same procedure has been adopted to calculate the mobility parameters for antimony-tin and antimony-germanium alloy single crystals and the solutions obtained are listed in tables (5.3) - (5.6).

The polar plots have been measured and therefore the complete set of model parameters obtained - on one sample from each composition. This method provides great advantages especially for alloys (as only one sample is necessary). This confirms that the expression for $\sigma_{ij}(B)$ used by Akgöz and Saunders (1974) for arsenic-antimony alloys applies directly to the other semimetals and their alloys.

TABLE (5.1)

Model parameters for pure antimony computed from the angular dependence at $B = |B| = 1.33$ Tesla

TEMP. (K)	Carrier density		Electrons				Holes			
	N	P	μ_1	μ_2	μ_3	θ_μ	ν_1	ν_2	ν_3	θ_ν
77	3.9	3.9	2.1	0.01	1.33	-9°	2.58	~0.0	2.4	-26°
196	4.2	4.2	0.5	0.005	0.389	-9°	0.79	~0.0	0.72	-28°
300	4.5	4.5	0.26	~0.0	0.205	-9°	0.41	~0.0	0.35	-27°

units: $N, P \times 10^{25} m^{-3}$, $\mu_i, \nu_i \; m^2 V^{-1} s^{-1}$

TABLE (5.2)

Model parameters for pure antimony computed from the low field method (Öktü and Saunders 1967)

TEMP. (K)	Carrier density		Electrons				Holes			
	N	P	μ_1	μ_2	μ_3	θ_μ	ν_1	ν_2	ν_3	θ_ν
77	3.86	3.86	1.62	0.038	1.26	-5^o	2.36	0.17	2.14	-24^o
183	4.0	4.0	0.459	0.01	0.38	-6^o	0.72	0.026	0.583	-24^o
273	4.22	4.22	0.274	0.011	0.195	-3^o	0.363	0.018	0.322	-24^o

units: $N, P \times 10^{25} m^{-3}$, μ_i, ν_i $m^2 V^{-1} s^{-1}$

TABLE (5.3)

Model parameters for antimony-tin alloy (Sb + 0.5at % sn) computed from the angular dependence at $B = |\mathbf{B}| = 2.19$ Tesla for 300K and $B = |\mathbf{B}| = 1.33$ Tesla for 77,196K.

TEMP. (K)	Carrier density		Electrons				Holes			
	N	P	μ_1	μ_2	μ_3	θ_μ	ν_1	ν_2	ν_3	θ_ν
77	0.14	13.5	1.220	0.0	0.72	-9°	0.88	0.0	0.84	-22°
196	0.14	14.1	0.22	0.0	0.20	-8°	0.32	0.0	0.30	-25°
300	0.15	14.2	0.10	0.0	0.09	-11°	0.20	0.0	0.17	-24°

units: N, P, $\times 10^{25} m^{-3}$, μ_i, ν_i $m^2 V^{-1} S^{-1}$

TABLE (5.4)

Model parameters for antimony-tin alloy (Sb+0.75 at% sn) computed from the angular dependence at $B = |\mathbf{B}| = 2.19$ Tesla for 196K and 300K, and $|\mathbf{B}| = 1.33$ for 77K.

TEMP (K)	Carrier density		Electrons				Holes			
	N	P	μ_1	μ_2	μ_3	θ_μ	ν_1	ν_2	ν_3	θ_ν
77	0.02	21.5	0.603	0.0	0.503	-4°	0.572	0.0	0.306	-26°
196	0.04	21.9	0.13	0.0	0.12	-9°	0.40	0.0	0.20	-31°
300	0.03	21.8	0.08	0.0	0.07	-4°	0.32	0.0	0.17	-25°

units: $N, P \times 10^{25} m^{-3}$, μ_i, ν_i $m^2 V^{-1} S^{-1}$

TABLE (5.5)

Model parameters for antimony-tin alloy (Sb+1 at % Sn) computed from the angular dependence at $B = |B| = 2.19$ Tesla for 300K and $B = |B| = 1.33$ Tesla for 77K and 196K.

TEMP (K)	Carrier density	Holes			
	P	ν_1	ν_2	ν_3	θ_ν
77	36.0	0.48	~0.0	0.25	-26°
196	36.0	0.40	~0.0	0.17	-24°
300	36.0	0.36	~0.0	0.16	-24°

units: $P \times 10^{25}\ m^{-3}$, ν_i, $m^2\ V^{-1} S^{-1}$

TABLE (5.6)

Model parameters for antimony-germanium alloy (Sb+1.16 at % Ge) computed from the angular dependence at $B = |B| = 2.19$ Tesla for 300K and $B = |B| = 1.33$ Tesla for 77K and 196K

TEMP (K)	Carrier density	Holes			
	P	ν_1	ν_2	ν_3	θ_ν
77	39.0	0.528	~0.0	0.301	-20^o
196	39.0	0.453	~0.0	0.28	-22^o
300	39.0	0.40	~0.0	0.27	-23^o

units: $P \times 10^{25}\ m^{-3}$, ν_i, $m^2\ V^{-1}S^{-1}$

CHAPTER SIX

DISCUSSION

6.1 Introduction

Two distinct approaches for the measurement of the magnetoresistivity tensor components $\rho_{ij}(B)$ are available, these are:

1. by obtaining the low field tensor components;
2. by measurement of either the angular or the field dependence of the field dependent tensor components.

Previously, the field dependent tensor method has been shown to give the same band model parameters and mobilities for bismuth (Saunders and Sümengen 1972) and arsenic-antimony alloys (Akgöz and Saunders 1974). A further check on the validity of the field dependent tensor method has been made here on antimony itself. The results in table (5.1) present, for the first time, details of carrier densities, mobilities and the tilt angles of the Fermi surface pockets for antimony obtained by using field dependent tensor. A comparison of the model parameters of antimony found here with those calculated from the low field method by Öktü and Saunders (1967) as shown in table (5.2) shows that there is good agreement between these results obtained using both methods. This establishes further the validity of the field dependent tensor method, and in particular shows that it holds for antimony itself. Since the results have been obtained from the field dependent and orientation dependence of the magnetoresistivity tensor components, they provide for the first time a quantitative explanation of the shape and field dependence of the tensor components of antimony (figures (4.12) to (4.14)). Furthermore, the carrier signs can be redetermined, in itself, useful to do in view of the long standing argument about which carrier occupied which set of pockets in antimony.

In view of the good agreement between band model parameters obtained from the low field method and field dependent tensor method results for antimony itself, we can use with confidence the field dependent tensor method to analyse quantitatively the alloy results. The advantages of the field dependent tensor are that the results provide a much more accurate set of model parameters for the alloys than could be obtained from the low field method by Öktü and Saunders (1967), and gives the complete set of model parameters on one specimen alone; this is important, especially for alloys, these are always difficult to grow homogeneously and for which the doping level can vary from specimen to specimen.

It is found that the best fit for the experimental values is made by assuming a two band model with tilted Fermi surfaces for the compositions 0.5 at % and 0.75 at % tin, while for the 1.0 at % tin and 1.16 at % germanium, the best fit for the experimental data is found by assuming of a one band carrier (valence band) model, we will discuss this particular point later in this chapter. Saunders and Öktü (1968) found there to be an extra set of holes in their antimony-tin alloy (1.7 at % to 8 at % tin), but in our case there was no evidence of any such holes, presumably because the concentration of our alloys were considerably smaller than those in which a second set of holes had been previously observed.

6.2 Electrical resistivity and Matthiessen's rule in the alloys.

In dilute alloys the residual resistivity is expected to vary linearly with concentration. This reflects the fact that scattering from each impurity atom should be independent of the other atoms so that the total scattering is just proportional to the number of scatterers i.e. to the concentration. This proportionality is illustrated in figure (6.9), and can be explained by *Matthiessen's rule* which will be studied later on. In addition to scattering by chemical impurities residual scattering can arise from physical defects in the lattice - such as vacancies, dislocations, stacking faults and so on. But in the present instance the doping level is so great that the effects of then other scattering centres are negligible compared with the ionized impurity scattering. This will be discussed in section 6.5.

The temperature dependences of the zero-field resistivity $\rho_{11}(B=0)$ for antimony-tin and antimony-germanium alloys are compared in figures (4.10) and (4.11) with those of arsenic-antimony alloys measured by Akgöz and Saunders (1974). The positive temperature coefficient of $\rho_{11}(B=0)$ over the whole temperature range shows that antimony-tin and antimony-germanium alloys have metallic behaviour, as do the arsenic-antimony alloys. However, as we will see in section 6.5, the scattering due to a tin or germanium impurity in antimony arises from the differences in the potential of the impurity from that of the host ion together with any screening effects due to the conductions. In the arsenic-antimony alloy (Akgöz and Saunders 1974) this is not so because arsenic and antimony have the same valency and scattering must arise from the disordered atomic array of lattice sites occupied at random by the two different atom types which scatter more efficiently than the lattice vibrations or carrier-carrier interactions.

Separation of the resistivity into two independent components (ρ_o and ρ_i) can be seen to be justified by examination of the experimental data in figures (4.10) and (4.11)

Matthiessen's rule

In general, it is found experimentally that if a dilute alloy has a residual resistivity ρ_o (measure at temperature low enough for phonon scattering to be negligible) its resistivity $\rho_{alloy}(T)$, at the same temperature T is to a good approximation, given by

$$\rho_{alloy}(T) = \rho_o + \rho_{pure}(T) \tag{6.1}$$

where $\rho_{pure}(T)$ is the resistivity of the pure host material (antimony in our case) at that temperature. This is known as *Matthiessen's rule*. This relationship implies that the temperature independent resistivity contributed by impurities (ρ_o) is effectively in series with the temperature-dependent part ($\rho(T)$), contributed by the phonons. Its theoretical basis is straightforward. Suppose that the scattering of electrons by impurities can be described by a relaxation time τ_o. Then at low temperature, when the impurities alone are responsible for the scattering, the conductivity is given by

$$\sigma_o = \frac{1}{\rho_o} = \frac{ne^2\tau}{m} \tag{6.2}$$

where n is the number of electrons per unit volume and m and e are their mass and charge. If at high temperature T the relaxation time for the pure metal due to phonon scattering is $\tau_{ph.}$, then for the pure metal

$$\frac{1}{\rho(T)} = \sigma_{pure}(T) = \frac{ne^2\tau_{ph.}}{m}. \tag{6.3}$$

Now consider the alloy at temperature T when both impurity scattering and phonon scattering operate together ($T \geq 25^{o}K$). The relaxation time τ for both processes is given by:

$$\frac{1}{\tau} = \frac{1}{\tau_o} + \frac{1}{\tau_{ph.}} \tag{6.4}$$

This holds if the two scattering mechanisms operate independently; since the probability of scattering is inversely proportional to the corresponding relaxation time, this expression is equivalent to adding the probability of scattering by two separate mechanisms. The resistivity of the alloy $\rho_{alloy}(T)$ at temperature T is related to τ by the expression

$$\frac{1}{\rho_{alloy}} = \sigma_{alloy}(T) = \frac{ne^2\tau}{m} \tag{6.5}$$

If therefore we combine equations 6.2., 6.3., 6.4. and 6.5., we get

$$\frac{1}{\sigma_{alloy}(T)} = \frac{1}{\sigma_o} + \frac{1}{\sigma_{pure}(T)}$$

or

$$\rho_{alloy}(T) = \rho_o + \rho_{pure}(T) \tag{6.6}$$

which is *Matthiessen's rule* expressed in an analytic manner. The rule is only valid for dilute alloys. That is to say, alloys in which the concentration of defects is not so great as to modify the lattice constant, elastic properties, and Fermi energy of the element. It is difficult to give a precise figure for the concentration of defects at which these changes occur, since it will vary from element to element, but it is probably true to say that the rule is no longer true for concentrations of defects of over 10 per cent. However, our most

concentrated sample does not exceed 3 per cent, then the *Matthiessen's rule* can be assumed for our samples. We should also emphasize that although we have here quoted the example of impurity and Phonon scattering, the analogue of *Matthiessen's rule* can be applied to other combinations of scattering mechanisms, e.g. electron-electron and phonon scattering, electron-electron and impurity scattering; or all three together; or from two different kinds of impurity.

We now turn to discuss the physical significance of the band model parameters and mobilities obtained from the computations described in chapter five. The carrier mobilities will be discussed first.

6.3 Carrier Mobilities

I - Pure antimony

The temperature dependence of the principle electron mobilities μ_1 and μ_3 are plotted on a logarithmic scale in figure (6.1). Both μ_1 and μ_3 show the same temperature dependence, as expected from the uniform relaxation time assumption. Similarly, the hole mobilities are illustrated in figure (6.2). Both sets of carriers have almost identical temperature dependences of mobility $T^{-1.4}$ for electrons and $T^{-1.52}$ for holes which are in very good agreement with those obtained by the low field method (Öktü and Saunders 1967) $T^{-1.42}$ and $T^{-1.48}$ respectively. The electron and hole mobilities calculated from the present work are higher in magnitude than those obtained by Öktü and Saunders (1967), which can be explained by the better quality of the crystals grown using the zone levelling technique.

Clearly, the formula $\tau \alpha T^{-1}\varepsilon^{-\frac{1}{2}}$ for scattering in semimetals is insufficient. This is not surprising considering the simple model of the energy bands that is used to derive the formula. The present finding of $T^{-1.4}$ and $T^{-1.52}$ laws for scattering of electrons and holes respectively gives evidence of a similar scattering mechanism for both types of carriers. The exponent may be compared with that of -2.1 for bismuth (Michenaud and Issi 1972) and -1.2 for single crystal graphite (Soule 1958). In a semiconductor, the mean energy of the non-degenerate carrier is proportional to $T^{-\frac{1}{2}}$ and hence, for acoustic mode lattice scattering the relaxation time and carrier mobilities obeys a $T^{-1.5}$ law. In metals and semimetals, where degenerate statistics are applicable only, carriers on the Fermi surface need to be considered. The Fermi level in semimetals has only a weak temperature dependence and is constant in metals. The Seebeck coefficient data of

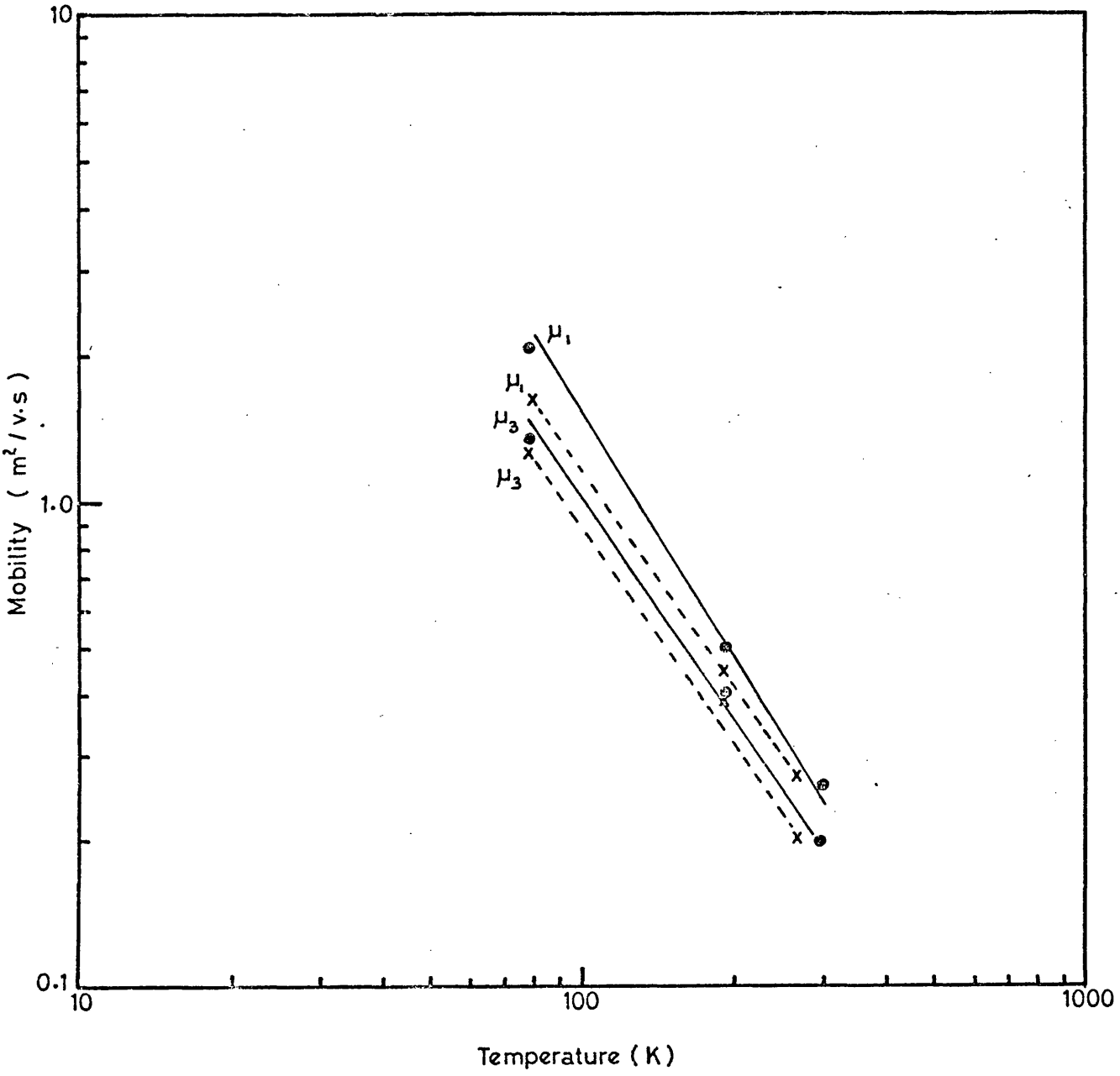

Fig. (6.1) The temperature dependence of the electron mobility tensor components for pure antimony.

Broken line: Öktü and Saunders (1967)

Solid line: Present work

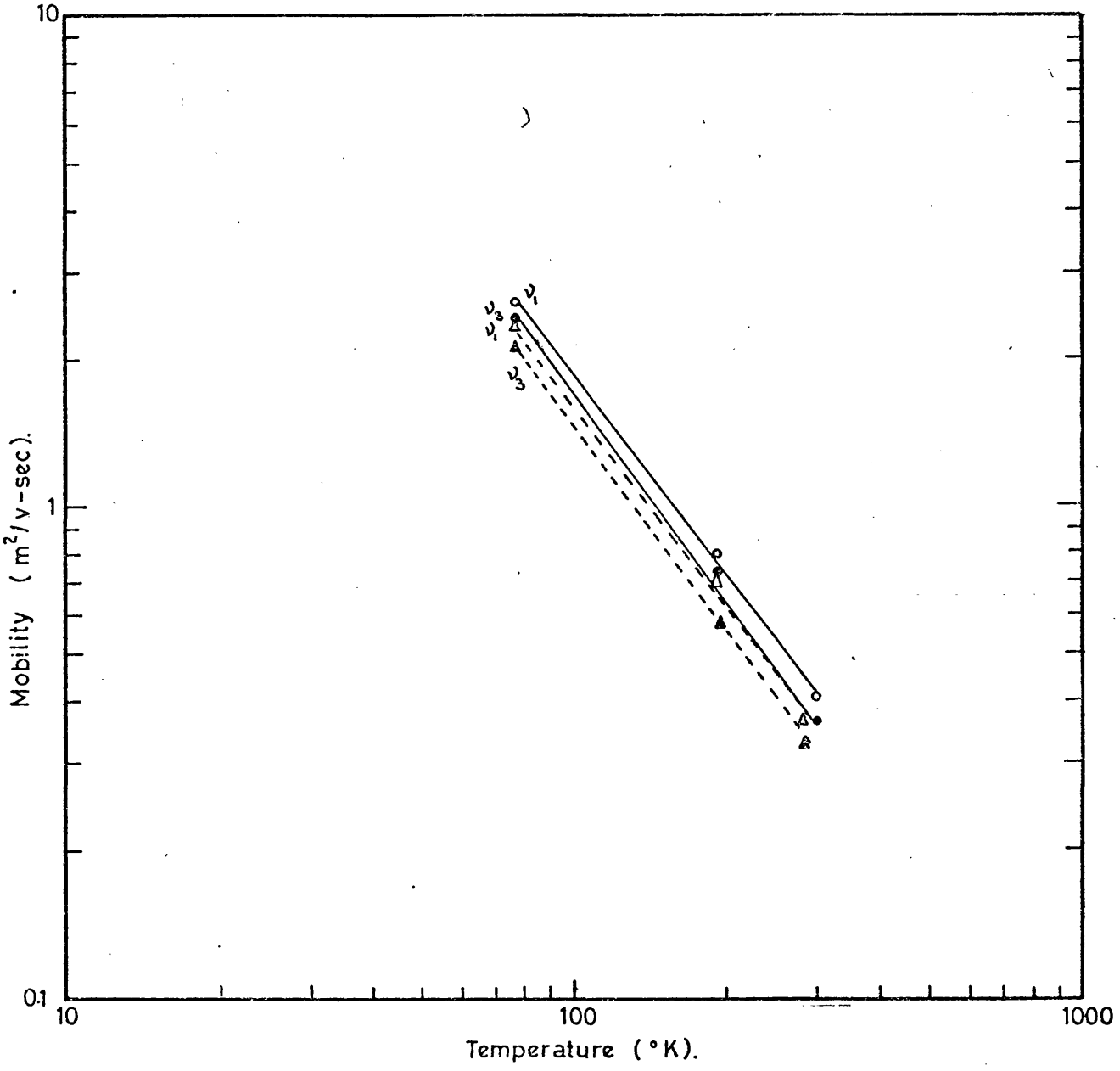

Fig. 6.2 The temperature dependence of the hole mobility tensor components for pure Antimony.

Broken line: Öktü & Saunders

Solid line: present work

antimony by Saunders and Öktü (1968) shows that the Fermi energies of electrons and holes are constant between 77K and 300K. Thus for acoustic mode intervalley scattering, a mobility temperature dependence closer to $T^{-1.0}$ between $77^{o}K$ and $300^{o}K$ would be expected. The $T^{-1.5}$ dependence of mobilities does not appear to have a simple explanation. Further theoretical studies are required to clarify the situation and assess possible contribution from other mechanisms such as intervalley scattering and electron-hole collisions. Plausibly the requirement of an isotropic relaxation time may be relaxed somewhat and the relaxation time written as a tensor $\boldsymbol{\tau}$, each component being a separate function of energy (Herring and Vogt 1956) therefore,

$$\mu = \frac{e\boldsymbol{\tau}}{m^*} \qquad (6.7)$$

When $\boldsymbol{\tau}$ is not too anisotropic, this approach is a good approximation; certainly it follows when the magnitudes of the tensor components differ by as much as a factor 2.

To estimate the relaxation time from equation (6.7) the appropriate components of the effective mass tensor are needed. Datars and Vanderkooy (1964) had provided these, although at the time when they made their cyclotron resonance experiments, the carrier types were inverted. That particular problem has been discussed in chapter two: carrier types which they called electrons were holes and vice-versa. In fact the present results add further confirmation that this is so; therefore in our estimation of the relaxation time, the effective mass data of Datars and Vanderkooy (1964) has been used but the carrier types have been changed round, thus the effective mass stated by Datars and Vanderkooy (1964) to be that of holes is taken to be that of electrons and vice-versa. In table (6.1) the relaxation times estimated from the present work are compared with those previously

Table (6.1) Relaxation times for electrons and holes in antimony calculated from the cyclotron effective masses (Datars and Vanderkooy 1964) and mobility data from band model parameters

Relaxation times	77K		196K		300K	
Electrons	Present work	Öktü & Saunders *	Present work	Öktü & Saunders *	Present work	Öktü & Saunders *
τ_1	11.1	8.6	2.6	2.4	1.3	1.4
τ_2	0.6	2.5	0.3	0.7	v.small	
τ_3	6.7	6.3	2.0	1.9	1.0	1.0
Holes						
τ_1	10.0	9.1	3.1	2.7	1.6	1.4
τ_2	v.small		v.small		v.small	
τ_3	6.8	6.1	2.1	1.6	1.0	0.9

* mobility obtained from low field tensors.
Relaxation times are quoted in units of 10^{-13} sec.

obtained by Öktü and Saunders (1967). The agreement is reasonable; however, the relaxation times obtained here are somewhat larger especially at 77°K than those obtained by Öktü and Saunders (1967). This is naturally a consequence of the larger value of the carrier mobilities obtained from the present work. These relaxation times are not highly anisotropic, and the anisotropy ratio is well within the limit of 2 for which the collision integral can be approximated by a tensor relaxation time (Herring and Vogt 1956).

It is interesting to note that the relaxation times in antimony are an order of magnitude larger than those in metals at the same temperature (i.e. for copper at 0°C, $\tau = 3 \times 10^{-14}$ sec. Mott and Jones 1936, page 286). This phenomenon is well known in semimetals. The reason for it is as follows: assuming one closed surface - or, if there are several, intravalley scattering - the largest wave number involved in scattering as far as electrical conduction concerned is that of a phonon that takes a carrier from one side of the Fermi surface to the other: i.e. $q \leq 2 \mid K_F \mid$ (where $K_F \simeq 0.6 \times 10^{9}\ m^{-1}$ in Sb). When the number of conduction electrons per atom (N_a) less than 0.25 ($N_a \sim 4 \times 10^{-3}$ in Sb), $2 \mid K_F \mid$ is small (Sondheimer 1952, Tsai *et al* 1978), and scattering is restricted to long wave length (small wave number) phonons. Furthermore, the relaxation times depend upon the factor $(4N_a)^{-4/3}$ and should decrease with increasing carrier concentration; this follows qualitatively through the sequence of semimetals at 77°K, for example

bismuth $N = 4.6 \times 10^{17} cm^{-3}$, $\tau_{av} \sim 10^{-11}$ sec. (Sümengen and Saunders 1972)

antimony $N = 3.9 \times 10^{19} cm^{-3}$, $\tau_{av} \sim 8 \times 10^{-13}$ sec. (present work)

and arsenic $N = 2.1 \times 10^{20} cm^{-3}$, $\tau_{av} \sim 3 \times 10^{-13}$ sec. (Jeavons and Saunders 1969)

The long relaxation time coupled with the small carrier effective masses accounts for the comparatively high mobilities found for semimetals.

II - Antimony-tin alloys

The behaviour of the carrier mobilities in the antimony-tin alloys is quite different from those in pure antimony itself. The tables (5.3) to (5.5) show the model parameter solutions for the antimony-tin alloys. Both electron and hole mobilities are decreased by increasing the tin concentration, as might be expected from the enhancement of impurity scattering (section 6.5).

Since in the pure antimony and its dilute alloys the electron and hole ellipsoids are highly elongated, the components of electron and hole mobilities reflect this. In antimony and its dilute alloys μ_2 and ν_2 are at least an order of magnitude smaller than either μ_1 or μ_3 and ν_1 or ν_3 respectively, μ_2 and ν_2 are effectively zero because the effects of the other components of the tensor swamp them, and quantitative information about their temperature dependence and the effect of scattering on them cannot be obtained, see Öktü and Saunders (1967).

The temperature dependence of the hole mobilities ν_1 and ν_3 are plotted on logarithmic scales in figures (6.5), (6.7) and (6.8); for each composition ν_1 and ν_3 both show almost the same temperature dependence: the same behaviour as found in the case of the pure element. The temperature dependence of the carrier mobilities decreases with substitution of more tin, being $T^{-0.8}$, $T^{-0.5}$ and $T^{-0.3}$ for 0.5 at %, 0.75 at % and 1.0 at % tin respectively.

The figures (6.4) and (6.6) show the temperature dependence of electron mobilities (μ_1 and μ_3) for 0.5 at % and 0.75 at % tin. Both mobility tensor component for samples of these compositions show a $T^{-1.6}$ dependence, that is almost the same temperature dependence a s found in pure antimony itself. Since the carrier

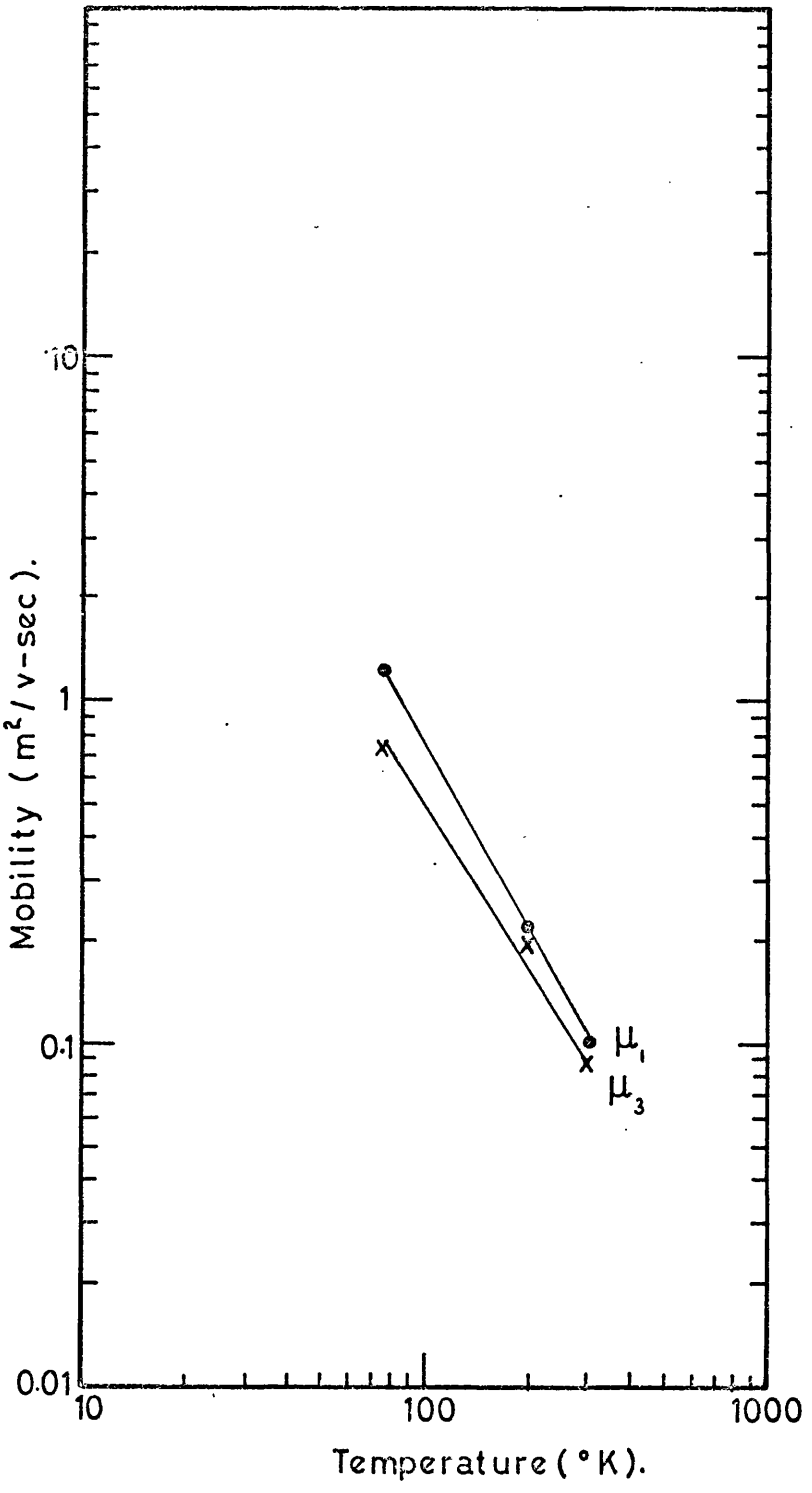

Fig. 6.4 The temperature dependence of the electron mobility tensor components of (Sb 0.5 at % Sn) alloy.

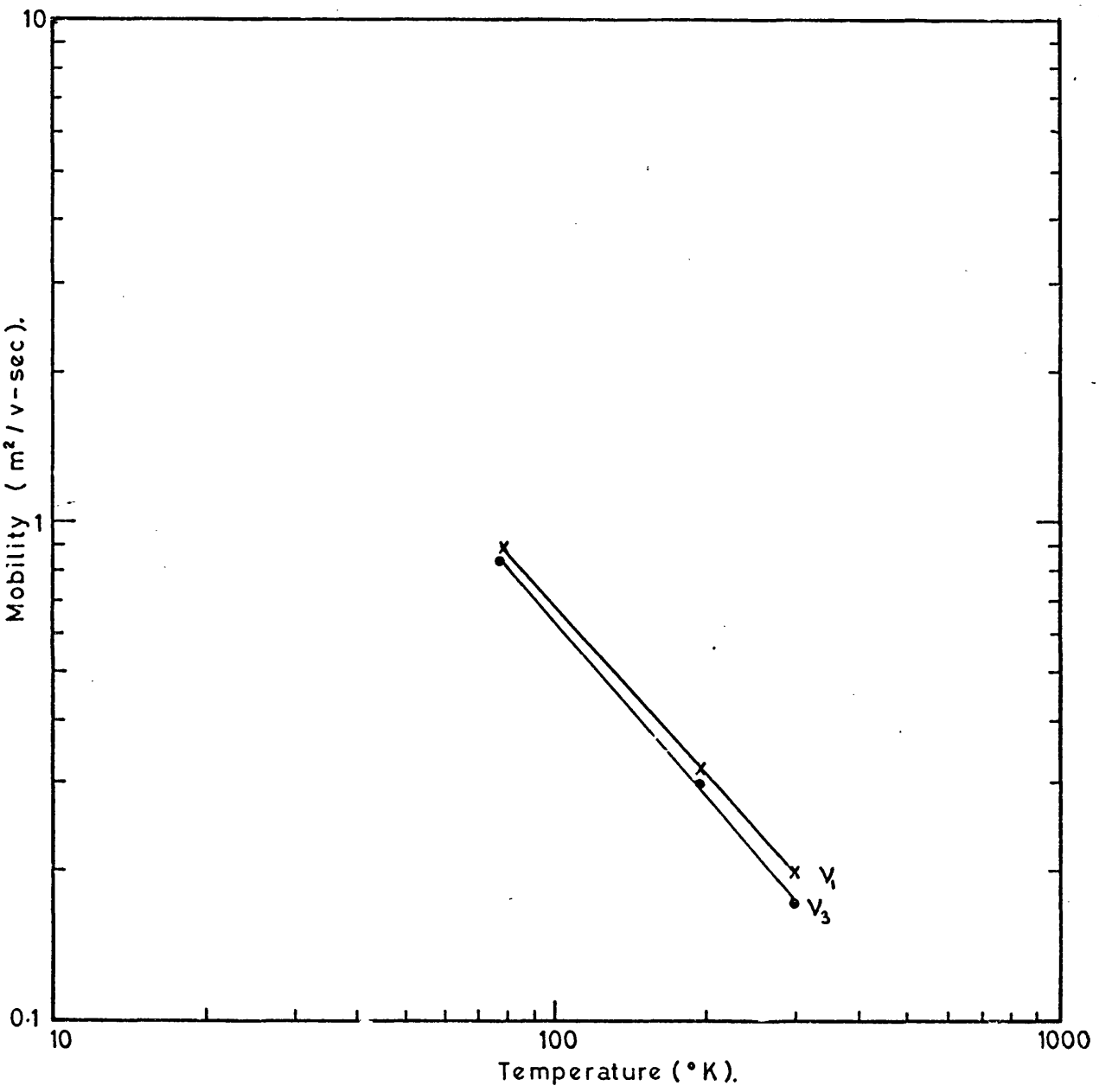

Fig. 6.5 The temperature dependence of the hole mobilitv tensor components of (Sb 0.5 at % Sn) alloy.

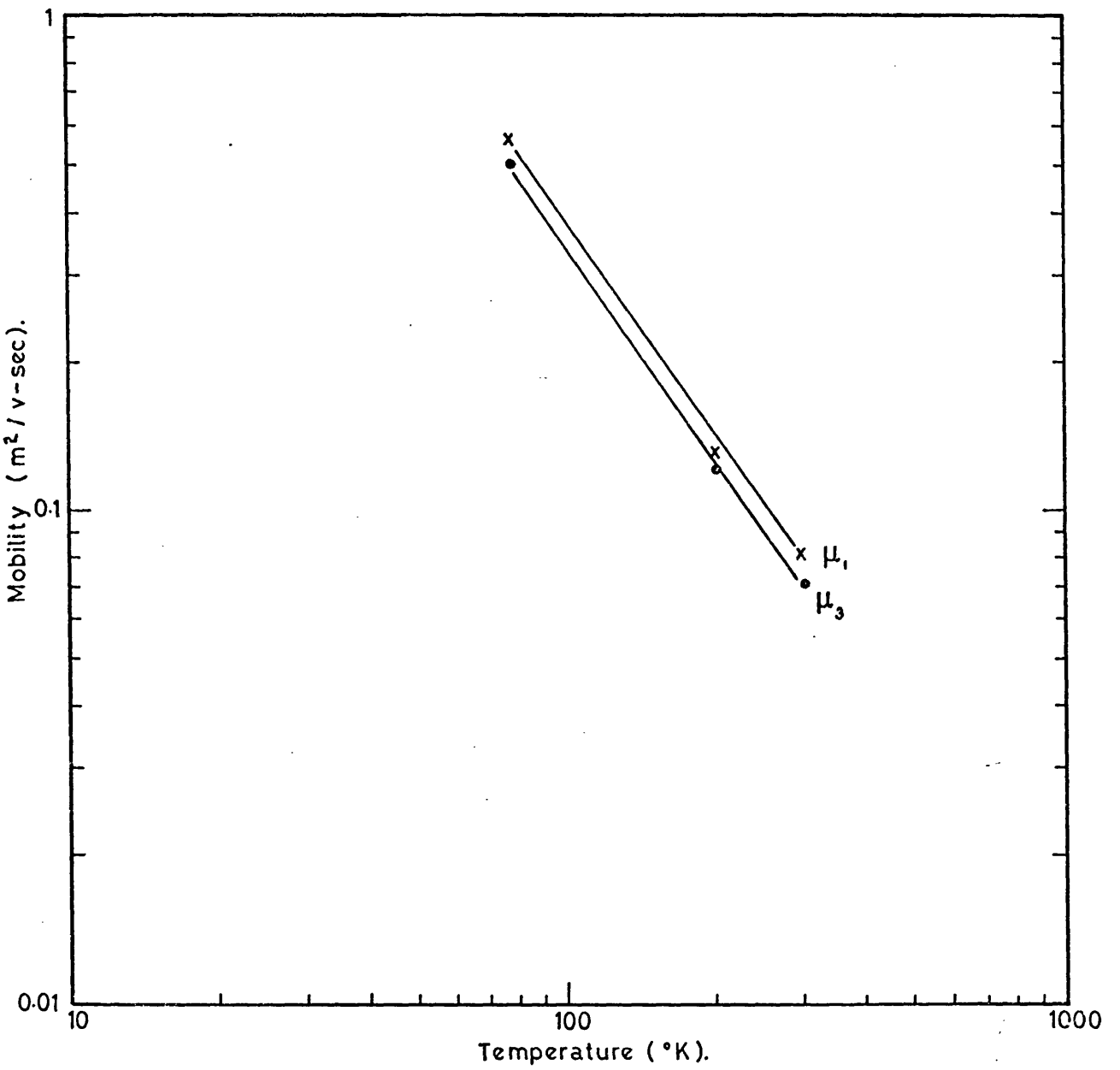

Fig. 6.6 The temperature dependence of the electron mobility tensor components of (Sb 0.75 at % Sn) alloy.

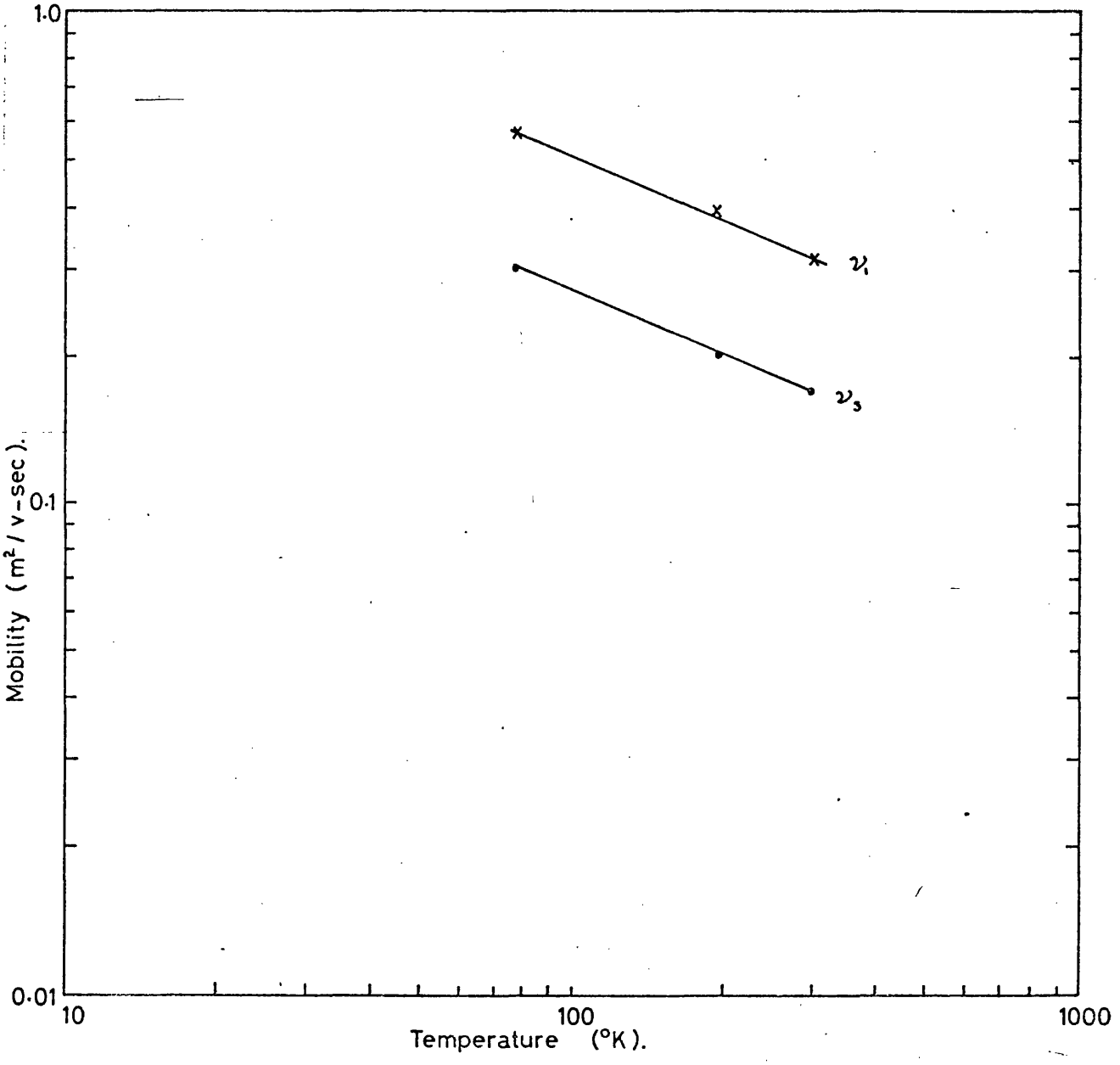

Fig.(6.7) The temperature dependence of the hole mobility tensor components of Sb-(0.75 at%Sn)alloy

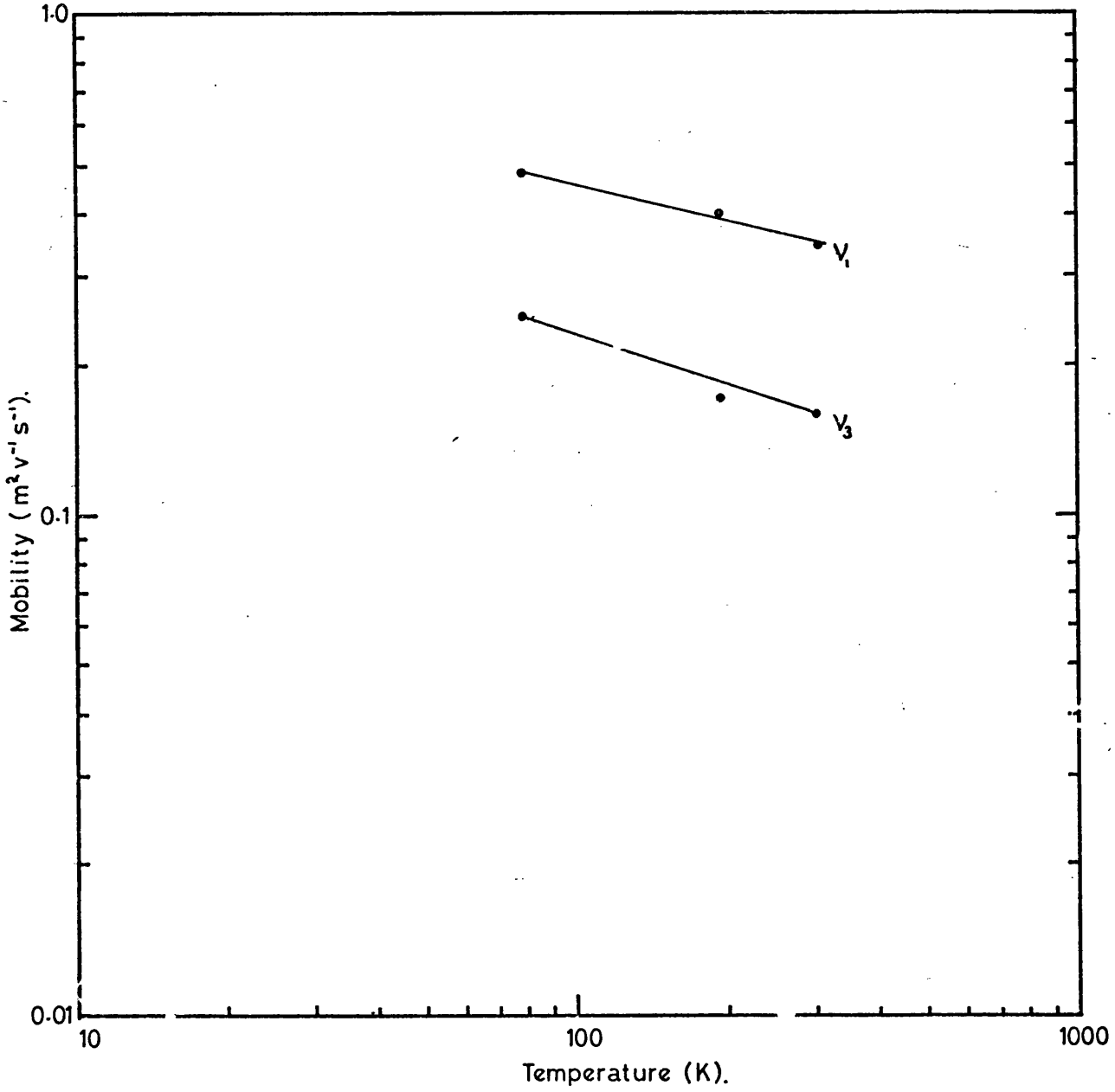

Fig. 6.8 The temperature dependence of the hole mobility tensor components of (Sb 1 at % Sn) alloy.

densities of the electrons in the doped alloys are much less than those of the holes, their contribution to the tensor components is small compared with that of holes; therefore, the band model and mobility parameters calculated for electrons are known to a much less precise degree than those of holes. Hence, the data for electrons must be treated with some caution; however, the results obtained do indicate that the $T^{-1.6}$ temperature dependence of electron mobility in tin-doped alloys are quite different from those of the holes, the effect of temperature on the electron mobility is much greater in tin-doped alloys than it is on the hole mobilities. One possible explanation of these differences in the temperature dependence of the mobilities is that there are different contributions from the several scattering mechanisms involved. Another possibility for these differences in the temperature dependence of the mobilities is that which could arise from the sensitivity of the Fermi level and thus the effective mass tensor components for a non-parabolic model.

In the alloys the ratio μ_1/μ_3 and ν_1/ν_3 of the mobility tensor components for electrons and holes respectively are somewhat different from those found for pure antimony. This change in mobility ratios is much more pronounced for the holes than it is for electrons. It is likely that the source of the change in mobility ratios on alloying is due to the change in the ratio of the effective masses (m^*_{1h}/m^*_{3h} and m^*_{1e}/m^*_{3e} for holes and electrons respectively) as the Fermi surface expands; for an isotropic relaxation time, the estimation of these ratios at room temperature are

$$1/\nu_1 : 1/\nu_3 \sim m^*_{1h} : m^*_{3h} \tag{6.8}$$

falls from 1 : 0.85 in the pure element,

through 1 : 0.55 in the 1.0 at % tin specimen

while the ratio of electron mobility tensor components

$$1/\mu_1 : 1/\mu_3 \sim m^*_{1e} : m^*_{3e} \qquad (6.9)$$

shows 1 : 0.8 in the pure antimony and 1 : 0.9 in the 0.75 at % tin specimen. This implies that there is not much change in the effective mass tensor of electrons by introducing more holes.

On alloying the hole Fermi surface volume has increased considerably. In fact in the 1.0 at % tin specimen the increase in the Fermi surface volume over that of pure itself is in the ratio of the carrier densities $\frac{36.0}{4.5} \sim 8$. The change in effective mass ratio given in equation (6.8) implies that as the Fermi surface volume expands the ellipsoids axes axial ratio do not do so in the same way, so that the overall shape of ellipsoid changes and therefore the effective mass ratio m^*_{1h}/m^*_{3h} also changes. It can be noted that similar behaviour for bismuth doped tin was found by Bate and Einspruch (1967).

Finally, we consider the minimum in the plot (6.9) of $\rho_{11}(B=0)$ against tin concentration at different temperatures. Since the majority carriers dominate the electrical resistivity, the source of this effect must lie with the changing balance of their densities and mobilities. That the minimum occurs only in $\rho_{11}(B=0)$, arises from the anisotropy of the electron to the hole mobility tensor ratio ($\mu_z/\nu_z \sim 0.55$ in pure antimony) parallel and ($\mu_x/\nu_x \sim 0.81$ in pure antimony) perpendicular to the trigonal axis (Saunders and Öktü 1968).

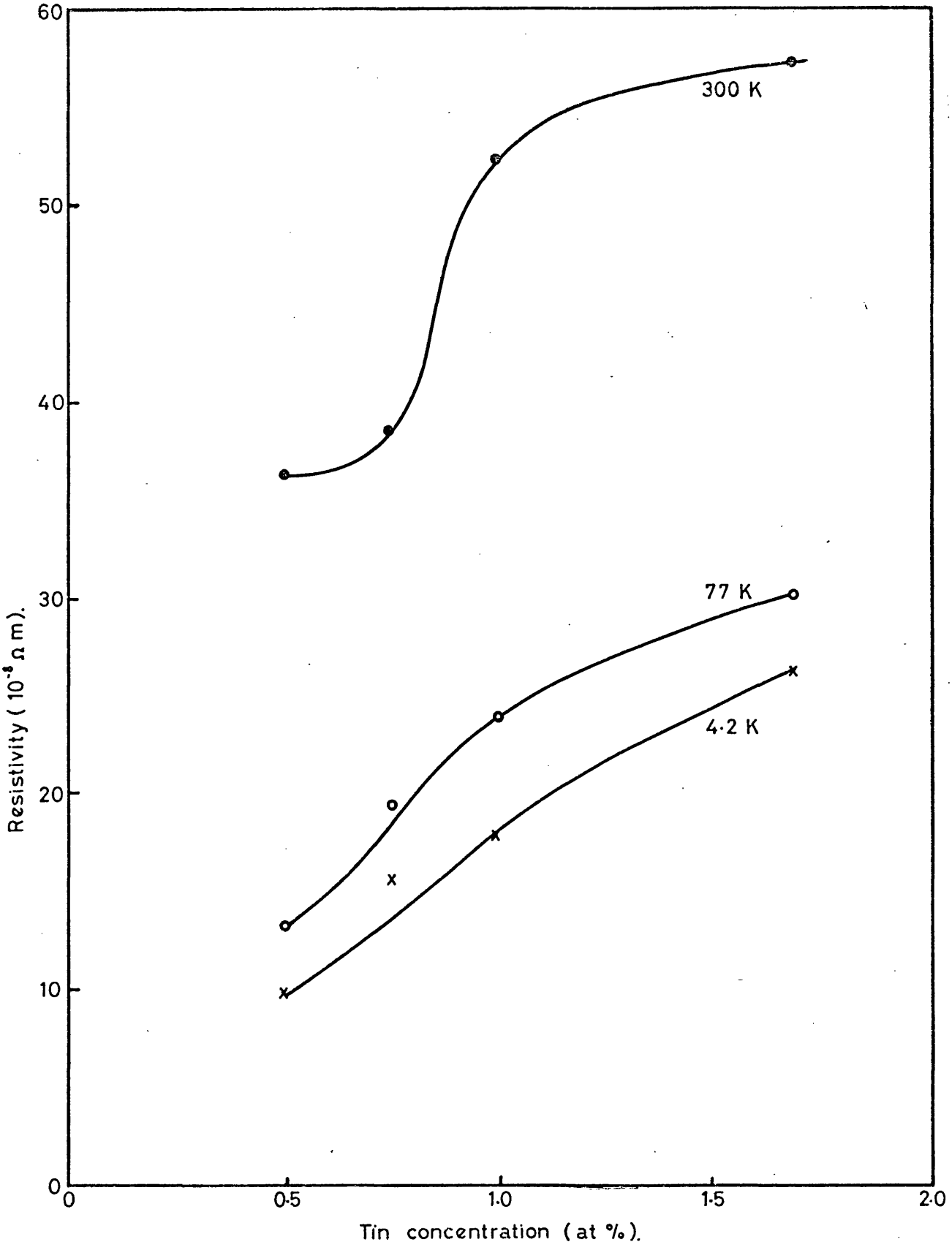

Fig. 6.9 The dependence of the component ρ_{11} of the resistivity tensor upon tin concentrations. Results for 1.7 at % tin are taken from Saunders and Oktü (1968).

III - Antimony-germanium alloy

For this particular alloy system we have chosen to measure the magnetoresistivity tensor component of only one composition (1.16 at % germanium). If germanium acts in the same way as tin, then this composition should be sufficient to lower the Fermi level below the bottom of conduction band edge, so that only holes are present. The other samples for which $\rho_{11}(B=0)$ has been measured, (figure 4.11) are more heavily doped with germanium, therefore, the tensor components are correspondingly less and are not measurable within a reasonable degree of accuracy. When we attempted to measure the magnetoresistivity tensor components, they were indeed found to be too small.

The mobility data has been obtained from two different antimony-germanium samples (*y*- and z-cut samples). Table (5.6) is the first set of band model parameters ever established for an antimony-germanium alloy. The mobilities are somewhat higher than those in the comparable antimony-tin alloy sample (1.0 at % tin) although the antimony-germanium crystals were not grown by the zone levelling technique. This implies that the mobilities in antimony-germanium alloys are less dependent on the dope densities than antimony-tin alloys. However, these differences are small: the mobility parameters for this antimony-germanium alloy are the same magnitude as the corresponding antimony-tin alloy.

The temperature dependence of the principle hole mobilities ν_1 and ν_3 are presented in figure (6.10), which shows a $T^{-0.2}$ and $T^{-0.08}$ dependence respectively. In antimony-germanium alloy, ν_1 and ν_3 do not show quite the same temperature shown in antimony-tin alloys. This possible discrepancy comes about because of the

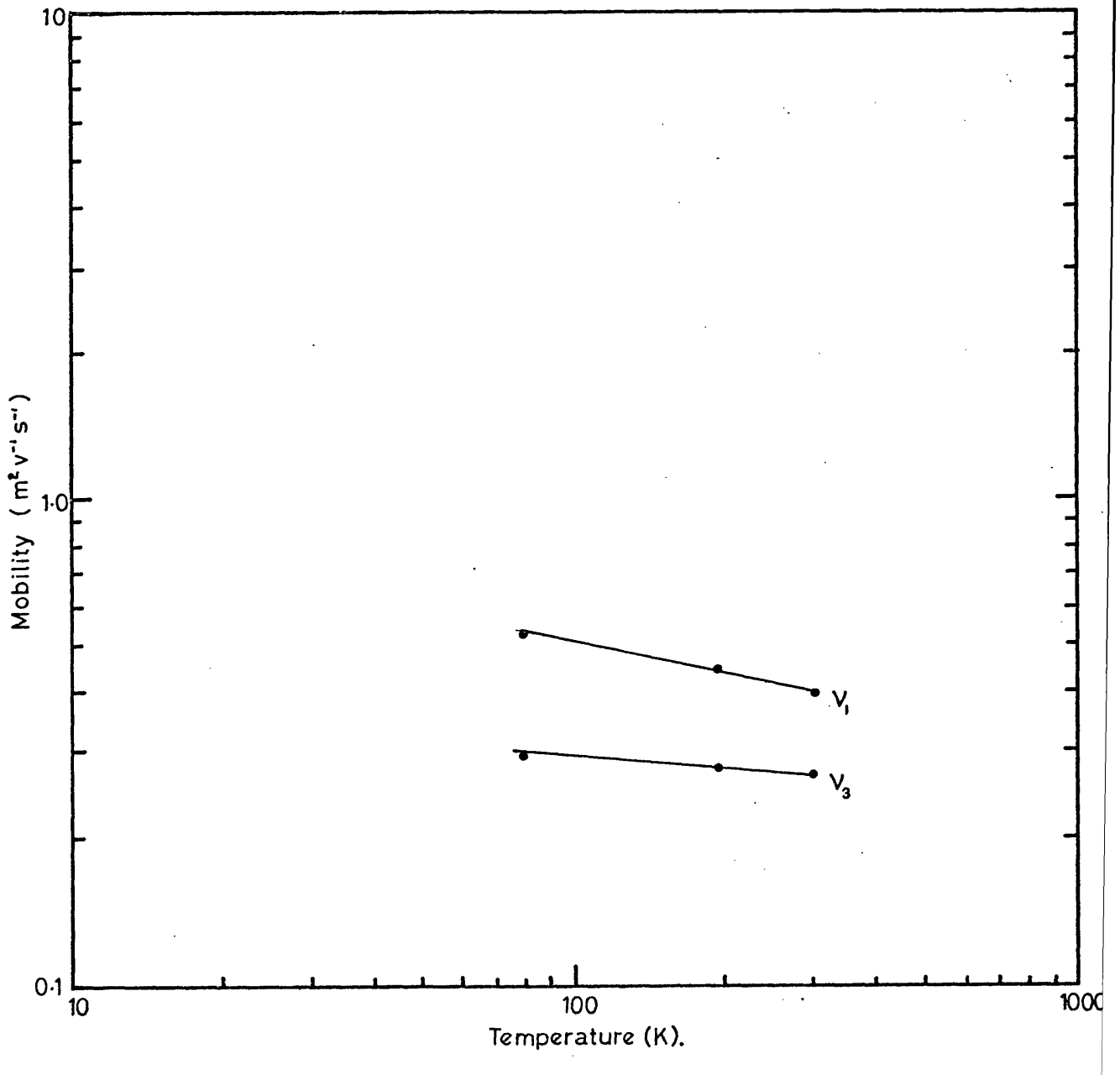

Fig. 6.10 The temperature dependence of the hole mobility tensor components of (Sb-1.16 at % Ge) alloy.

different growth technique used with the antimony-germanium alloy rather than the zone levelling technique. One of the mobility tensor components (ν_3) given very weak ($T^{-0.08}$) temperature dependence of mobility, possible because the particular antimony-germanium sample used to obtain these mobility parameters was (001) direction (z-cut). Antimony is one of the materials which cleaves easily in this direction (see chapter two); and when we tried to measure $\rho_{33}(B=0)$ as a function of temperature the sample cleaved at below $200^{o}K$. Therefore, the results obtained on this z-specimen must be treated with caution.

If we assume as in antimony-tin alloys, that the relaxation time is isotropic in the antimony-germnium alloys; then the effective mass anisotropy ratio will be the same as the mobility ratio ν_3/ν_1. The estimated effective mass ratio in antimony-germanium alloys at room temperature using the relation (6.8), drops from 1 : 0.85 in the pure element to 1 : 0.7 in the antimony-germanium alloy (1.16 at % Ge). This indicates that the change in the mass ratio is much less than in the comparable tin-doped alloy sample, although the expansion in the volume of the Fermi surface, estimated from the carrier density ratios 39.0/4.5~8.6 (see section 6.4), is almost the same as in tin-doped sample.

6.4 Carrier densities

The carrier densities for pure antimony calculated from the field dependent tensor data are $3.90 \times 10^{19}/cm^3$ at $77^{o}K$ and $4.5 \times 10^{19}/cm^3$ at $300^{o}K$. Between $77^{o}K$ and room temperature the Fermi energy of electrons (ε_F^e) is 0.098 ev and the Fermi energy of holes (ε_F^h) is 0.067 ev. The overlap energy, estimated as 0.165 ev, agrees with that obtained at liquid helium temperatures from the de Haas-Shubnikov effect (0.20 ev) by Rao *et al* (1964). The Fermi energies and the band overlap energy are essentially temperature independent up to $300^{o}K$.

The Fermi level in semimetals is characterised by the following equation (Saunders and Öktü 1968):

$$\left[\frac{m_h^*}{m_e^*}\right]^{3/2} = \frac{n_e}{n_h} \cdot \frac{F_{\frac{1}{2}}(\xi_e)}{F_{\frac{1}{2}}(\xi_h)} \qquad (6.10)$$

where n_e and n_h are the number of ellipsoids for conduction and valence band.

When the density of states, effective masses for electrons and holes, have similar magnitudes, the Fermi level is constrained towards the centre of the region of band overlap and is closer to the edge of that band containing the heavier carriers. The concept of degeneracy temperature T_D, defined by setting the Fermi energy equal to KT_D, can have no physical significance, if the band overlap increases, while the Fermi level remains pinned between the two band edges. The implication of the degeneracy temperature for a given band is that at that temperature the Fermi level is close to the band edge; this is never true for antimony: the carrier populations always remain at least partially degenerate and ξ_e and ξ_h never fall below 3.5 and 2.0 respectively.

Table (6.2) presents the carrier densities obtained by different methods at different temperatures. The carrier densities obtained from

Table (6.2) Carrier densities in antimony.

Reference	Carrier density ($\times 10^{19}/cm^3$)	Temperature (K)
Erikesson (1964	$N_e = 4.2$	1.5^o
	$N_h = 4.4$	
Epstein and Juretschke (1963)	$N_e = N_h = 4.30$	1.5^o
Ketterson and Eckstein (1963)	$N_e = N_h = 4.07$	1.15^o
Rao *et al* (1964)	$N_e = N_h = 5.05$	4.2^o
Öktü and Saunders (1967)	$N_e = N_h = 5.22$	273^o
	$= 4.12$	225^o
	$= 4.00$	183^o
	$= 3.92$	139^o
	$= 3.86$	77^o
Present work	$N_e = N_h = 4.5$	300^o
	$= 4.2$	196^o
	$= 3.9$	77^o
Windmiller and Priestley (1965)	$N_e = N_h = 5.5$	1.26^o

the present work using field dependent tensor method are about 25% less than that ($5.5 \times 10^{19}/cm^3$) obtained by the de Haas-Van Alphen effect measurements of Windmiller and Priestley (1965), while in agreement with that from the low field method ($3.86 \times 10^{19}/cm^3$) of Öktü and Saunders (1967), de Haas-Shubnikov effect data ($4.07 \times 10^{19}/cm^3$) of Ketterson and Eckstein (1963) and the ultrasonic attenuation measurements ($4.2 \times 10^{19}/cm^3$) of Eriksson *et al* (1964).

The new information obtained from the alloy measurements concerns the change in carrier concentration with alloying. From this it is possible to draw an additional conclusion about the band structure of antimony. As tin or germanium added, the density of holes increases while that of electrons decreases shown in tables (5.1) to (5.6). The fact that the hole population increases much faster than the electron population decreases, implies that the density of states in the two bands differs. In the simplest case each tin atom would remove one electron from conduction band as proved by low field method (Saunders and Öktü 1968) and de Haas-Van Alphen method (Dunsworth and Datars 1973). However, to adjust the Fermi level a number of electrons from the lower Brillouin zone must spill over into the conduction band. The number of spilled electrons depends upon the density of states in the two zones. From the present results it is possible to estimate the number of holes which each acceptor atom provides, we can do this by summing the carrier density change in the valence and conduction bands together;

For the valence band:

Number of holes in pure antimony = N_h

Number of holes in doped antimony = N_h'

Therefore, the number of holes introduced by doping $\Delta N_h = (N_h' - N_h)$ (6.11)

For the conduction band:

Number of electrons in pure antimony = N_e

Number of electrons in doped antimony = N_e'

Therefore, the number of electrons removed by doping

$\Delta N_e = (N_e - N_e')$

Then the total change in carrier density

$$\Delta N_h + \Delta N_e = (N_e - N_e') + (N_h' - N_h) \qquad (6.12)$$

Table (6.3) shows the carrier densities, total change of carrier density, the number of tin atoms added and the ratio of the carrier density. The last row indicates that all the tin atoms added are effective in changing the carrier concentration. The average value of carrier density change to tin-atom density is (1.09 ± 0.15); the rigid-band model prediction predicts 1.00. Similar calculations have been carried out for the antimony-germanium alloy (table 6.4) and the value of carrier density change to germanium atom density is 1.02. Errors in determination of the tin and germanium concentration could account for the observed differences from 1.00, specially for tin doped alloys. We used nominal concentration because of the large random error in the atomic absorption analysis. Extrapolation of our electron density with alloying indicates that the electron pocket will be empty at 1.0 at % tin or germanium see figure (6.11). This value is more than a factor of three greater than the 0.35 at % tin found by Dunsworth and Datars (1973) but our value agreed reasonably with 0.75 ± 0.05 at % tin by Harte and Priestley (1975). The conclusion to be drawn from the calculated mobility parameters and carrier densities is that germanium acts in the same way as tin when alloyed with antimony.

Table (6.3) Carrier densities in antimony-tin alloys change of density from that of pure antimony.

Tin concentration (at %)	0.00	0.50	0.75	1.00
Number of tin atoms ($10^{19} cm^{-3}$)	0.0	16.5	24.8	33
Number of electrons ($10^{19} cm^{-3}$)	3.9	0.14	0.02	0.00
Number of holes ($10^{19} cm^{-3}$)	3.9	13.5	21.5	36.0
Total change of carrier density ($10^{19} cm^{-3}$)	....	13.4	21.48	36.0
Total change/number of tin atoms	....	0.81	0.87	1.09

Table (6.4) Carrier densities in antimony-germanium alloys change of density from that of pure antimony.

Germanium concentration (at %)	0.00	1.16
Number of germanium atoms ($10^{19} cm^{-3}$)	0.0	38.3
Number of electrons ($10^{19} cm^{-3}$)	3.9	0.0
Number of holes ($10^{19} cm^{-3}$)	3.9	39.0
Total change of carrier density ($10^{19} cm^{-3}$)	....	39.0
Total change/number of germanium atoms	....	1.02

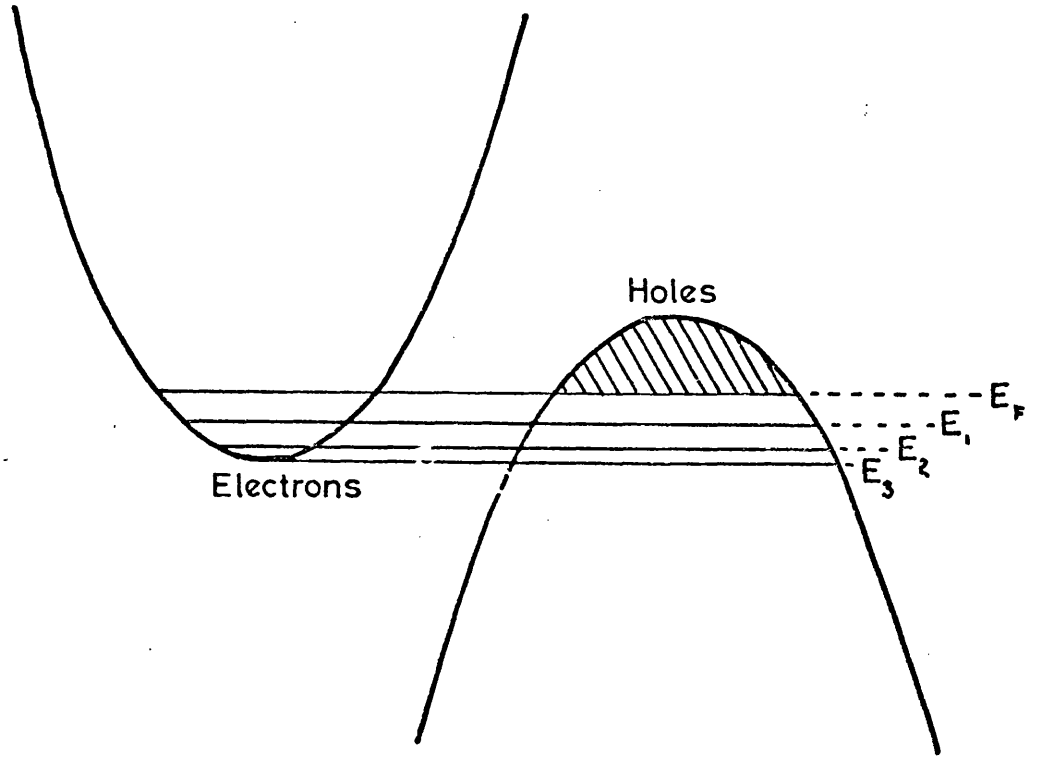

E_F Pure antimony

E_1 0.5at%tin

E_2 0.75%tin

E_3 1.0at%tin

Fig.(6.11) Band structure for antimony and antimony-tin alloys

6.5 Carrier Scattering Mechanisms

A quantitative theoretical description of the carrier scattering process in semimetals has yet to be formulated. The source of the difficulty is the observed temperature dependence of carrier mobility: $T^{-1.5}$ for antimony (present work and Öktü and Saunders 1967) and $T^{-1.7}$ for arsenic (Jeavons and Saunders 1969) between 77°K and room temperature. In semimetals, the temperature exponent x in T^x and the inverse of the relaxation time (τ^{-1}) should be proportional to the product of the phonon density and the carrier density of states (Öktü and Saunders 1967). Now the first factor is proportional to temperature and the second is a measure of the vacant sites available for occupancy by a scattered carrier which depends upon the carrier density. In the pure element for acoustic mode intravalley scattering, a mobility temperature dependence closer to $T^{-1.0}$ would be expected (see section 6.3). A stronger dependence on temperature than that of $T^{-1.0}$ has been observed and indicates that there must be some contribution from other mechanisms which could include phonon dominated, intervalley scattering, carrier - carrier scattering (included electron-electron, electron-hole and hole-hole collisions or two phonon processes).

The decrease in the temperature dependence of the mobilities for doped materials with respect to a pure semimetal will result, not only from increased impurity scattering of the carriers, but also from a quantitative change in the elctron-phonon acoustic scattering. At a high temperature, in addition to being scattered by the carriers or with other phonons, the phonons are being scattered and held near equilibrium by processes such as scattering by impurities or physical defects or by mutual interaction. In the pure element and in alloys the phonon concentration increases with temperature, but the presence of the impurities in the alloys reduces the phonon mean free path, and

therefore, the electron-phonon scattering probability is less than in the element. The temperature dependence of the carrier mobility in the alloys which results from electron-phonon scattering is reduced due to phonon-impurity scattering (thus the $T^{-1.5}$ dependence in pure antimony drops to a $T^{-0.3}$ dependence in 1.0 at % tin and a $T^{-0.2}$ dependence in 1.16 at % germanium).

In the antimony alloys phonon-electron scattering does not become important until a higher temperature than is usual for metal alloys; the measurements of resistivity as a function of temperature which is shown in figures(4.10) and (4.11) indicate that the scattering of electrons and phonons by impurities only becomes evident above 25^{o}K for antimony-tin and antimony-germanium alloys. As an example of metal rather than semimetal alloys, we can consider the indium-thallium alloys for which the scattering of electrons and phonons by impurities becomes evident above 4^{o}K (Sladek 1955), indicating that electron-phonon scattering is important at lower temperatures than it is for the antimony alloys, which is mainly because only long wavelength (λ) phonons can scatter carriers in semimetals (Heremans *et al* 1977) these are scattered by impurities and so the carriers do not see them (see section 6.3 for the value of phonon wavevector in antimony). It is noticeable that the Residual Resistivity Ratio (RRR) in semimetals is much less than that in metals (i.e. in bismuth RRR = 125 by Lerner 1962, arsenic RRR = 856 by Jeavons and Saunders 1969 and in Indium RRR = 12000 by Hurd 1974).

I - "Impurity Scattering of Carriers"

We now consider the value of mobility which can be expected in a medium containing a number of point imperfections or impurities which scatter the carriers. In our case the following considerations need to be taken into account.

(a) In general for impurity scattering in dilute alloys it is usual to take care to consider that neighbouring impurity atoms are separated from each other by a number of atoms in the host lattice; then the impurity atoms can be taken as being isolated. The alloys we have dealt with in our present work contain less than 3 at % tin or germanium; therefore, we can assume to a first approximation that the scattering problem can be reduced to that of finding the scattering probability due to the presence of one scattering centre.

(b) An approximation often made in impurity scattering theory is that the electronic energy states can still be described as Bloch states but the energy will be broadened by scattering (Heine 1960).

Scattering by phonons determines the mobility of carriers when relatively few impurity atoms are present. Then it is only at a low temperature that scattering by impurity atoms dominates, but by increasing the concentration of impurity atoms, this scattering may become more important at higher temperatures. The nature of scattering will depend on whether the impurity is neutral or ionized. The neutral atom problem is equivalent to the scattering of an electron by a hydrogen atom (Zimann 1960). In our case tin and germanium must be ionized impurities, so that the scattering mechanism we need to be concerned with is that due to ionized not neutral impurities.

II - Ionized impurity

The potential of an electron in the field of a screened single ionized impurity is

$$V(r) = \left(\frac{e}{r}\right) e^{-r/R} \tag{6.13}$$

where $\left(\frac{e}{r}\right)$ is the coulomb potential of a single electron charge and R is the screeing radius, which is roughly the effective radius of the scattering centre. If holes and electrons are both present, the screening radius for the degenerate system is given by

$$R = \frac{KT}{4\pi e^2 n'} \tag{6.14}$$

n' is a function of the number of carriers electrons or holes. The relaxation time is given as

$$\frac{1}{\tau_a(E)} = \frac{\pi}{\sqrt{2}} \frac{Z^2 e^4 N_i}{E^{2/3} m^{*\frac{1}{2}}} F(E) \tag{6.15}$$

where N_i is an ionized impurity and $F(E) = 3KT$, then the mobility takes the form

$$\mu_a = \frac{e\tau_a(E)}{m^*} \tag{6.16}$$

This formula given by Blatt (1968) is essentially the same as the result obtained by Conwell and Weisskopf (1950) who used the simple Rutherford Scattering law.

In order to obtain the contribution of the ionized impurity scattering to the mobility, we subtract the intrinsic scattering rate from the total rate as Bhargava (1967) did for doped bismuth. If μ_l and $\mu_{l(sb)}$ are the mobilities in the trigonal plane for the alloy and the pure metal respectively, the ionized scattering mobility μ_{la} is given by

$$\mu_{la} = \frac{\mu_l}{\left(1 - \frac{\mu_l}{\mu_{l(sb)}}\right)} \tag{6.17}$$

and

$$\nu_{1a} = \frac{\nu_1}{\left(1 - \frac{\nu_1}{\nu_{1(sb)}}\right)} \qquad (6.18)$$

Since the impurity scattering contribution is greater the lower the temperature, the best procedure is to calculate μ_{1a} and ν_{1a} at the lowest temperature (77°K) for which a complete set of mobility data is available. The values of $\mu_{1(sb)}$ and $\nu_{1(sb)}$ for electrons and holes in pure antimony are $2.1 m^2$/v.sec. and $2.58 m^2$/v.sec. respectively at 77°K. Table (6.5) shows the calculated ionized mobility scattering from equations (6.17) and (6.18) using the measured mobilities for antimony-tin and antimony-germanium alloys. As more tin or germanium is added so the value of ionized impurity mobility decreases as was the case in bismuth-lead alloys (Bhargava 1967).

To explain the ionized impurity scattering, two extreme cases have been discussed in the literature according to whether $kR \gg 1$ or $kR \ll 1$, where k is the carrier wave number and R is the range of the scattering potential. Bhargava (1967) has calculated the value of kR ($kR \gg 1$) for bismuth-lead alloy, and in the previous section we estimated that the value of k in antimony is much bigger than in bismuth. Therefore, in our case we can assume that $kR \gg 1$. This case has been discussed for semiconductors by Conwell and Weisskopf (1946, 1950) who used the Rutherford scattering formula cut off for small angle scattering and independently by Brooks and Herring (1954) and Dingle (1955), who used the Born approximation and a screened coulomb field.

Figure (6.12) shows the variation of hole mobility ν_{1a} with doping concentrations for antimony-tin alloys in comparison with the bismuth-lead data obtained by Bhargava (1967). In the antimony-tin system the slope is (-1.1) while in a bismuth-lead system the slope is -1.2. For bismuth $kR > 1$ for holes so that the Born approximation is not very good.

Table (6.5) Results of the ionized mobility scattering on antimony alloys at $77^{o}K$.

Alloy	Hole		Electron	
	ν_1 m^2/v.s.	ν_{1a} m^2/v.s.	μ_1 m^2/v.s.	μ_{1a} m^2/v.s.
Sb + 0.5 at % Sn	0.88	1.33	1.22	2.9
Sb + 0.75 at % Sn	0.572	0.73	0.603	0.85
Sb + 1.0 at % Sn	0.25	0.28	.....	.....
Sb + 1.16 at % Ge	0.301	0.34	.....	.....

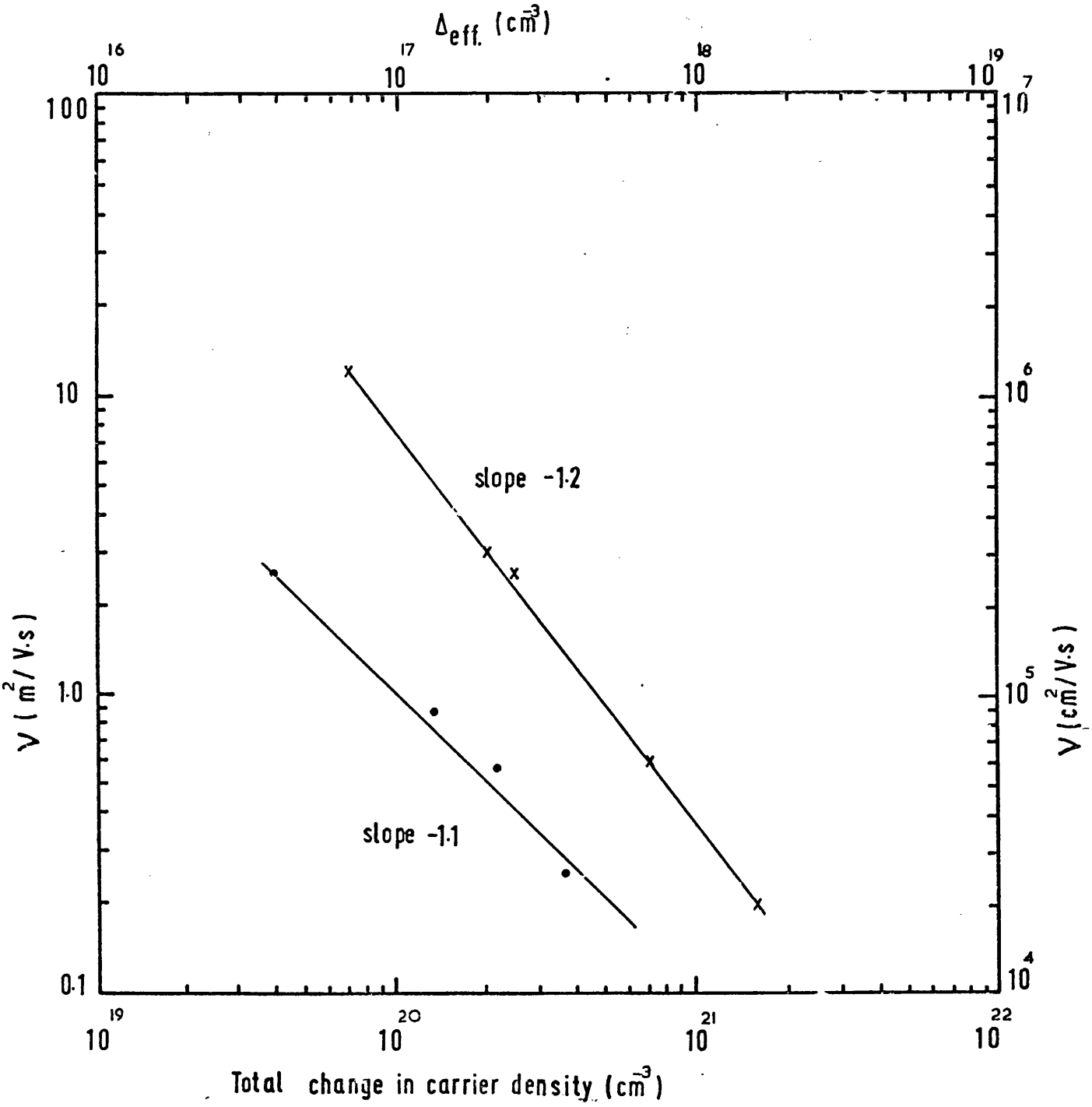

Fig.(6.12) The variation of hole mobilities as a function of doping density.

(x) bismuth-lead alloy (Bhargava 1967)
(.) antimony-tin alloy (present work), the solid is least-mean-square fit.

This may be the reason why the straight line for holes in figure (6.12) deviates from a slope of 1.0 (Bhargava 1967). However, for antimony, $kR > 1$ so that the Born approximation is rather better.

6.6 The tilt angles of the Fermi surface pockets in antimony and its alloys

The features of the galvanomagnetic data of antimony have been interpreted quantitively on the basis of a two multi-valley band model. Carrier mobilities obtained by this method match the cyclotron resonance effective masses of Datars and Vanderkooy (1964), if an isotropic relaxation time is assumed. The conclusive finding that the field dependent tensor methods are correct is the agreement between the tilt angles obtained by this method and those by other methods. Table (6.6) shows the tilt angles; one set of pockets has a small tilt angle of about -7^{o}, while the tilt angle of second set is about -31^{o}. At one time the large tilt angle ellipsoids have been assumed to contain electrons. However, for this case there are no solutions to the galvanomagnetic effects (see chapter two).

In the present work the small tilt angle -9^{o} for the electron pockets found accords with the result of other workers, shown in table (6.6), but the other tilt angle -27^{o} is not in so close agreement with the usual value of about -31^{o} (Windmiller and Priestley (1965)). Assumptions made in the model used must give rise to these discrepancies. In the present case it has been assumed that the constant energy surfaces are ellipsoidal. However, it is known that both sets of ellipsoids are in fact warped; the deviation is more marked for the hole pockets, as discussed in chapter two. Furthermore the assumptions made in carrier scattering and isotropic relaxation times might be responsible in part for the discrepancy. The effective tilt angle measured by galvanomagnetic effects is only a mean value. Tilt angles measured by the de Haas-Van Alphen effect are those of a different property, that of the

extremal cross-section of the Fermi surface.

We have collected, in table (6.6), the smallest and largest reported electron and hole tilt angles of arsenic, antimony and bismuth. The variation of the reported tilt angles over a wide range may be taken as an evidence that τ is nonsymmetric i.e. the principal axes of the mobility (or rather conductivity) and mass ellipsoids do not coincide (Akgöz 1974).

The present work shows that the tilt angles for antimony alloy single crystals are $-27^{o} \pm 1^{o}$ for hole pockets and $-9^{o} \pm 1^{o}$ for electron pockets: Saunders and Öktü (1968) using the low field method found $-24^{o} \pm 1^{o}$ for hole pockets and $-4^{o} \pm 1^{o}$ for electron pockets. In both cases the tilt angles are invariant with temperature and concentration even up to 8 at % tin.

Armed with a firm description of the tilt angles, we shall now show how to introduce them into the galvanomagnetic equations. The key equation (see, Herring and Vogt 1956) is

$$\mu = \frac{e\tau}{m^*} = e\,\tau.\alpha \qquad (6.19)$$

where μ is the mobility tensor, τ is the relaxation time tensor, m is the effective mass tensor and α is the inverse effective mass tensor ($\alpha = (m^*)^{-1}$). All the tensors in this equation are second rank polar. Equation (6.19) is defined only when all the tensors refer to the same point in the Brillouin zone. The symmetry of this point restricts the form of these tensors. Since the above equation relates the mobilities to the effective masses via the relaxation time, it may be called the bridge equation, i.e. results obtained from the galvanomagnetic measurements can be related to the fundamental parameters via equation (6.19).

Now, how does the tilt angle enter into the mobility equation expression in the crystallographic orthogonal set? For this we use the passive convention and employ clockwise and anticlockwise rotations. Rotations of an ellipsoid axes about the binary (+x) direction (which is parallel to the 1 axis of the ellipsoid) is represented by

$$R = \begin{pmatrix} 1 & 0 & 0 \\ 0 & \cos\theta & \pm\sin\theta \\ 0 & \mp\sin\theta & \cos\theta \end{pmatrix} \qquad (6.20)$$

where the upper sign is for clockwise rotations and the lower sign for anticlockwise rotations, θ is the tilt angle and its range is $0^{o} < \theta < 90^{o}$. It is convenient to insert the sign of the tilt angle into the transformation matrix R, so that θ takes positive values only.

Example (1)

The principal electron ellipsoids of antimony and its alloy. The tilt angles are negative, that is, the lower sign in equation (6.20) is used. The mobility tensor components transform as

$$\begin{aligned} \mu_{11} &= \mu_1 \\ \mu_{22} &= \mu_2 \cos^2\theta + \mu_3 \sin^2\theta \\ \mu_{33} &= \mu_2 \sin^2\theta + \mu_3 \cos^2\theta \\ \mu_{23} &= \tfrac{1}{2}(\mu_3-\mu_2) \sin 2\theta \end{aligned} \qquad (6.21)$$

The tilt angle can be obtained by

$$\tan 2\theta = \frac{2\mu_{23}}{(\mu_{33}-\mu_{22})} \qquad (6.22)$$

where $\mu_{23} > 0$ and $(\mu_{33}-\mu_{22}) > 0$.

Example (2)

The principal hole ellipsoids of antimony and its alloys. The tilt angles are negative. The hole mobility tensor components transform as

$$\begin{aligned} \nu_{11} &= \nu_1 \\ \nu_{22} &= \nu_2 \cos^2\theta + \nu_3 \sin^2\theta \\ \nu_{33} &= \nu_2 \sin^2\theta + \nu_3 \cos^2\theta \\ \nu_{23} &= \tfrac{1}{2}(\nu_3-\nu_2) \sin 2\theta \end{aligned} \tag{6.23}$$

The tilt angle can be obtained by

$$\tan 2\theta = \frac{2\nu_{23}}{(\nu_{33}-\nu_{22})} \tag{6.24}$$

The difficulty arises when $45^\circ < |\theta| < 90^\circ$, that is for the hole tilt angle of arsenic $|\theta| = 50^\circ$ (Akgöz and Saunders 1974). For this case $\nu_{23} > 0$, but $(\nu_{33}-\nu_{22}) < 0$ therefore equation (6.24) yields the complimentary tilt angle with a negative sign. This difficulty may be removed by rewriting equation (6.24) as

$$\tan 2\phi = \frac{2\nu_{23}}{(\nu_{33}-\nu_{22})} \quad \text{and} \quad \theta = \frac{\pi}{2} - \phi \tag{6.25}$$

Thus when $45^\circ < |\theta| < 90$ equation (6.25) instead of equation (6.24)

The tilt angles found by using the field dependent tensor method are essentially the same as those found by using other methods. One of the advantages of the galvanomagnetic effects in general is that it is possible to obtain from such measurements information on the band parameters - such as tilt angles - at temperatures above 4.2K, whereas most quantum methods are only applicable at helium temperatures ($\sim$4.2K). The field dependent

tensor method is particularly convenient for crystals with many-valleyed, small Fermi surface pockets as in semimetals and their alloys, and the successful determination of these properties as related to the Fermi surface is evidence of its validity.

Table (6.6) Range of the reported electron and hole tilt angles in As, Sb, Bi, Sb-Sn and As-Sb alloy. The smallest and largest (in magnitude) reported value are listed only.

Material		Electron tilt angle	Hole tilt angle
As	theoretical	-8^{o}(a)	-46^{o}(a)
	experimental	-4^{o}(b) to (-8)(c)	-50^{o}(c) to -53^{o}(d)
Sb	theoretical	-7^{o}(e)	-49^{o}(e)
	experimental	-2.3^{o}(f) to -8^{o}(g)	-24^{o}(h) to -37^{o}(f)
Bi	theoretical	$+3.5^{o}$(i) to $+10^{o}$(j)	-
	experimental	$+4.3^{o}$(k) to $+8^{o}$(ℓ)	-
As (25.5 at %) - Sb			
	experimental	-7^{o}(m)	-34^{o}(m)
Sb-Sn alloy			
	experimental	-9^{o}(n)	-27^{o}(n)

(a) Lin and Falicov (1966)
(b) Datars and Vanderkooy (1966)
(c) Jeavons and Saunders (1969)
(d) Priestley et al (1967)
(e) Falicov and Lin (1966)
(f) Windmiller (1966)
(g) Kechin (1968)
(h) Öktü & Saunders (1967)
(i) Ferreira (1968)
(j) Golin (1968)
(k) Smith *et al* (1964)
(ℓ) Gregers-Hansen (1971)
(m) Akgöz and Saunders (1974)
(n) This work.

APPENDICES

APPENDIX I

The transformation equations from the ellipsoidal axis system to the crystallographic system for the mobilities are

For electrons:

$$\mu_{11} = \mu_1$$
$$\mu_{22} = \mu_2\cos^2\theta_\mu + \mu_3\sin^2\theta_\mu$$
$$\mu_{33} = \mu_2\sin^2\theta_\mu + \mu_3\cos^2\theta_\mu$$
$$\mu_{23} = \tfrac{1}{2}(\mu_2-\mu_3)\sin 2\theta_\mu \qquad \text{(I.1)}$$

For holes:

$$\nu_{11} = \nu_1$$
$$\nu_{22} = \nu_2\cos^2\theta_\nu + \nu_3\sin^2\theta_\nu$$
$$\nu_{33} = \nu_2\sin^2\theta_\nu + \nu_3\cos^2\theta_\nu$$
$$\nu_{23} = \tfrac{1}{2}(\nu_2-\nu_3)\sin 2\theta_\nu \qquad \text{(I.2)}$$

where μ_i and ν_i are the diagonal components of the mobility tensors in the ellipsoidal axis system.

APPENDIX II

On the basis of Akgöz and Saunders (1974) the following magnetoconductivity tensor components $\sigma_{ij}(B_1,B_2,0)$ have been derived $\vec{B} = (B_1,B_2,0)$.

$$\sigma_{11}(B_1,B_2,0) = (\mu_{11}+d_eB_1^2)U_1 + \tfrac{1}{4}(\mu_{11}+3\mu_{22}+4d_eB_1^2)(U_2+U_3)$$
$$+ (\nu_{11}+d_hB_1^2)W_1 + \tfrac{1}{4}(\nu_{11}+3\nu_{22}+4d_hB_1^2)(W_2+W_3)$$

$$\sigma_{22}(B_1,B_2,0) = (\mu_{22}+d_eB_2^2)U_1 + \tfrac{1}{4}(3\mu_{11}+\mu_{22}+4d_eB_2^2)(U_2+U_3)$$
$$+ (\nu_{22}+d_hB_2^2)W_1 + \tfrac{1}{4}(3\nu_{11}+\nu_{22}+4d_hB_2^2)(W_2+W_3)$$

$$\sigma_{33}(B_1,B_20) = \mu_{33}(U_1+U_2+U_3) + \nu_{33}(W_1+W_2+W_3)$$

$$\sigma_{12}(B_1,B_20) = (\mu_{11}\mu_{23}B_2+d_eB_1B_2)\,U_1 + \{g_e-\tfrac{1}{2}\mu_{11}\mu_{23}(-\sqrt{3}B_1+B_2) + d_eB_1B_2\}U_2$$
$$+ \{-g_e-\tfrac{1}{2}\mu_{11}\mu_{23}(\sqrt{3}B_1B_2) + d_eB_1B_2\}U_3$$
$$+ (-\nu_{11}\nu_{23}B_2+d_hB_1B_2)W_1 + \{g_h-\tfrac{1}{2}\nu_{11}\nu_{23}(\sqrt{3}B_1-B_2) + d_hB_1B_2\}W_2$$
$$+ \{-g_h-\tfrac{1}{2}\nu_{11}\nu_{23}(-\sqrt{3}B_1-B_2) + d_hB_1B_2\}W_3$$

$$\sigma_{13}(B_1,B_2,0) = \mu_{11}\mu_{33}B_2U_1 + \{\frac{\sqrt{3}}{2}\mu_{23} - k_eB_1 + \tfrac{1}{4}(\mu_{11}\,_{33}+\frac{3d_e}{\mu_{11}})B_2\}U_2$$
$$+ \{-\frac{\sqrt{3}}{2}\mu_{23} + k_eB_1 + \tfrac{1}{4}(\mu_{11}\mu_{33}+\frac{3d_e}{\mu_{11}})B_2\}U_3 - \nu_{11}\nu_{33}B_2W_1$$
$$- \{-\frac{\sqrt{3}}{2}\nu_{23} - k_hB_1 - \tfrac{1}{4}(\nu_{11}\nu_{33}+\frac{3d_h}{\nu_{11}})B_2\}W_2$$
$$+ \{-\frac{\sqrt{3}}{2}\nu_{23} - k_hB_1 - \tfrac{1}{4}(\nu_{11}\nu_{33}+\frac{3d_h}{\nu_{11}})B_2\}W_3$$

$$\sigma_{23}(B_1,B_2,0) = (\mu_{23}-\frac{d_e}{\mu_{11}}B_1)U_1 + \{-\tfrac{1}{2}\mu_{23}-\tfrac{1}{4}(3\mu_{11}\mu_{33}+\frac{d_e}{\mu_{11}})B_1 + k_eB_2\}U_2$$
$$+ \{-\tfrac{1}{2}\mu_{23}-\tfrac{1}{4}(3\mu_{11}\mu_{33}+\frac{d_e}{\mu_{11}})B_1 - k_eB_2\}U_3$$
$$+ (\nu_{23}+\frac{d_h}{\nu_{11}}B_1)W_1 + \{-\tfrac{1}{2}\nu_{23}+\tfrac{1}{4}(3\nu_{11}\nu_{33}+\frac{d_h}{\nu_{11}})B_1-k_hB_2\}W_2$$
$$+ \{-\tfrac{1}{2}\nu_{23}+\tfrac{1}{4}(3\nu_{11}\nu_{33}+\frac{d_h}{\nu_{11}})B_1+k_hB_2\}W_3 \qquad \text{II.1}$$

where

$$d_e = \mu_{11}(\mu_{22}\mu_{33}-\mu_{23}^2) \qquad d_h = \nu_{11}(\nu_{22}\nu_{33}-\nu_{23}^2)$$

$$g_e = \frac{\sqrt{3}}{4}(\mu_{11}-\mu_{22}) \qquad g_h = \frac{\sqrt{3}}{4}(\nu_{11}-\nu_{22})$$

$$k_e = \frac{\sqrt{3}}{4}(\mu_{11}\mu_{33}-\frac{d_e}{\mu_{11}}) \qquad k_h = \frac{\sqrt{3}}{4}(\nu_{11}\nu_{33}-\frac{d_h}{\nu_{11}}) \qquad \text{II.2}$$

$B_1 = B\cos\phi, B_2 = B\sin\phi$ where $B = |\vec{B}|$ and ϕ is the rotation angle taken round the xy plane (the sense of rotation is taken from $+x$ direction towards $+y$ direction).

$$U_1 = ne(1+\frac{d_e}{\mu_{11}}B_1^2+\mu_{11}\mu_{33}B_2^2)^{-1}$$

$$U_2 = ne\{1+\tfrac{1}{4}(3\mu_{11}\mu_{33}+\frac{d_e}{\mu_{11}})B_1^2+\tfrac{1}{4}(\mu_{11}\mu_{33}+\frac{3d_e}{\mu_{11}}) \times B_2^2 - \frac{\sqrt{3}}{2}(\mu_{11}\mu_{33}-\frac{d_e}{\mu_{11}})B_1B_2\}^{-1}$$

$$U_3 = ne\{1+\tfrac{1}{4}(3\mu_{11}\mu_{33}+\frac{d_e}{\mu_{11}})B_1^2+\tfrac{1}{4}(\mu_{11}\mu_{33}+\frac{3d_e}{\mu_{11}}) \times B_2^2 + \frac{\sqrt{3}}{2}(\mu_{11}\mu_{33}-\frac{d_e}{\mu_{11}})B_1B_2\}^{-1} \qquad \text{II.3}$$

where n is the number of carriers per ellipsoid. W_1, W_2, W_3 are obtained from equations (II.3) by replacing U_i by W_i, μ_{ij} by ν_{ij} and d_e by d_h. The remaining tensor components $\sigma_{21}(B_1,B_2,0)$, $\sigma_{31}(B_1,B_2,0)$, and $\sigma_{32}(B_1,B_2,0)$ can be obtained from the Onsager relation $\sigma_{ij}(\vec{B}) = \sigma_{ji}(-\vec{B})$.

APPENDIX III

On the basis of Akgöz and Saunders (1974) expressions, the following magnetoconductivity tensor components $\sigma_{ij}(0,B2,B3)$

$\bar{B} = (0,B2,B3)$

$$
\begin{aligned}
\sigma_{11}(B_2,B_3) &= \left[\mu_{11}U(1) + \tfrac{1}{4}(\mu_{11}+3\mu_{22})\,(U(2)+U(3))\right] \\
&+ \left[\nu_{11}V(1) + \tfrac{1}{4}(\nu_{11}+3\nu_{22})\,(V(2)+V(3))\right] \\
\sigma_{22}(B_2,B_3) &= \left[(\mu_{22}+d_e B_2^2)U(1) + \tfrac{1}{4}(3\mu_{11}+\mu_{22}+4d_e B_2^2)\,(U(2)+U(3))\right] \\
&+ \left[(\nu_{22}+d_h B_2^2)\,V(1) + \tfrac{1}{4}(3\nu_{11}+\nu_{22}+4d_h B_2^2)\,(V(2)+V(3))\right] \\
\sigma_{33}(B_2,B_3) &= \left[(\mu_{33}+d_e B_3^2)\,(U(1)+U(2)+U(3))\right] \\
&+ \left[(\nu_{33}+d_h B_3)\,(V(1)+V(2)+V(3))\right] \\
\sigma_{12}(B_2,B_3) &= \Big[-\mu_{11}(-\mu_{22}B_3)U(1) + \big(\tfrac{\sqrt{3}}{2}\,(\mu_{11}-\mu_{22}) \\
&+ \mu_{11}\mu_{22}B_3\big)U(2) + \big(-\tfrac{\sqrt{3}}{2}\,(\mu_{11}-\mu_{22}) \\
&+ \mu_{11}\mu_{22}B_3\big)U(3)\Big] + \Big[-\nu_{22}B_3V(1) \\
&+ \big(\tfrac{\sqrt{3}}{2}\,(\nu_{11}-\nu_{22}) + \tfrac{1}{2}\nu_{11}\nu_{23}B_2 + \nu_{11}\nu_{22}B_3\big)V(2) \\
&+ \big(-\tfrac{\sqrt{3}}{2}\,(\nu_{11}-\nu_{22}) + \nu_{11}\nu_{22}B_3\big)V(3)\Big] \\
\sigma_{23}(B_2,B_3) &= \Big[\mu_{23}U(1) + \Big[-\tfrac{1}{2}\mu_{23} - \tfrac{\sqrt{3}}{2}\,\mu_{11}\mu_{23}B_3\Big] + U(2) \\
&+ \Big[-\tfrac{1}{2}\mu_{23} + \tfrac{\sqrt{3}}{2}\,\mu_{11}\mu_{23}B_3 +\Big]U(3)\Big] \\
&+ \Big[(\nu_{23}+d_h B_2 B_3)V(1) + \Big[-\tfrac{1}{2}\nu_{23} - \tfrac{\sqrt{3}}{2}\,\nu_{11}\nu_{23}B_3 +\Big]V(2) \\
&+ \Big[-\tfrac{1}{2}\nu_{23} + \tfrac{\sqrt{3}}{2}\,\nu_{11}\nu_{23}B_3\Big] + V(3)\Big] \\
\sigma_{13}(B_2,B_3) &= \Big[-\mu_{11}(-\mu_{23}B_3)U(1) + \Big[\tfrac{\sqrt{3}}{2}\,\mu_{23} - \tfrac{1}{2}\mu_{11}\mu_{23}B_3\Big]U(2) \\
&+ \Big[-\tfrac{\sqrt{3}}{2}\,\mu_{23} - \tfrac{1}{2}\mu_{11}\mu_{23}B_3\Big]U(3)\Big] \\
&+ \Big[-\nu_{11}(-\nu_{23}B_3)V(1) + \Big[\tfrac{\sqrt{3}}{2}\,\nu_{23} - \tfrac{1}{2}\nu_{11}\nu_{23}B_3\Big]V(2) \\
&+ \Big[-\tfrac{\sqrt{3}}{2}\,\nu_{23} - \tfrac{1}{2}\nu_{11}\nu_{23}B_3\Big]V(3)\Big] \qquad \text{III.1}
\end{aligned}
$$

$$d_e = \mu_{11}(\mu_{22}\mu_{33}-\mu_{23}^2)$$

$$d_h = \nu_{11}(\nu_{22}\nu_{33}\ \nu_{23}^2) \qquad \text{III.2}$$

$B_2 = B\cos\phi$, $B_2 = B\sin\phi$ where $B = |\vec{B}|$ and ϕ is the ! rotation angle taken round the YZ plane (the sense of rotation is from +y direction towards +z).

$$U(1) = ne\left[1 + \mu_{11}(\mu_{33}B_2^2 - 2\mu_{23}B_2B_3 + \mu_{22}B_3^2)\right]^{-1}$$

$$U(2) = ne\left[1 + \tfrac{1}{4}(\mu_{11}\mu_{33} + \frac{3d_e}{\mu_{11}})B_2^2 + \mu_{11}\mu_{22}B_3^2 + \mu_{11}\mu_{23}B_2B_3\right]^{-1}$$

$$U(3) = U(2)$$

$$V(1) = ne\left[1 + \nu_{11}\ (\nu_{33}B_2^2 - 2\nu_{23}B_2B_3 + \nu_{22}B_3^2)\right]^{-1}$$

$$V(2) = ne\left[1 + \tfrac{1}{4}(\nu_{11}\nu_{33} + \frac{3d_h}{\nu_{11}})B_2^2 + \nu_{11}\nu_{22}B_3^2 + \nu_{11}\nu_{23}B_2B_3\right]^{-1}$$

$$V(3) = V(2) \qquad \text{III.3}$$

The remaining tensor components $\sigma_{21}(0,B2,B3) - \sigma_{31}(0,B2,B3)$ and $\sigma_{32}(0,B2,B3)$ can be obtained from the onsager relation $\sigma_{ij}(\bar{B}) = \sigma_{ji}(-B)$.

APPENDIX IV

On the basis of Akgöz and Saunders (1974) expressions, the following magnetoconductivity tensor components $\sigma_{ij}(B1,0,B3)$ have been derived.

$\bar{B} = (B1,0,B3)$

$$\sigma_{11}(B1,0,B3) = \left[(\mu_{11}+d_e B_1^2)\ U1 + \tfrac{1}{4}(\mu_{11}+3\mu_{22}+4d_e B_1^2)\ (U2+U3)\right] + \left[(\nu_{11}+d_h B_1^2)W1 + \tfrac{1}{4}(\nu_{11}+3\nu_{22}+4d_h B_1^2)\ (W2+W3)\right]$$

$$\sigma_{22}(B1,0,B3) = \left[\mu_{22}U1 + \tfrac{1}{4}(3\mu_{11}+\mu_{22})\ (U2+U3)\right] + \left[\nu_{22}W1 + \tfrac{1}{4}(\nu_{11}+3\nu_{22})\ (W2+W3)\right]$$

$$\sigma_{33}(B1,0,B3) = \left[(\mu_{33}+d_e B_3^2)\ (U1+U2+U3)\right] + \left[(\nu_{33}+d_h B_3^2)\ (W1+W2+W3)\right]$$

$$\sigma_{12}(B1,0,B3) = \left[\mu_{11}\mu_{22}B3U1 + (g_e + \frac{\sqrt{3}}{2}\mu_{11}\mu_{23}B1 + \mu_{11}\mu_{22}B3 + \frac{\sqrt{3}}{2}(\mu_{11}-\mu_{22}))U2 + (-g_e - \frac{\sqrt{3}}{2}\mu_{11}\mu_{23}B1 - \frac{\sqrt{3}}{2}(\mu_{11}-\mu_{22}) + \mu_{11}\mu_{22}B3)U3\right] + \left[\nu_{11}\nu_{22}B3W1 + (g_h + \frac{\sqrt{3}}{2}\nu_{11}\nu_{23}B1 + \nu_{11}\nu_{22}B3 + \frac{\sqrt{3}}{2}(\nu_{11}-\nu_{22}))W2 + (-g_h - \frac{\sqrt{3}}{2}\nu_{11}\nu_{23}B1 - \frac{\sqrt{3}}{2}(\nu_{11}-\nu_{22}) + \nu_{11}\nu_{22}B3)W3\right]$$

$$\sigma_{13}(B1,0,B3) = \left[\mu_{11}\mu_{23}B3U1 + (\frac{\sqrt{3}}{2}\mu_{23} - \tfrac{1}{2}\mu_{11}\mu_{23}B3 - k_e B1)U2 + (-\frac{\sqrt{3}}{2}\mu_{23} + k_e B1 - \tfrac{1}{2}\mu_{11}\mu_{23}B3)U3\right] + \left[\nu_{11}\nu_{23}B3W1 + (\frac{\sqrt{3}}{2}\nu_{23} - \tfrac{1}{2}\nu_{11}\nu_{23}B3 - k_h B1)W2 + (-\frac{\sqrt{3}}{2}\nu_{23} + k_h B1 - \tfrac{1}{2}\nu_{11}\nu_{23}B3)W3\right] \qquad \text{IV.1}$$

$$d_e = \mu_{11}(\mu_{22}\mu_{33}-\mu_{23}^2)$$

$$g_e = \tfrac{1}{4}\sqrt{3}(\mu_{11}-\mu_{22})$$

$$k_e = \tfrac{1}{4}\sqrt{3}(\mu_{11}\mu_{33} - \frac{d_e}{\mu_{11}})$$

$$d_h = \nu_{11}(\nu_{22}\nu_{33}-\nu_{23}^2)$$

$$g_h = \tfrac{1}{4}\sqrt{3}(\nu_{11}-\nu_{22})$$

$$k_h = \tfrac{1}{4}\sqrt{3}(\nu_{11}\nu_{33} - \frac{d_h}{\nu_{11}})$$

$$Q1 = \sqrt{\frac{3}{2}} \qquad \text{IV.2}$$

$B_1 = B\cos\phi$, $B_3 = B\sin\phi$ where $B = |\bar{B}|$ and ϕ is the rotation angle taken round the XZ plane (the sense of rotation is taken from $+x$ direction towards $+z$ direction).

$$U1 = ne\left(1 + \frac{d_e}{\mu_{11}} B_1^2 + \mu_{11}\mu_{22}B_3^2\right)^{-1}$$

$$U2 = ne\left[1 + \tfrac{1}{4}(3\mu_{11}\mu_{33} + \frac{d_e}{\mu_{11}})B_1^2 + \mu_{11}\mu_{22}B_3^2\right]^{-1}$$

$$U3 = U2$$

$$W1 = pe\left\{1 + \frac{d_h}{\nu_{11}} B_1^2 + \nu_{11}\nu_{22}B_3^2\right\}^{-1}$$

$$W2 = pe\left\{1 + \tfrac{1}{4}\,(3\nu_{11}\nu_{33} + \frac{d_h}{\nu_{11}})B_1^2 + \nu_{11}\nu_{22}B_3^2\right\}^{-1}$$

$$W3 = W2 \qquad \text{IV.3}$$

The remaining tensor components $\sigma_{21}(B1,0,B3)$, and $\sigma_{31}(B1,0,B3)$ and $\sigma_{32}(B1,0,B3)$ can be obtained from the onsager relation $\sigma_{ij}(\bar{B}) = \sigma_{ji}(-\bar{B})$.

APPENDIX V

This was the computer program used to calculate the band parameters of antimony and its alloy single crystals. Some symbols employed in the program are different from those given in appendices II, III and IV. The definitions are as follows:

In the equations	In the program
μ_1	MU(1)
μ_2	MU(2)
μ_3	MU(3)
θ_μ	MU(4)
ν_1	NU(5)
ν_2	NU(6)
ν_3	NU(7)
θ_ν	NU(8)
N	A(9)
P	A(10)
μ_{11}	X(1)
μ_{22}	X(2)
μ_{33}	X(3)
μ_{23}	X(4)
ν_{11}	X(5)
ν_{22}	X(6)
ν_{33}	X(7)
ν_{23}	X(8)
N_{13}	X(9)
P_{13}	X(10)

In the equations	In the program
co.	corresponding value
z	calculated value
w	weight factors
E	Electron contribution
H	Hole contribution
Q	1.6×10^{19}C
$S(i)$	The magnetoresistivity tensor equation as a function of orientation of magnetic field
B	magnetic field
BC	B_1
BS	B_2
T_1	Tilt angle for electron pockets
T_2	Tilt angle for hole pockets
C_{ij}	$\sigma_{ij}(B1,B2)$
R_{ij}	$\sigma_{ij}(B1,B3)$

```
**********************************************************************************************
**********************************************************************************************
**********************************************************************************************

        BPYJ40: BPY21A              BPYJ40: BPY21A              BPYJ40: BPY21A
        BPYJ40: BPY21A              BPYJ40: BPY21A              BPYJ40: BPY21A

**********************************************************************************************
**********************************************************************************************
**********************************************************************************************


J40:BPY21A.FCN   (F1496 )    FOR USER BPYJ40                          ON PLAIN  19:41:43

         SUBROUTINE FCN(NPAR,G,SUM,X,IFLAG)
         DIMENSION G(10),X(10),CO(16),Z(16),Q(16),P(10),W(16),
        1U1(4),U2(4),U3(4),U4(4),U5(4),U6(4),C11(4),C22(4),C33(4),C12(4),
        2C21(4),C23(4),C32(4),C13(4),C31(4),C(4),V1(4),V2(4),V3(4),V4(4),
        3V5(4),V6(4),R11(4),R22(4),R33(4),R12(4),R21(4),R23(4),R32(4),
        4R13(4),R31(4),R(4),EC11(4),EC22(4),EC33(4),EC12(4),EC21(4),
        5EC23(4),EC32(4),EC13(4),EC31(4),HC11(4),HC22(4),HC33(4),
        6HC12(4),HC21(4),HC23(4),HC32(4),HC13(4),HC31(4),ER11(4),ER22(4),
        7ER33(4),ER12(4),ER21(4),ER23(4),ER32(4),ER13(4),ER31(4),
        8HR11(4),HR22(4),HR33(4),HR12(4),HR21(4)
    1   FORMAT (8E10.1)
    2   FORMAT (16F5.1)
    3   FORMAT (I2)
   18   FORMAT ('SOLUTION',/,4X,'MU(1)',7X,'MU(2)',7X,'MU(3)',7X,'MU(4)',
        17X,'NU(1)',7X,'NU(2)',7X,'NU(3)',7X,'NU(4)',7X,'A(9)',/,7X,'A(10)'
        210(1X,E11.3),/)
   12   FORMAT (' ',10X,'MEASURED COEFFICIENTS',/,2(8(E11.4,1X),/))
   13   FORMAT (' ',10X,'COMPUTED COEFFICIENTS',/,2(8(E11.4,1X),/))
   14   FORMAT (' ',10X,'QUALITY FACTOR',/,2(8(F11.3,1X),/))
   15   FORMAT (' ',10X,'SUM',10X,F18.6,////)
   16   FORMAT (20X,'SUBCOEFFICIENTS',/,68(4(E12.4,4X),/))
   17   FORMAT (' ','FINAL RESALTS',/,3(1X,E11.3),1X,F6.2,1X,
        13(1X,E11.3),1X,F6.2,2(1X,E11.3),/)
        GO TO (10,40,40,40,40),IFLAG
   10   READ (5,3) N
        READ (5,1) CO
        READ (5,2) (W(K),K=1,N)
   40   SUM=0.0
        CALL XYZ(X,Z,U1,U2,U3,EC11,EC22,EC33,EC12,EC21,EC23,EC32,EC13,
       1         EC31,U4,U5,U6,HC11,HC22,HC33,HC12,HC21,HC23,HC32,
       2         HC13,HC31,C11,C22,C33,C12,C21,C23,C32,C13,C31,C,V1,V2,
       3         V3,ER11,ER22,ER33,ER12,ER21,ER23,ER32,ER13,ER31,V4,V5,
       4         V6,HR11,HR22,HR33,HR12,HR21,HR23,HR32,HR13,HR31,
       5         R11,R22,R33,R12,R21,R23,R32,R13,R31,R)
        DO 41 K=1,N
        Q(K)=CO(K)/Z(K)
   41   SUM=SUM+(W(K)*(Q(K)-1.0))**2
        IF(IFLAG.NE.3) RETURN
        N1=N+1
        DO 22 K=N1,16
        Z(K)=0.0
        CO(K)=0.0
   22   Q(K)=0.0
        T1= ATAN((2.0*X(4))/(X(2)-X(3)))
        T2= ATAN((2.0*X(8))/(X(6)-X(7)))
        P(1)=X(1)
```

```
      P(2)=0.5*(X(2)+X(3))+0.5*(X(2)-X(3))/ COS(T1)
      P(3)=0.5*(X(2)+X(3))-0.5*(X(2)-X(3))/ COS(T1)
      P(4)=(90.0/3.1416)*T1
      P(5)=X(5)
      P(6)=0.5*(X(6)+X(7))+0.5*(X(6)-X(7))/ COS(T2)
      P(7)=0.5*(X(6)+X(7))-0.5*(X(6)-X(7))/ COS(T2)
      P(8)=(90.0/3.1416)*T2
      P(9)=3.0*X(9)
      P(10)=3.0*X(10)
      WRITE (6,18) X
      WRITE (6,12) CO
      WRITE (6,13) Z
      WRITE (6,14) Q
      WRITE (6,15) SUM
      WRITE (6,16) U1,U2,U3,EC11,EC22,EC33,EC12,EC21,EC23,EC32,EC13,
     1 EC31,U4,U5,U6,HC11,HC22,HC33,HC12,HC21,HC23,HC32,HC13,HC31,
     2 C11,C22,C33,C12,C21,C23,C32,C13,C31,C,V1,V2,V3,ER11,ER22,
     3 ER33,ER12,ER21,ER23,ER32,ER13,ER31,V4,V5,V6,HR11,HR22,
     4 HR33,HR12,HR21,HR23,HR32,HR13,HR31,R11,R22,R33,R12,R21,R23,
     5R32,R13,R31,R
      WRITE (6,17) P
      RETURN
      END
```

J40:BPY21A.FCN (F1406) FOR USER BPYJ40 COMPLETED AT 19:42:08 69 L1

```
**********************************************************************************************
**********************************************************************************************
**********************************************************************************************

          BPYJ40; BPY21A              BPYJ40; BPY21A              BPYJ40; BPY21A
          BPYJ40; BPY21A              BPYJ40; BPY21A              BPYJ40; BPY21A

**********************************************************************************************
**********************************************************************************************
**********************************************************************************************

BPYJ40;BPY21A.XYZ   (F1496 )    FOR USER BPYJ40                          ON PLAIN  19;42

      SUBROUTINE XYZ(A,S,U1,U2,U3,EC11,EC22,EC33,EC12,EC21,EC23,EC32,
     1EC13,EC31,U4,U5,U6,HC11,HC22,HC33,HC12,HC21,HC23,HC32,HC13,HC31,
     2C11,C22,C33,C12,C21,C23,C32,C13,C31,C,V1,V2,V3,ER11,ER22,ER33,
     3ER12,ER21,ER23,ER32,ER13,ER31,V4,V5,V6,HR11,HR22,HR33,HR12,HR21,
     4HR23,HR32,HR13,HR31,R11,R22,R33,R12,R21,R23,R32,R13,R31,R)
      DIMENSION A(10),S(16),U1(4),U2(4),U3(4),EC11(4),EC22(4),EC33(4),
     1EC12(4),EC21(4),EC23(4),EC32(4),EC13(4),EC31(4),U4(4),U5(4),U6(4),
     2HC11(4),HC22(4),HC33(4),HC12(4),HC21(4),HC23(4),HC32(4),HC13(4),
     3HC31(4),C11(4),C22(4),C33(4),C12(4),C21(4),C23(4),C32(4),C13(4),
     4C31(4),C(4),V1(4),V2(4),V3(4),ER11(4),ER22(4),ER33(4),ER12(4),
     5ER21(4),ER23(4),ER32(4),ER13(4),ER31(4),V4(4),V5(4),V6(4),HR11(4)
     6,HR22(4),HR33(4),HR12(4),HR21(4),HR23(4),HR32(4),HR13(4),HR31(4),
     7R11(4),R22(4),R33(4),R12(4),R21(4),R23(4),R32(4),
     8R13(4),R31(4),R(4)
      INTEGER I,KD
      REAL Q,B,D
      Q=1.6
      KD=0
      DO 55 I=1,4
      B=1.33
      D=KD/57.29578
      IF (KD-90) 2,3,2
    2 CD=COS(D)
      SD=SIN(D)
      GO TO 4
    3 CD=0.0
      SD=1.0
    4 DA=A(2)*A(3)-A(4)**2
      DE=A(1)*DA
      DB=A(6)*A(7)-A(8)**2
      DH=A(5)*DB
      G=Q*A(9)
      H=Q*A(10)
      BC=B*CD
      BS=B*SD
      A12=A(1)*A(2)
      A56=A(5)*A(6)
      A1M2=A(1)-A(2)
      A5M6=A(5)-A(6)
      A13=A(1)*A(3)
      A57=A(5)*A(7)
      A14=A(1)*A(4)
      A58=A(5)*A(8)
      Q3=SQRT(3.0)
      Q2=Q3/2.0
```

```
 U1(I)=G/(1.0+DA*BC**2+A13*BS**2)
 U2(I)=G/(1.0+0.25*(3.0*A13+DA)*BC**2+0.25*(A13+3.0*DA)*BS**2
1-Q2*(A13-DA)*BC*BS)
 U3(I)=G/(1.0+0.25*(3.0*A13+DA)*BC**2+0.25*(A13+3.0*DA)*BS**2
1       +Q2*(A13-DA)*BC*BS)
 U4(I)=H/(1.0+DB*BC**2+A57*BS**2)
 U5(I)=H/(1.0+0.25*(3.0*A57+DB)*BC**2+0.25*(A57+3.0*DB)*BS**2
1       -Q2*(A57-DB)*BC*BS)
 U6(I)=H/(1.0+0.25*(3.0*A57+DB)*BC**2+0.25*(A57+3.0*DB)*BS**2
1       +Q2*(A57-DB)*BC*BS)
 EC11(I)=(A(1)+DE*BC**2)*U1(I)+0.25*(A(1)+3.0*A(2)+4.0*DE*BC**2)
1         *(U2(I)+U3(I))
 HC11(I)=(A(5)+DH*BC**2)*U4(I)+0.25*(A(5)+3.0*A(6)+4.0*DH*BC**2)
1         *(U5(I)+U6(I))
 C11(I) =EC11(I)+HC11(I)
 EC22(I)=(A(2)+DE*BS**2)*U1(I)+0.25*(3.0*A(1)+A(2)+4.0*DE*BS**2)
1         *(U2(I)+U3(I))
 HC22(I)=(A(6)+DH*BS**2)*U4(I)+0.25*(3.0*A(5)+A(6)+4.0*DH*BS**2)
1         *(U5(I)+U6(I))
 C22(I) =EC22(I)+HC22(I)
 EC33(I)=A(3)*(U1(I)+U2(I)+U3(I))
 HC33(I)=A(7)*(U4(I)+U5(I)+U6(I))
  C33(I)=EC33(I)+HC33(I)
 EC12(I)=(A14*BS+DE*BC*BS)*U1(I)+(Q4*A1M2-A14*(-Q2*BC+0.5*BS)
1         +DE*BC*BS)*U2(I)+(-Q4*A1M2-A14*(Q2*BC+0.5*BS)
2         +DE*BC*BS)*U3(I)
 HC12(I)=(-A58*BS+DH*BC*BS)*U4(I)+(Q4*A5M6-A58*(Q2*BC-0.5*BS)
1         +DH*BC*BS)*U5(I)+(-Q4*A5M6-A58*(-Q2*BC-0.5*BS)
2         +DH*BC*BS)*U6(I)
  C12(I)=EC12(I)+HC12(I)
 EC21(I)=(-A14*BS+DE*BC*BS)*U1(I)+(Q4*A1M2-A14*(Q2*BC-0.5*BS)
1         +DE*BC*BS)*U2(I)+(-Q4*A1M2-A14*(-Q2*BC-0.5*BS)+DE*BC*BS)
2         *U3(I)
 HC21(I)=(A58*BS+DH*BC*BS)*U4(I)+(Q4*A5M6-A58*(-Q2*BC+0.5*BS)
1         +DH*BC*BS)*U5(I)+(-Q4*A5M6-A58*(Q2*BC+0.5*BS)+DH*BC*BS)
2         *U6(I)
 C21(I)=EC21(I)+HC21(I)
 EC23(I)=(A(4)-DA*BC)*U1(I)+(-0.5*A(4)-0.25*(3.0*A13+DA)*BC
1         +Q4*(A13-DA)*BS)*U2(I)+(-0.5*A(4)-0.25*(3.0*A13+DA)*BC
2         -Q4*(A13-DA)*BS)*U3(I)
 HC23(I)=(A(8)+DB*BC)*U4(I)+(-0.5*A(8)+0.25*(3.0*A57+DB)*BC
1         -Q4*(A57-DB)*BS)*U5(I)+(-0.5*A(8)+0.25*(3.0*A57+DB)*BC
2         +Q4*(A57-DB)*BS)*U6(I)
  C23(I)=EC23(I)+HC23(I)
 EC32(I)=(A(4)+DA*BC)*U1(I)+(-0.5*A(4)+0.25*(3.0*A13+DA)*BC
1         -Q4*(A13-DA)*BS)*U2(I)+(-0.5*A(4)+0.25*(3.0*A13+DA)*BC
2         +Q4*(A13-DA)*BS)*U3(I)
 HC32(I)=(A(8)-DB*BC)*U4(I)+(-0.5*A(8)-0.25*(3.0*A57+DB)*BC
1         +Q4*(A57-DB)*BS)*U5(I)+(-0.5*A(8)-0.25*(3.0*A57+DB)*BC
2         -Q4*(A57-DB)*BS)*U6(I)
  C32(I)=EC32(I)+HC32(I)
 EC13(I)=A13*BS*U1(I)+(Q2*A(4)-Q4*(A13-DA)*BC+0.25*(A13+3.0*DA)
1         *BS)*U2(I)+(-Q2*A(4)+Q4*(A13-DA)*BC
2         +0.25*(A13+3.0*DA)*BS)*U3(I)
 HC13(I)=-A57*BS*U4(I)+(Q2*A(8)+Q4*(A57-DB)*BC-0.25*(A57+3.0*DB)
1         *BS)*U5(I)+(-Q2*A(8)-Q4*(A57-DB)*BC
2         -0.25*(A57+3.0*DB)*BS)*U6(I)
  C13(I)=EC13(I)+HC13(I)
 EC31(I)=-A13*BS*U1(I)+(Q2*A(4)+Q4*(A13-DA)*BC-0.25*(A13+3.0*DA)
1         *BS)*U2(I)+(-Q2*A(4)-Q4*(A13-DA)*BC
```

```
2         -0.25*(A13+3.0*DA)*BS)*U3(I)
 HC31(I)=A57*BS*U4(I)+(Q2*A(8)-Q4*(A57-DB)*BC+0.25*(A57+3.0*DB)
1         *BS)*U5(I)+(-Q2*A(8)+Q4*(A57-DB)*BC
2         +0.25*(A57+3.0*DB)*BS)*U6(I)
  C31(I)=EC31(I)+HC31(I)
 V1(I)=G/(1.0+DA*BC**2+A12*BS**2)
 V2(I)=G/(1.0+0.25*(3.0*A13+DA)*BC**2+A12*BS**2-Q3*A14*BC*BS)
 V3(I)=G/(1.0+0.25*(3.0*A13+DA)*BC**2+A12*BS**2+Q3*A14*BC*BS)
 V4(I)=H/(1.0+DB*BC**2+A56*BS**2)
 V5(I)=H/(1.0+0.25*(3.0*A57+DB)*BC**2+A56*BS**2-Q3*A58*BC*BS)
 V6(I)=H/(1.0+0.25*(3.0*A57+DB)*BC**2+A56*BS**2+Q3*A58*BC*BS)
 ER11(I)=(A(1)+DE*BC**2)*V1(I)+0.25*(A(1)+3.0*A(2)+4.0*DE*BC**2)
1         *(V2(I)+V3(I))
 HR11(I)=(A(5)+DH*BC**2)*V4(I)+0.25*(A(5)+3.0*A(6)+4.0*DH*BC**2)
1         *(V5(I)+V6(I))
  R11(I)=ER11(I)+HR11(I)
 ER22(I)=A(2)*V1(I)+0.25*(3.0*A(1)+A(2))*(V2(I)+V3(I))
 HR22(I)=A(6)*V4(I)+0.25*(3.0*A(5)+A(6))*(V5(I)+V6(I))
  R22(I)=ER22(I)+HR22(I)
 ER33(I)=(A(3)+DE*BS**2)*(V1(I)+V2(I)+V3(I))
 HR33(I)=(A(7)+DH*BS**2)*(V4(I)+V5(I)+V6(I))
  R33(I)=ER33(I)+HR33(I)
 ER12(I)=-A12*BS*V1(I)+(Q4*A1M2+Q2*A14*BC-A12*BS)*V2(I)
1         +(-Q4*A1M2-Q2*A14*BC-A12*BS)*V3(I)
 HR12(I)=A56*BS*V4(I)+(Q4*A5M6-Q2*A58*BC+A56*BS)*V5(I)
1         +(-Q4*A5M6+Q2*A58*BC+A56*BS)*V6(I)
  R12(I)=ER12(I)+HR12(I)
 ER21(I)=A12*BS*V1(I)+(Q4*A1M2-Q2*A14*BC+A12*BS)*V2(I)
1         +(-Q4*A1M2+Q2*A14*BC+A12*BS)*V3(I)
 HR21(I)=-A56*BS*V4(I)+(Q4*A5M6+Q2*A58*BC-A56*BS)*V5(I)
1         +(-Q4*A5M6-Q2*A58*BC-A56*BS)*V6(I)
  R21(I)=ER21(I)+HR21(I)
 ER23(I)=(A(4)-DA*BC)*V1(I)+(-0.5*A(4)-0.25*(3.0*A13+DA)*BC
1         +Q2*A14*BS)*V2(I)+(-0.5*A(4)-0.25*(3.0*A13+DA)
2         *BC-Q2*A14*BS)*V3(I)
 HR23(I)=(A(8)+DB*BC)*V4(I)+(-0.5*A(8)+0.25*(3.0*A57+DB)*BC
1         -Q2*A58*BS)*V5(I)+(-0.5*A(8)+0.25*(3.0*A57+DB)
2         *BC+Q2*A58*BS)*V6(I)
  R23(I)=ER23(I)+HR23(I)
 ER32(I)=(A(4)+DA*BC)*V1(I)+(-0.5*A(4)+0.25*(3.0*A13+DA)*BC
1         -Q2*A14*BS)*V2(I)+(-0.5*A(4)+0.25*(3.0*A13+DA)
2         *BC+Q2*A14*BS)*V3(I)
 HR32(I)=(A(8)-DB*BC)*V4(I)+(-0.5*A(8)-0.25*(3.0*A57+DB)*BC
1         +Q2*A58*BS)*V5(I)+(-0.5*A(8)-0.25*(3.0*A57+DB)
2         *BC-Q2*A58*BS)*V6(I)
  R32(I)=ER32(I)+HR32(I)
 ER13(I)=(-A14*BS+DE*BC*BS)*V1(I)+(Q2*A(4)-Q4*(A13-DA)*BC
1         +0.5*A14*BS+DE*BC*BS)*V2(I)+(-Q2*A(4)+Q4*(A13-DA)*BC
2         +0.5*A14*BS+DE*BC*BS)*V3(I)
 HR13(I)=(A58*BS+DH*BC*BS)*V4(I)+(Q2*A(8)+Q4*(A57-DB)*BC
1         -0.5*A58*BS+DH*BC*BS)*V5(I)+(-Q2*A(8)-Q4*(A57-DB)*BC
2         -0.5*A58*BS+DH*BC*BS)*V6(I)
  R13(I)=ER13(I)+HR13(I)
 ER31(I)=(A14*BS+DE*BC*BS)*V1(I)+(Q2*A(4)+Q4*(A13-DA)*BC
1         -0.5*A14*BS+DE*BC*BS)*V2(I)+(-Q2*A(4)-Q4*(A13-DA)*BC
2         -0.5*A14*BS+DE*BC*BS)*V3(I)
 HR31(I)=(-A58*BS+DH*BC*BS)*V4(I)+(Q2*A(8)-Q4*(A57-DB)*BC
1         +0.5*A58*BS+DH*BC*BS)*V5(I)+(-Q2*A(8)+Q4*(A57-DB)*BC
2         +0.5*A58*BS+DH*BC*BS)*V6(I)
  R31(I)=ER31(I)+HR31(I)
```

```
 55   CONTINUE
      S(1)=1.0/(1.5*Q*(A(9)*(A(1)+A(2))+A(10)*(A(5)+A(6))))
      S(2)=1.0/(3.0*Q*(A(9)*A(3)+A(10)*A(7)))
       S(3)=(-R21(2)*R33(2)+R31(2)*R23(2))/R(2)
       S(4)=(-R21(3)*R33(3)+R31(3)*R23(3))/R(3)
       S(5)=R12(4)/(R11(4)**2+R12(4)**2)
      S(6)=1.0/C11(1)
      S(7)=(C22(2)*C33(2)-C32(2)*C23(2))/C(2)
      S(8)=(C22(3)*C33(3)-C32(3)*C23(3))/C(3)
      S(9)=(C22(4)*C33(4)-C32(4)*C23(4))/C(4)
      S(10)=(R22(2)*R33(2)-R32(2)*R23(2))/R(2)
      S(11)=(R22(3)*R33(3)-R32(3)*R23(3))/R(3)
      S(12)=R11(4)/(R11(4)**2+R12(4)**2)
      RETURN
      END
```

OF BPYJ40:BPY21A.XYZ (F1496) FOR USER BPYJ40 COMPLETED AT 19:42:34 1

REFERENCES

Abeles B. and Meiboom S., 1956, Phys. Rev. 101, 544.

Akgöz Y.C., 1974 PhD Thesis, University of Durham.

Akgöz Y.C., Farley J.M. and Saunders G.A., 1972, J. Mater. Sci., 7, 598.

Akgöz Y.C. and Saunders G.A., 1971, J. Mater. Sci., 6, 395.

Akgöz Y.C. and Saunders G.A., 1974, J. Phys. C.: Solid State Phys. 7, 1655.

Akgöz Y.C. and Saunders G.A., 1975, J. Phys. C.: Solid State Phys. 8, 1387.

Akgöz Y.C. and Saunders G.A., 1975, J. Phys. C: 8, 2962.

Aubrey J.E., 1971, J. Phys. F.: Metal Phys. 1, 493.

Bate R.T. and Einspruch N.G., 1967, Phys. Rev. 153, 796.

Beer A.C. 1963, Solid State Phys. Supplement 4.

Belashchenko D.K., Gushchina E.I., Omarova D.K., 1971, Phys. Met. and Metallogr. (G.B.) - Fiz. Met and Metalloved (U.S.S.R.), Vol. 31, No. 5, 930.

Bhagavantam S., 1966 'Crystal Symmetry and Physical Properties' (Academic Press, London).

Bhargava R.N., 1967, Phys. Rev., 156, 785.

Blatt F.J., 1968 'Physics of Electronic Conduction in Solids' (McGraw-Hill, New York).

Brooks and Herring Cf., Debye P.P. and Conwell E.M., 1954, Phys. Rev. 93, 693.

Brown R.D., Hartman R.L. and Koenig S.H., 1968, Phys. Rev. 172, 598.

Brown S.H. and Lane C.T., 1941, Phys. Rev., 60, 895.

Brown S.H. and Lane C.T., 1941, Phys. Rev., 60, 899.

Casimir H.B.G., 1945, Rev. Mad. Phys. 17, 343.

Casimir H.B.G. and Gerritse A.N., 1941, Physica 8, 1107.

Cohen N.H., Falicov L.M. and Golin S., 1964, IBM, J. Rev. Develop. 8, 215.

Conwell E.M. and Weisskopf V.F. 1946, Phys. Rev. 69, 258.

Conwell E.M. and Weisskopf V.F. 1950, Phys. Rev. 77, 388.

Datars W.R. and Dexter R.N., 1961, Phys. Rev. 124, 75.

Datars W.R. and Vanderkooy J., 1964, IBM, J. Res. Develop. 8, 247.

Dingle R.B., 1955, Phil. Mag. 46, 831.

Drabble J.R. and Wolfe R. 1956, Proc. Phys. Soc. B69, 1101.

Dresselhaus M.S. 1971, J. Phys. Chem. Solids 32, Suppl. 1, 3-33.

Dunsworth A.E. and Datars W.R., 1973, Phys. Rev., B7, 3435.

Epstein S. and Juretschke H.J., 1963, Phys. Rev., 129, 1148.

Erikesson L., Beckman O. and Hürnfeldt S., 1964, J. Phys. Chem. Solids, 25, 1339.

Falicov L.M. and Golin S., 1965, Phys. Rev. 137, A871.

Falicov L.M. and Lin P.J., 1966, Phys. Rev. 141, 562.

Ferreira L.G. 1968, J. Phys. Chem. Solids, 28, 1891 and 29, 537.

Freedman S.J. and Juretschke H.J., 1961, Phys. Rev. 124, 1379.

Fuchser T.D., Mackey H.J. and Sybert J.R., 1970, Phys. Rev. B2, 3863.

Golin S., 1968, Phys. Rev. 166, 643.

Grabner L., 1960, Phys. Rev. 117, 689.

Gregers-Hansen P.E., J. Phys. Chem. Solids, 32, 1881.

Harman T.C. and Honig J.M., 1967, 'Thermoelectric and Thermomagnetic Effects and Applications' (McGraw-Hill, New York).

Harte G.H., 1974, PhD Thesis, University of Bristol.

Harte G.H. and Priestley M.G., 1975 (to be published).

Heine V., 1960, Fermi Surface.

Heremans J., Issi J-P, Rashid A.A.M. and Saunders G.A., 1977, J. Phys. C. Vol.10, 22, 5411.

Herring C., 1955, Bell Syst. Tech. Jour. 34, 237.

Herring C. and Vogt E., 1956, Phys. Rev. 101, 944.

Hurd C.M. 1972 'The Hall Effect in Metals and Alloys' (Plenum, New York).

Ishizawa Y. and Tanuma S., 1965, J. Phys. Soc. Japan, 20, 1278.

Jacobson D.M., 1973, Phys. Stat. Sol. (b) 58, 243.

Jan J-P, 1957, Solid State Phys. 5, 3.

Jeavons A.P., 1969, PhD Thesis, University of Durham.

Jeavons A.P. and Saunders G.A., 1969, Proc. Roy. Soc. A310, 415.

Kao L.P. and Katz E. 1958, J. Phys. Chem. Solids 6, 223.

Kechin V.V. 1968 Sov. Phys., Solid State 9, 2828.

Ketterson J. and Eckstein Y., 1963, Phys. Rev., 132, 1885.

Landau L.D. and Lifshitz E., 1960, 'Electrodynamics of Continuous Media' (Pergamon Press).

Lerner L.S. 1962, Phys. Rev. 127, 1480.

Lichnowski A., 1975, PhD Thesis, University of Durham.

Lifshitz I.M. Azbel M.Ya. and Keganov M.I., 1973, 'Electron Theory of Metals' (Consultants Bureau).

Lin P.J. and Falicov L.M., 1966, Phys. Rev. 142, 441.

Logan J.K. and Marcus J.A., 1952, Phys. Rev. 88, 1234.

Michenaud J-P and Issi J-P., 1972, J. Phys. C., 5, 3061.

Mott N.F. and Jones H. 1936, 'The Theory of the Properties of Metals and Alloys' (Oxford University Press).

Nelder J.A. and Mead R. 1965, Comput. J. 7, 308.

Oktu O. and Saunders G.A. 1967, Proc. Phys. Soc. 91, 156.

Pfann W.G. 1966, 'Zone Melting' (John Wiley and Sons).

Priestley M.G., Windmiller L.R., Ketterson J.B. and Eckstein Y., 1967, Phys. Rev. 154, 671.

Rao G.N., Zebuni N.H., Grenier C.G. and Reynolds J.M., 1964, Phys. Rev., 133, A141.

Saunders G.A., 1968, Journal de Physique Colloque C4, Supplement au No. 11-12, p.C4-3.

Saunders G.A., 1974 (to be published).

Saunders G.A., Cooper G., Miziumski C. and Lawson A.W., 1965, J. Phys. Chem Solids 26, 533.

Saunders G.A. and Öktü O., 1968, J. Phys. Chem. Solids 29, 327.

Saunders G.A. and Öktü O., 1968, J. Phys. Chem. Solids 29, 1589.

Saunders G.A. and Sümengen Z. 1972, J. Phys. F: Metal Phys. 2, 972.

Shtrikman S. and Thomas H., 1965, Solid State Commun. 3, 147

Sladek R.J., 1955, Phys. Rev. 97, 902.

Smith G.E., Wolfe R. and Haszko S.E., 1964, Proc. Int. Conf. Semic. Phys. Paris. Page 399.

Smith G.E., Galt J.K. and Merritt F.R., 1960, Phys. Rev. Letters, 4, 276.

Sondheimer E.H., 1952, Proc. Phys. Soc. A65, 561.

Soule D.E., 1958, Phys. Rev. 112, 698.

Stout M.B., 1960, 'Basic Electrical Measurements' (Prentice Hall) Ch.7.

Sümengen Z. and Saunders G.A. 1972a, Solid State Phys. 5, 425.

Sümengen Z. and Saunders G.A., 1972b, Solid State Commun. 10, 37.

Sümengen Z., Turetken N. and Saunders G.A., 1974, J. Phys. C: Solid State Phys. 7, 2204.

Tiller W.A., Jackso K.A., Rutter J.W. and Chalmers B., 1953, ACTA Metallurgica 1, 428.

Tsai C.L., Waldorf D., Tanaka K., and Grenier C.G. 1978, Phys. Rev. B, Vol. 17, No. 2, 618.

Volger J., 1950, Phys. Rev. 79, 1023.

Windmiller L.R., 1966, Phys. Rev. 149, 472.

Windmiller L.R., Priestley M.G., 1965, Solid State Commun., 3, 199.

Yim W.M. and Dismukes J.P., 1967, J. Phys. Chem. Solids, Suppl. 187-196.

Zimann J.M., 1960, 'Electrons and Phonons' (Oxford at the Clarendon Press).

Zitter R.N., 1962, Phys. Rev. 127, 1471.

PUBLICATIONS

1. Hall-effect in Gold-Silver Alloys. T. Dosdal, D. Grieg and A.A.M. Rashid (J. Phys. F. Metal Phys. Vol. 5 November 1975 pages 2109-2118).

2. Electrical and Thermal Transport Properties of Arsenic. J. Heremans, J-P Issi, A.A.M. Rashid and G.A. Saunders (J. Phys. C. Vol. 10 No. 22, November 1977 pages 5411-5422).

3. Field Dependent Tensors in Antimony-tin and Antimony-Germanium Alloy Single Crystal. A.A.M. Rashid and G.A. Saunders (in preparation).

4. Hall-effect in Gold-Silver Alloys. T. Dosdal, D. Grieg and A.A.M. Rashid, European Physics Society Conference on Conduction Electron in Metals, University of East Anglia, September 1974.

5. Magnetoresistivity of Bismuth and Tellirium doped Bismuth Single Crystal. A.A.M. Rashid, C.Y. Akgoz and G.A. Saunders, Arabic Scientific Journal, University of Manchester, August 1975.

6. Electron Scattering in Arsenic. J. Heremans, J-P Issi, A.A.M. Rashid and G.A. Saunders, Conference of 'La Societe Belge de Physique', Brussels 9-10 June 1977.

7. Electrical and Thermal Transport Properties of Arsenic. J. Heremans, J-P Issi, A.A.M. Rashid and G.A. Saunders, European Physical Society Conference on Electron Transport and Molecular Solids, University of Leeds 26-29 July 1977.